Boundary integral equation methods for simulation and design of photonic devices

Thesis by
Emmanuel Garza

In Partial Fulfillment of the Requirements for the
Degree of
Doctor of Philosophy

CALIFORNIA INSTITUTE OF TECHNOLOGY
Pasadena, California

2020
Defended December 12th, 2019

Emmanuel Garza
ORCID: 0000-0003-1687-8216

ACKNOWLEDGMENTS

I would like to first thank my advisor, Professor Oscar P. Bruno, who took a chance in the summer of 2011 by having me as a SURF student. He brought me back as a SURF student in 2012 before taking me as a graduate student in 2013. I will forever be grateful to him for giving me these opportunities that changed my life. I'm also grateful to my thesis committee, Professors Houman Owhadi, Andrei Faraon, and Constantine Sideris. In particular, the work of Chapter 7 would not have been possible without the input and contributions from Professors Faraon and Sideris.

During my time at Caltech, I had the pleasure of crossing paths with many incredible people whose work is reflected either directly or indirectly in this thesis. In particular, I have to thank Carlos Pérez-Arancibia for helping me understand the nuts and bolts of integral equation methods, and providing crucial contributions on the WGF method of Chapter 2. I owe a great deal to Agustin Fernandez-Lado whose parallel implementation of the accelerator, and contributions to Chapter 7 cannot be overstated. Additionally, I would like to thank fellow members of Professor Bruno's group, both past and present: Max Cubillos, Eldar Akhmetgaliyev, Thomas Anderson, Martín Maas, Ambuj Pandey, Jagabandhu Paul, Christoph Bauinger, Daniel Leibovici, John Emmons, James Guzman, Luke Voss and Victor Kononov.

A special thanks goes to Edwin Jimenez, whose friendship and mentorship dates back to my first summer in Pasadena. He taught me not to be afraid of not knowing, and that most mathematical problems rest in simple and elegant ideas. I also thank him for his contributions to this work, including the many discussions about the three-dimensional integral equation solvers and the derivation of the adjoint operators from Chapter 7. To the amazing friends I've made throughout this journey: Fabio, Hugo, Josh, Porfirio and Scott. My life at Caltech was much better thanks to them.

I would have never been able to do this work without my parents' sacrifices so that I could have the best education. Thanks to my brother and sister for their support and friendship. Finally, a special thanks to my wife, Ellen Barry, who inspires me everyday to be a better person, and has taught me the real meaning of happiness.

ABSTRACT

This thesis presents novel boundary integral equation (BIE) and associated optimization methodologies for photonic devices. The simulation and optimization of such structures is a vast and rapidly growing engineering area, which impacts on design of optical devices such as waveguide splitters, tapers, grating couplers, and metamaterial structures, all of which are commonly used as elements in the field of integrated photonics. The design process has been significantly facilitated in recent years on the basis of a variety of methods in computational electromagnetic (EM) simulation and design. Unfortunately, however, the expense required by previous simulation tools has limited the extent and complexity of the structures that can be treated. The methods presented in this thesis represent the results of our efforts towards accomplishing the dual goals of 1) Accurate and efficient EM simulation for general, highly-complex three-dimensional problems, and 2) Development of effective optimization methods leading to an improved state of the art in EM design.

One of the main proposed elements utilizes BIE in conjunction with a modified-search algorithm to obtain the modes of uniform waveguides with arbitrary cross sections. This method avoids spurious solutions by means of a certain normalization procedure for the fields within the waveguides. In order to handle problems including nonuniform waveguide structures, we introduce the windowed Green function (WGF) method, which used in conjunction with auxiliary integral representations for bound mode excitations, has enabled, for the first time, accurate simulation of a wide variety of waveguide problems on the basis of highly accurate and efficient BIE, in two and three spatial dimensions. The "rectangular-polar" method provides the basic high-order singular-integration engine. Based on non-overlapping Chebyshev-discretized patches, the rectangular-polar method underlies the accuracy and efficiency of the proposed general-geometry three-dimensional BIE approach. Finally, we introduce a three-dimensional BIE framework for the efficient computation of sensitivities—i.e. gradients with respect to design parameters—via adjoint techniques. This methodology is then applied to the design of metalenses including up to a thousand parameters, where the overall optimization process takes in the order of three hours using five hundred computing cores. Forthcoming work along the lines of this effort seeks to extend and apply these methodologies to some of the most challenging and exciting design problems in electromagnetics in general, and photonics in particular.

PUBLISHED CONTENT AND CONTRIBUTIONS

[1] Oscar P. Bruno and Emmanuel Garza. A Chebyshev-based rectangular-polar integral solver for scattering by general geometries described by non-overlapping patches. *arXiv*, 2018. arXiv ID: 1807.01813.
E. Garza participated in the conception of the project, development of the integration strategy, coded the numerical method, and did the presented simulations.

[2] Oscar P. Bruno, Emmanuel Garza, and Carlos Pérez-Arancibia. Windowed Green function method for nonuniform open-waveguide problems. *IEEE Transactions on Antennas and Propagation*, 65(9):4684–4692, September 2017. ISSN 0018926X. doi: 10.1109/TAP.2017.2728118. arXiv ID: 1610.04939.
E. Garza participated in the conception of the project, solved the problem of incorporating incident bound modes, provided the programming of the numerical method, and did the presented simulations.

[3] Constantine Sideris, Emmanuel Garza, and Oscar P. Bruno. Ultra-Fast Simulation and Optimization of Nanophotonic Devices with Integral Equation Methods. *ACS Photonics*, November 2019. ISSN 2330-4022. doi: 10.1021/acsphotonics.9b01137.
E. Garza participated in the conception of the project, provided input on the implementation of the WGF method, and edited the figures.

TABLE OF CONTENTS

LIST OF ILLUSTRATIONS

LIST OF TABLES

Background

Chapter 1

INTRODUCTION

The understanding of electromagnetic phenomena has revolutionized the way we interpret and interact with the world. With the advent of computational tools, applied electromagnetics has seen an exponential growth—devices that were designed using these tools are now ubiquitous in our lives. With increasing improvements in computational resources, new simulation capabilities continue to emerge, and although the governing electromagnetic laws have been known for more than 150 years, new discoveries and developments continue to be obtained at an ever increasing pace.

1.1 Maxwell's equations

Classical electrodynamics, if had to be described in one sentence, is the study of how charged particles interact with other charged particles. All of the extremely rich electromagnetic theory stems, either directly or indirectly, from this concept. In fact, quoting the popular undergraduate text by Griffiths [42, p. 438-439]:

> "[...] if we could only write down the formula for the force one charge exerts on another, we would be done with electrodynamics, in principle. That, together with the superposition principle, would tell us the force exerted on a test Q by any configuration whatsoever. Well.. here we are: [...]"

and then proceeds to show the formula for the force between two charges. Use of this formula ([42, equation 10.67]) for every relevant moving and stationary charge in a given configuration, fully encapsulates all of the predictions of electromagnetism for the configuration at hand.

From a historical perspective, it was the experiments by Michael Faraday—which established the relation between electricity and magnetism— that marked a turning point in the understanding of electromagnetism. It was then the Scottish physicist James Clerk Maxwell who, in a set of publications [29, 30, 59, 60], unified and expanded the known theory to what we now call the Maxwell's equations, which encompass the description of all classical electromagnetic phenomena.

The concept of electromagnetic (EM) fields were introduced to make the calculation of EM forces more manageable. In essence, the EM fields are quantities that describe how much of a force, and in what direction, would a charged particle experience if put at a given point in space. Since EM forces are between two charged particles, then it is natural to think of the EM fields as produced by some *source*, which is either static or moving charges—the latter also know as electric currents. In its differential form, Maxwell's equations for the electromagnetic fields are given by [42, p. 330]

$$\nabla \cdot \mathbf{D} = \frac{1}{\varepsilon_0}\rho_f, \quad \text{Gauss's law} \tag{1.1a}$$

$$\nabla \cdot \mathbf{B} = 0, \quad \text{Gauss's law for } \mathbf{B} \tag{1.1b}$$

$$\nabla \times \mathbf{E} + \frac{\partial \mathbf{B}}{\partial t} = 0, \quad \text{Faraday's law} \tag{1.1c}$$

$$\nabla \times \mathbf{H} - \frac{\partial \mathbf{D}}{\partial t} = \mathbf{J}_f, \quad \text{Ampère's law with Maxwell's correction} \tag{1.1d}$$

where the electromagnetic and auxiliary fields are denoted by

- $\mathbf{E}$: Electric field
- $\mathbf{B}$: Magnetic induction field
- $\mathbf{D} \equiv \varepsilon_0\mathbf{E} + \mathbf{P}$: Electric displacement field
- $\mathbf{H} \equiv \frac{1}{\mu_0}\mathbf{B} - \mathbf{M}$: Magnetic (H) field

The specific constitutive relations between the EM and auxiliary fields depend on the material properties defined by the quantities:

- $\mathbf{P}$: Polarization $\longrightarrow$ electric dipole moment per unit volume
- $\mathbf{M}$: Magnetization $\longrightarrow$ magnetic dipole moment per unit volume

The EM fields are created by sources that can either be distributed over volumes or surfaces. These quantities are usually denoted by the following notation:

- ρ_f: Free charge (volumetric) density
- σ_f: Free charge (surface) density
- $\mathbf{J}_f$: Free current (volumetric) density
- $\mathbf{K}_f$: Free current (surface) density

As with any other system of partial differential equations, to solve Maxwell's equations (1.1), we need corresponding initial and boundary conditions. In particular, the boundary conditions are given by

$$D_1^{\perp} - D_2^{\perp} = \sigma_f, \tag{1.2a}$$

$$B_1^{\perp} - B_2^{\perp} = 0, \tag{1.2b}$$

$$\mathbf{E}_1^{\parallel} - \mathbf{E}_2^{\parallel} = 0, \tag{1.2c}$$

$$\mathbf{H}_1^{\parallel} - \mathbf{H}_2^{\parallel} = \mathbf{K}_f \times \boldsymbol{n}, \tag{1.2d}$$

which themselves can be derived from the integral form of Maxwell's equations.

These relationships hold in general for any material. However, in most of the cases we deal with linear media, which satisfy the constitutive relations

$$\mathbf{P} = \varepsilon_0 \chi_e \mathbf{E}, \tag{1.3a}$$

$$\mathbf{M} = \chi_m \mathbf{H}, \tag{1.3b}$$

where χ_e and χ_m are the electric and magnetic—respectively—susceptibility tensors. In this case, the auxiliary fields depend linearly on the EM fields:

$$\mathbf{D} = \varepsilon \mathbf{E}, \tag{1.4a}$$

$$\mathbf{H} = \frac{1}{\mu}\mathbf{B}, \tag{1.4b}$$

where ε and μ are the electric permittivity and magnetic permeability tensors, respectively. If, additional to the medium being linear, it is also isotropic, then ε and μ are just constants (or a diagonal tensor with all diagonal entries equal). And if the medium obeys Ohm's law with conductivity σ, the free current density is then [42, eq. 9.117]

$$\mathbf{J}_f = \sigma \mathbf{E}. \tag{1.5}$$

Maxwell's equations in Eq. (1.1) are the mathematical model of how charged particles produce electric fields, currents produce magnetic fields, and how time-varying electric (resp. magnetic) fields produce magnetic (resp. electric) fields.

1.2 Time-harmonic solutions: The frequency domain

In this thesis, we are interested in the solution of electromagnetic problems that involve linear, piecewise homogeneous media. A standard technique for simplifying Maxwell's equations is to take time-harmonic solutions—solutions that have a $e^{-i\omega t}$

time-dependence—given that a time-domain solution can then be reconstructed via a Fourier transform in time.

Time-harmonic solutions are not just useful as an intermediate tool to the full time-domain solution, but in fact they provide the full solution when the problem has sources with only one frequency—which is the case in many real-life applied settings.

Mathematically, a time-harmonic solution is an electromagnetic field of the form

$$\mathbf{E}(\boldsymbol{r}, t) = \operatorname{Re}\left(\widetilde{\mathbf{E}}(\boldsymbol{r})e^{-i\omega t}\right), \tag{1.6a}$$

$$\mathbf{H}(\boldsymbol{r}, t) = \operatorname{Re}\left(\widetilde{\mathbf{H}}(\boldsymbol{r})e^{-i\omega t}\right). \tag{1.6b}$$

Since for the remaining of the thesis we'll be working with time-harmonic solutions, we use a well-known notational abuse by dropping the time dependence from the notation, and we thus write

$$\widetilde{\mathbf{E}} = \mathbf{E}, \tag{1.7a}$$

$$\widetilde{\mathbf{H}} = \mathbf{H}. \tag{1.7b}$$

Then, by defining the (complex) wavenumber k:

$$k \equiv \omega\sqrt{\mu\left(\varepsilon + i\frac{\sigma}{\omega}\right)} \tag{1.8}$$

(where the branch of the square root is taken so that the imaginary part of k is negative), and substituting into equation (1.1), under the assumption of absence of free charges and currents (other than the ones induced by Ohm's law), we obtain the time-harmonic version of Maxwell's equations [63]

$$\nabla \times \mathbf{H} + i\omega\left(\varepsilon + i\frac{\sigma}{\omega}\right)\mathbf{E} = 0, \tag{1.9a}$$

$$\nabla \times \mathbf{E} - i\omega\mu\mathbf{H} = 0, \tag{1.9b}$$

with boundary equations (1.2) which, in the present context, are generally expressed in the forms [1]

$$\mathbf{E}^+ \times \boldsymbol{n} - \mathbf{E}^- \times \boldsymbol{n} = 0, \tag{1.10a}$$

$$\mathbf{H}^+ \times \boldsymbol{n} - \mathbf{H}^- \times \boldsymbol{n} = 0. \tag{1.10b}$$

[1] For conductors that satisfy Ohm's law, the free surface current vanishes. See Griffiths [42, p. 397]

1.3 Units and electromagnetic parameters

For frequency domain problems, the relevant material properties are the electric permittivity ε and magnetic permeability μ. In vacuum, these quantities are denoted by ε_0 and μ_0. In many instances, nonmagnetic materials are consider, for which $\mu = \mu_0$ and then the material is fully characterized by the permittivity, or equivalently, by the refractive index n. Additionally, the frequency ω of the problem (sometimes called the "pulsation") must be specified. Then, letting c_0 and c denote the speed of light in vacuum and inside a medium, respectively, we have the relations

$$c = \frac{1}{\sqrt{\mu\varepsilon}}, \tag{1.11a}$$

$$n = \sqrt{\frac{\varepsilon\mu}{\varepsilon_0\mu_0}} = \frac{c_0}{c}, \tag{1.11b}$$

$$\lambda = \frac{\lambda_0}{n}, \tag{1.11c}$$

$$k_0 = \frac{2\pi}{\lambda_0} = \frac{c_0}{\omega}, \tag{1.11d}$$

$$k = n\, k_0. \tag{1.11e}$$

Typically, one of the quantities ω, λ_0 or k_0 is selected; the remaining electromagnetic parameters can be found given the permittivities and permeabilities for each relevant dielectric domain.

Throughout this thesis, we utilize units for which $\varepsilon_0 = \mu_0 = 1$. In the present context, we typically measure wavelengths in microns ($1\,\mu m = 10^{-6}$ m)—a unit that is quite common for photonic applications—so that $c_0 = 1\,[\mu m/T]$, where T is the unit of time that makes c_0 consistent with the SI value of the speed of light of exactly 299 792 458 m/s [46]. For this example, the relevant unit of time is then $T = 10^{-6}/299\,792\,458$ s. The other quantities can be then found from these time units—e.g. the frequency $f = c_0/\lambda_0 = 1\,[T^{-1}] = 2.998 \times 10^{14}$ Hz.

1.4 Boundary integral equation methods

The problem of wave scattering by obstacles plays a central role in theoretical and computational electromagnetism. In a scattering configuration, an incoming wave impinges upon a set of obstacles (the "scatterers"), and is subsequently "scattered"—in accordance with a generally quite complex process governed by Maxwell's equations. Only in the simplest cases can closed-form expressions be found for the solution—most notably, scattering by a sphere can be expressed in a series solution that relies on spherical Bessel functions.

For more complex scatterers, however, evaluation of solutions requires use of computational methods. Notably, the finite-difference time-domain method [76] has been one of the most widely used techniques due to its robustness and conceptual simplicity. In the context of scattering problems, these methods require of artificially absorbing boundaries to simulate the infinite propagation domain within the necessarily-bounded computational domain. The class of numerical methods that rely on discretizing the truncated volumetric simulation domain are usually called "volumetric solvers."

Examination of the physical phenomena that underlies the scattering problem, however, gives rise to important alternative solution techniques. We thus consider the sequence of events inherent in the scattering process: as an incoming wave hits the scatterer, the fields induce currents on the scattering boundaries—giving rise to an additional EM field—which, in turn, affect the currents, etc. Importantly, the surface currents can be utilized to completely determine the electromagnetic state of a system: the EM fields can be computed from such current distributions. Boundary integral equations (BIE) for scattering problems provide a description of this phenomenology that relies solely on surface currents—and, thus provides a mathematical formulation which is spatially restricted to the scattering boundaries, and which, as discussed in what follows, gives rise to significant advantages from a computational standpoint.

Both volumetric and BIE methods have pros and cons. Volumetric methods tend to be simpler to implement, they can handle linear and nonlinear materials alike, and they either do not require solution of linear systems of equations, when used in the time domain or, at worst, when directly used in the frequency domain, require only sparse linear systems. However, these methods do require discretization of the entire volume, and their time-domain versions are restricted by CFL time-step constraints. BIE methods, on the other hand, only require discretization of the scattering boundaries, thus reducing by one the dimensionality of the problem, and they additionally naturally incorporate the "boundary condition at infinity" (the so-called outgoing radiation conditions) on the scattered fields. The caveat is that they tend to be more complicated to implement, they result in full (non-sparse) matrices, and they also require additional algorithms (so called accelerators) to eliminate the substantial cost (quadratic or worse in the number of unknowns) that arises from the associated, non-sparse, matrix equations. In spite of this caveat, however, integral-equation methods do provide significant advantages in terms of accuracy

and computing costs.

1.5 Dielectric waveguides

One of the central themes in this thesis concerns the propagation of fields in the presence of dielectric waveguide structures. In brief, a dielectric waveguide is composed of at least two dielectric regions; the core of the waveguide has the higher refractive index, and the lower-refractivity cladding material surrounds the core. Dielectric waveguides significantly differ from perfectly electric conducting (PEC) waveguides, since in the PEC case the fields are fully contained inside the structure, while in the dielectric case, nonvanishing fields exist outside of the waveguide core. Although the first studies of dielectric waveguides date back to 1910 [45], the interest in these structures was not significant until the sixties and seventies where optical fibers (a class of dielectric waveguides) found their applications in telecommunications [75].

A uniform waveguide consists of a single infinite cylindrical structure of arbitrary cross section. Uniform waveguides, with distinctive core (interior) and cladding (exterior) regions, can support electromagnetic fields that propagate without loss along the waveguide core all the way to infinity. Such solutions, which lie at the heart of the usefulness of these structures, are known as the "bound modes" of the waveguide. A nonuniform waveguide structure, on the other hand, is partly comprised of uniform semi-infinite waveguides (SIW)—a half of an infinite uniform waveguide that carries energy to and/or from infinity—joined at junctions, terminations or additional bounded scatterers (devices) that perform desired optical operations.

Chapters 2, 3 and 6 in this thesis treat a variety of waveguide problems on the basis of boundary integral equations. The unbounded character of these problems, which had previously been found challenging in the context of integral-equation based solvers, is tackled here by means of a novel "windowing" concept which is described in the following section.

1.6 Windowing of improper integrals

Boundary integral equation methods have been mostly used in the context of bounded obstacles. However, recent advances in "windowing" methods [13, 18, 20, 21, 23, 55, 61, 68] have demonstrated that integral equations provide a powerful tool for problems that involve unbounded obstacles. In brief, the windowing approach is based on the observation that, along infinite boundaries, the relevant integral equations involve oscillatory and slowly decaying integrands (that result as the products

of a non-decaying oscillatory current density times a decaying and oscillatory kernel). In fact, this behavior can be characterized by an idealized integration problem consisting on approximating the integral[2]

$$I = \int_1^\infty e^{ik_z z} \frac{e^{-ik_0 z}}{\sqrt{z}} \mathrm{d}z, \tag{1.12}$$

where we can interpret the term $e^{ik_z z}$ to be representative of the boundary densities, while $e^{-ik_0 z}/\sqrt{z}$ accurately represents the character of the integral-equation kernel asymptotics. The integral in equation (1.12) is in fact not absolutely integrable, and the convergence results only because of the oscillatory harmonic factor. From a numerical perspective, a simple truncation followed by straight-forward numerical evaluation of the form

$$I_{\mathrm{tr}}(A) = \int_1^A e^{ik_z z} \frac{e^{-ik_0 z}}{\sqrt{z}} \mathrm{d}z, \tag{1.13}$$

using a finite value A, might at first be viewed as a potentially useful numerical approximation. Unfortunately, however, the convergence of this approximation is extremely slow: a simple integration-by-parts argument provides the error estimate [13, 61]

$$|I - I_{\mathrm{tr}}(A)| = O\left(\frac{1}{|k_0 - k_z|\sqrt{A}}\right), \tag{1.14}$$

which shows that one additional digit of numerical accuracy requires an increase in the size of the computational domain by a factor of one-hundred—which is clearly prohibitive given that each increase in the size of the computational domain corresponds, in the integral-equation version, to a proportional increase in the number of unknowns used for the solution of the problem. But in fact, consideration of the error analysis just presented suggests a possible solution to the problem, namely, use of a smooth and slowly-rising truncation window to eliminate the boundary terms (and, therefore, the slow decay), to as many orders as desired in the integration by parts procedure, showing that the error is "super-algebraically" small.

In detail, the windowing method utilizes a window function $w_A(z)$ that satisfies the following properties:

(i) $w_A(z)$ vanishes for z outside the interval $[-A, A]$.

[2]Here we use the variable z since in the context of waveguides, the optical axis is usually aligned with the z-axis.

(ii) $w_A(z) = 1$ for $z \in (-\alpha A, \alpha A)$ for some α satisfying $0 < \alpha < 1$.

(iii) All of the derivatives $w_A^{(p)}(z)$ (p a positive integer) vanish at $z = \pm A$ and $z = \pm\alpha A$.

(iv) $w_A(z)$ enjoys a "slow-rise." (I.e., when rescaled to a unit interval, all of the derivatives of $w_A(z)$ remain uniformly bounded for all A; see Chapter 2.)

Then, the approximation

$$I_w(A) = \int_1^A w_A(z) e^{ik_z z} \frac{e^{-ik_0 z}}{\sqrt{z}} \mathrm{d}z, \tag{1.15}$$

which is only minimally more expensive than equation (1.13), incurs a super-algebraically small error, that is to say, for all positive integers p we have

$$|I - I_w(A)| = O\left(\frac{1}{|k_0 - k_z|^p A^{p-\frac{1}{2}}}\right). \tag{1.16}$$

The significant convergence improvement that results from use of the windowing method is demonstrated in Figure 1.1, where $k_0 = 2\pi$ and several values of k_z were used. An important observation from this numerical experiment is that in general, the convergence of the windowed integrals depends on the parameter $A/\widetilde{\lambda}$, where

$$\widetilde{\lambda} = \frac{2\pi}{|k_0 - k_z|}. \tag{1.17}$$

Indeed, as illustrated by when k_z is close to k_0, the error, although still super-algebraically small, has a much larger proportionality constant, which could require use of extremely large windows. This observation is in line with the tenet that the oscillatory character is what makes the windowed integrals rapidly convergent.

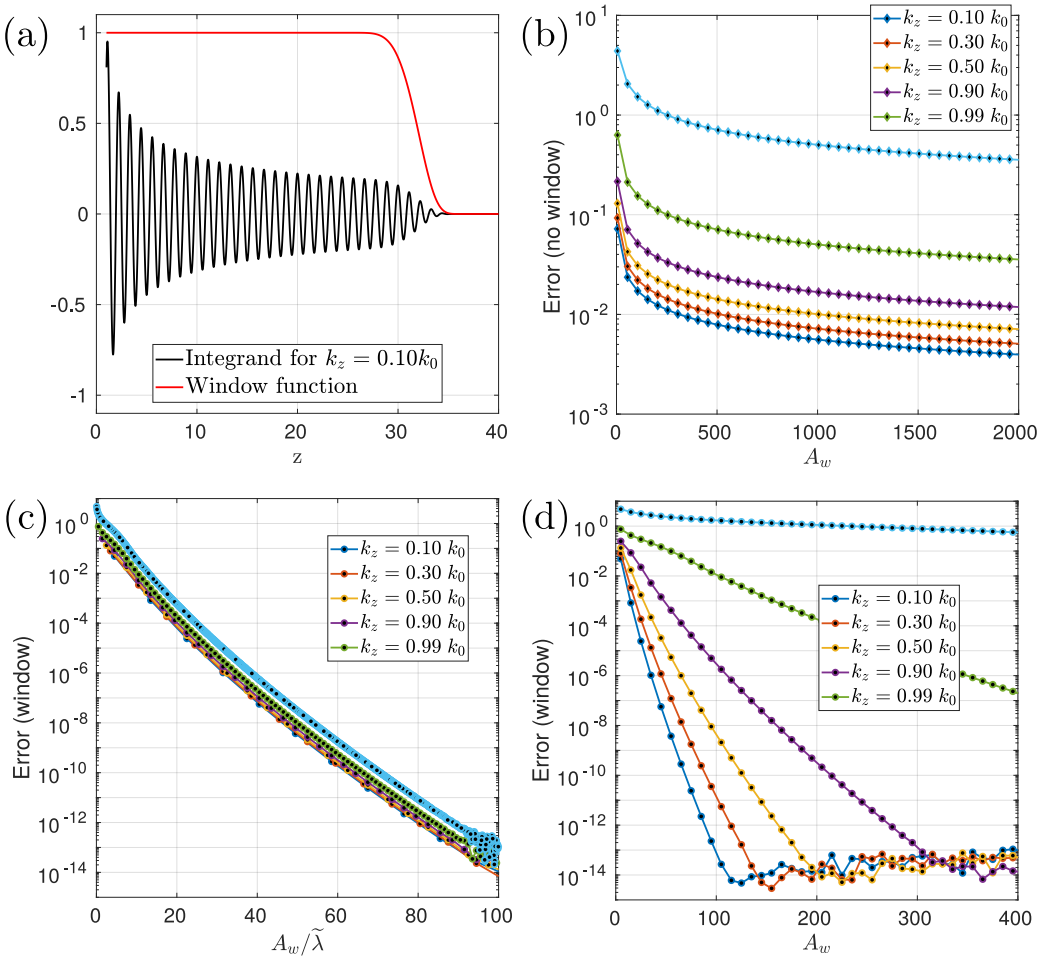

Figure 1.1: Convergence of the integrals from equations (1.12), (1.13) and (1.15). In Figure (a), the plot of the windowed integrand is shown. Figure (b) displays the slow convergence of the direct truncation method. On the other hand, (c) and (d) demonstrate the great improvement introduced by the window function.

1.7 Thesis outline

This thesis is divided into five parts, namely: (1) Background, (2) Two-Dimensional Problems, (3) Three-Dimensional Problems, (4) Shape Optimization of Electromagnetic Devices, and (5) Concluding Remarks. In the "Two-Dimensional Problems" part, Chapter 2 introduces the two-dimensional windowed Green function (WGF) method for nonuniform open-waveguide problems; Chapter 3 presents a boundary integral equation computational method for the two-dimensional problem of evaluation of bound modes on three-dimensional waveguides of arbitrary cross-section.

The "Three-Dimensional Problems" part starts with Chapter 4, which presents a novel high-order "rectangular-polar" integral equation method for acoustic problems in three-dimensional space. This methodology is based on Chebyshev representa-

tions of the surface densities for geometrical obstacles described by a set of non-overlapping patches. Chapter 5 then presents the well-known integral representation formulas of the theory of electromagnetic scattering, and it uses them in conjunction with the "rectangular-polar" technique from Chapter 4 to solve problems of scattering by three-dimensional dielectric obstacles. Chapter 6 uses the dielectric solver developed in Chapter 5 to generalize the WGF method from Chapter 2 to the three-dimensional waveguide problem.

The "Shape Optimization of Electromagnetic Devices" part only contains Chapter 7, which presents a novel boundary integral equation approach for the problem of photonic-device optimization which is based on the integral methodologies developed in previous chapters of this thesis as well as novel adjoint-optimization methods. The "Concluding Remarks" part, finally, summarizes the main findings of this thesis, and it proposes related additional work in this area.

Two-dimensional problems

Chapter 2

WINDOWED GREEN FUNCTION METHOD FOR 2D WAVEGUIDES

This chapter[1] considers the problem of evaluation of wave propagation and scattering in nonuniform open-waveguide structures. This is a problem of fundamental importance in a wide range of areas, including modeling and design of dielectric antenna systems, photonic and optical devices, dielectric RF transmission lines, etc. The numerical simulation of such structures presents significant challenges—in view of the unbounded character of the associated dielectric boundaries and propagation domains as well as the presence of radiating fields, inhomogeneities, and scattering obstacles.

The present contribution introduces an effective methodology for the solution of such nonuniform open-waveguide problems. Based on use of Green functions and integral equations akin to those used in the Method of Moments [37, 73], and incorporating as a main novel element a certain "slow-rise" windowing function, the proposed windowed Green function approach (WGF) can be used to model, with high-order accuracy, highly-complex waveguide structures without recourse to use of mode matching (which can be quite challenging in the open-waveguide context), absorbing boundary conditions, staircasing or time-domain simulations.

The finite-difference time-domain method (FDTD) is one of the simplest and most reliable existing methods for solution of open-waveguide problems. In the FDTD approach, unbounded domains are truncated by relying on absorbing boundary conditions or absorbing layers such as the PML [9]. Further, subpixel smoothing techniques [38] are often used in FDTD implementations to model material interfaces while maintaining second order accuracy—in spite of the staircasing that accompanies Cartesian discretization of curved boundaries. In order to obtain the frequency response from a FDTD simulation, finally, Fourier transforms in time are typically used. In spite of its usefulness, the FDTD approach does present

[1]This chapter is based on the published article: Oscar P. Bruno, Emmanuel Garza, and Carlos Pérez-Arancibia. *Windowed Green function method for nonuniform open-waveguide problems*. IEEE Transactions on Antennas and Propagation, 65(9):4684-4692, Sep. 2017. ISSN 0018-926X. doi: 10.1109/TAP.2017.2728118. Some excerpts have been taken verbatim.

a number of difficulties in the context of waveguide problems [76, p. 223] concerning (i) Illumination by specified waveguide modes and inadvertent excitation of unwanted modes; (ii) Necessary use of sufficiently large computational domains to allow decay of reactive fields; (iii) Need for substantially prolonged simulation times in order for spectral energy above the waveguide cutoff frequency to reach a given interaction structure of interest; and (iv) Necessary use of fine spatial and temporal discretizations to mitigate the numerical dispersion associated with the second-order accuracy of the method.

A few Green function methods for open-waveguide problems have also been proposed. The recent boundary-element method [81], for example, in which a conductive absorber is used to truncate the unbounded waveguide structure, requires the excitation source to lie within the computational domain. The source then produces a radiation field that decays as $O(1/r)$ and thus limits the accuracy of the implementation. Other approaches for open-waveguide problems based on perturbation and transform methods [27, 28, 56] can effectively handle limited types of (sufficiently small) localized inhomogeneities.

Relying on the free space Green function and associated integral equations along the dielectric boundaries, the WGF method presented here utilizes a slow-rise window function to truncate the infinite integrals while providing super-algebraically small error (that is, errors smaller than any negative power of the window size). The method can easily incorporate bound modes and arbitrary beams as illuminating sources, and it can treat general inhomogeneities and multiple arbitrarily oriented waveguides without difficulty.

The proposed use of slow-rise window functions has been previously found highly effective in the contexts of scattering by periodic rough surfaces [13, 21, 61] and obstacles in presence of layered-media [20, 22, 68] as well as long-range volumetric propagation [24]. The implementation details vary from problem to problem; in the present open-waveguide context, for example, the treatment of incident fields and windowed integral operators differs significantly from those used previously.

This chapter is organized as follows: Notations and mathematical background on the open-waveguide problem are presented in section 2.1. The WGF method is then introduced in section 2.2, which includes, in particular, an integration example which demonstrates in a very simple context the properties of the slow-rise windowing function. A variety of applications of the open-waveguide WGF method are presented in section 2.3, demonstrating applicability to waveguide junctions (includ-

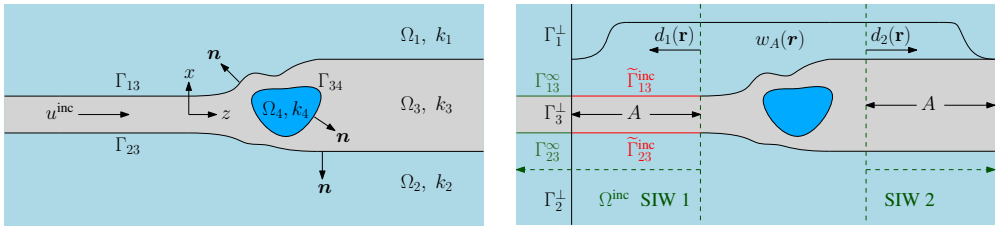

(a) Schematic depiction of a typical waveguide scattering problem.

(b) Notations associated with the WGF method.

Figure 2.1: The open-waveguide problem and geometrical structures utilized in the WGF method presented in this chapter.

ing couplers and sharp bends), dielectric antennas, focused beam illumination, and, for reference, an unperturbed waveguide for which the exact solution is known. In all cases, the WGF method provides high accuracies in computing times of the order of seconds. Significant additional acceleration could be incorporated on the basis of equivalent sources and Fast Fourier Transforms, along the lines of reference [21]; such acceleration methods are not considered here in view of the fast performance that the unaccelerated method already provides in the present two-dimensional case.

2.1 Mathematical Framework for 2D Open Waveguides

This chapter considers the problem of electromagnetic wave propagation and scattering induced by two-dimensional (zx-plane) nonuniform open (dielectric) waveguides, with application to nonuniformities such as waveguide junctions, illumination and termination regions. In Figure 2.1, a schematic depiction of the problem is presented.

General two-dimensional structures consisting of spatial arrangements of two-dimensional dielectric waveguides and bounded dielectric structures can be considered within the proposed framework—including, for example, configurations which are constructed as a combination of a given finite number of "semi-infinite waveguide" structures (SIW) and additional bounded dielectric bodies. Here a SIW is one of the two portions that result as a fully uniform waveguide is cut by a straight line (plane) orthogonal to the waveguide axis. A simple such configuration is depicted in Figure 2.1.

Additionally, it is useful to identify *connected* (bounded or unbounded) regions that are occupied by a given dielectric material; as illustrated in Figure 2.1, these regions are denoted by Ω_j ($j = 1, \ldots, N$). The electrical permittivity, magnetic

permeability, refractive indices and wavenumbers in Ω_j are denoted ε_j, μ_j, n_j and $k_j = \omega\sqrt{\varepsilon_j\mu_j} = n_j\omega/c$ (c being the speed of light in vacuum), respectively.

The structure may be illuminated by arbitrary combinations of bound waveguide modes supported on a single component SIW (or, more precisely, by the restriction to the given SIW of a mode of the corresponding fully uniform waveguide). By linearity, simultaneous illumination by several SIWs can be obtained directly by addition of the corresponding solutions for single SIW illumination. Letting $\boldsymbol{r} = (z, x)$ and denoting by χ^{inc} the indicator function of a SIW region Ω^{inc} that contains the prescribed illuminating field,

$$\chi^{\text{inc}}(\boldsymbol{r}) = \begin{cases} 1 & \text{for } \boldsymbol{r} \in \Omega^{\text{inc}} \\ 0 & \text{for } \boldsymbol{r} \notin \Omega^{\text{inc}}, \end{cases} \tag{2.1}$$

the total electric field $\boldsymbol{E}$ is given by $\boldsymbol{E} = \boldsymbol{E}^{\text{inc}}\chi^{\text{inc}} + \boldsymbol{E}^{\text{scat}}$. (See Figure 2.1b, where the region $\Omega^{\text{inc}} = \{z < 0\}$ is such that the waveguide boundaries are flat within Ω^{inc}, and thus, a bound mode can be prescribed in this region as an incident field.) The scattered field $\boldsymbol{E}^{\text{scat}}$ is assumed to satisfy an appropriate radiation condition (which, roughly, states that the scattered field propagates away from all inhomogeneities as either outward waveguide modes or cylindrical waves; see [67, equation (24)] for details) in each component Ω_j that is not bounded—in addition to the Maxwell equations which, in the two-dimensional case considered in what follows, reduce to the Helmholtz equation.

Assuming a time-harmonic temporal dependence of the form $\mathrm{e}^{-i\omega t}$ (which is suppressed in all subsequent expressions) and letting u (resp. u^{scat}) denote either the y-component of the total (resp. scattered) electric field in TE-polarization or the y-component of the total (resp. scattered) magnetic field in TM-polarization, the field component $u = u^{\text{inc}}\chi^{\text{inc}} + u^{\text{scat}}$ is the unique [67] radiating solution of the problem

$$\begin{cases} \Delta u + k_j^2 u = 0 & \text{in} \quad \Omega_j, \\ u_+ - u_- = 0 & \text{on} \quad \Gamma_{j\ell} \quad (j < \ell), \\ \dfrac{\partial u_+}{\partial \boldsymbol{n}} - \nu_{j\ell}\dfrac{\partial u_-}{\partial \boldsymbol{n}} = 0 & \text{on} \quad \Gamma_{j\ell} \quad (j < \ell). \end{cases} \tag{2.2}$$

Here $\nu_{j\ell} = 1$ in TE-polarization and $\nu_{j\ell} = (k_j/k_\ell)^2$ in TM-polarization; for each pair (j, ℓ) with $j < \ell$, $\Gamma_{j\ell}$ denotes the boundary between Ω_j and Ω_ℓ; for $\boldsymbol{r} \in \Gamma_{j\ell}$, $\boldsymbol{n} = \boldsymbol{n}(\boldsymbol{r})$ denotes the unit normal vector to $\Gamma_{j\ell}$ which points into the "plus side" Ω_j of $\Gamma_{j\ell}$ (the plus side of $\Gamma_{j\ell}$ is defined by the aforementioned condition $j < \ell$); and

for $\boldsymbol{r} \in \Gamma_{j\ell}$, finally,

$$u_{\pm}(\boldsymbol{r}) = \lim_{\delta \to 0^+} u(\boldsymbol{r} \pm \delta \boldsymbol{n}(\boldsymbol{r})), \tag{2.3}$$

$$\frac{\partial u_{\pm}}{\partial \boldsymbol{n}}(\boldsymbol{r}) = \lim_{\delta \to 0^+} \nabla u(\boldsymbol{r} \pm \delta \boldsymbol{n}(\boldsymbol{r})) \cdot \boldsymbol{n}(\boldsymbol{r}). \tag{2.4}$$

Remark 2.1.1 *A few comments concerning notations are in order: (i)* $\Gamma_{j\ell}$ *may be empty for a number of pairs* (j, ℓ)*: for example* $\Gamma_{12} = \emptyset$ *for the geometry displayed in Figure 2.1a, and* $\Gamma_{j\ell}$ *is necessarily empty, by definition, whenever* $j \geq \ell$*. (ii) The use of indicator functions in equation* (2.1) *makes it possible to conveniently specify incident fields in an adequately selected SIW region* Ω^{inc} *(which equals the half plane containing the SIW that supports the incident field). (iii) Once u is determined by solving equation* (2.2)*, the total electromagnetic field in the domain* Ω_j *(*$j = 1, 2 \ldots N$*) is given by* $\boldsymbol{E} = (0, u, 0)$*,* $\boldsymbol{H} = \frac{i}{\omega \mu_j} \left(\frac{\partial u}{\partial z}, 0, -\frac{\partial u}{\partial x} \right)$ *in TE-polarization, and* $\boldsymbol{E} = \frac{i\omega\mu_j}{k_j^2} \left(-\frac{\partial u}{\partial z}, 0, \frac{\partial u}{\partial x} \right)$*,* $\boldsymbol{H} = (0, u, 0)$ *in TM-polarization.*

2.2 Windowed Green Function Method (WGF)

2.2.1 Integral Equation Formulation

This section presents an integral equation formulation for the propagation and scattering problem considered in section 2.1. For simplicity (and without loss of generality) throughout this chapter, it is assumed that the structure is illuminated by means of an arbitrary superposition of bound modes incoming from a single SIW whose optical axis coincides with the $z-$axis; the generalization to structures containing multiple arbitrarily-oriented waveguides is straightforward. Under this assumption, the incident field is prescribed by

$$u^{\text{inc}}(z, x) = \sum_{m=1}^{M} A_m^{\text{inc}} u_{\perp}^m(x) \, \mathrm{e}^{i k_z^m z}, \tag{2.5}$$

where M is the total number of bound modes supported by the waveguide structure, A_m^{inc} denotes the m-th modal coefficient, $u_{\perp}^m(x)$ is the transverse profile of the mode, and k_z^m is the corresponding propagation constant for the m-th mode. Note that $u_{\perp}^m(x)$ and k_z^m can be easily found by solving a one dimensional eigenvalue problem by means of the method of separation of variables [56]. For example, the bound mode solutions for a single waveguide centered at $x = 0$, with half-width h and with

core and cladding wavenumbers $k_{\mathrm{co}} > k_{\mathrm{cl}}$ respectively, are given by [56]

$$u_{\perp}^{m}(x) = \begin{cases} v\left(\gamma_{\mathrm{co}}\, h\right) e^{-\gamma_{\mathrm{cl}}(x-h)} & , \quad x > h \\ v\left(\gamma_{\mathrm{co}}\, x\right) & , \quad |x| \leq h \\ v\left(-\gamma_{\mathrm{co}}\, h\right) e^{\gamma_{\mathrm{cl}}(x+h)} & , \quad x < -h, \end{cases} \tag{2.6}$$

where $\gamma_{\mathrm{co}} = \sqrt{k_{\mathrm{co}}^2 - (k_z^m)^2}$ and $\gamma_{\mathrm{cl}} = \sqrt{(k_z^m)^2 - k_{\mathrm{cl}}^2}$. Here $v(\tau) = \cos(\tau)$ for the symmetric modes, $v(\tau) = \sin(\tau)$ for the antisymmetric modes, and k_z^m ($k_{\mathrm{cl}} < k_z^m < k_{\mathrm{co}}$) is the m-th solution of the transcendental equation

$$\begin{cases} \gamma_{\mathrm{cl}} = \nu_{\mathrm{wg}} \gamma_{\mathrm{co}} \tan\left(\gamma_{\mathrm{co}} h\right) & \text{(symmetric mode)}, \\ \nu_{\mathrm{wg}} \gamma_{\mathrm{co}} = -\gamma_{\mathrm{cl}} \tan\left(\gamma_{\mathrm{co}} h\right) & \text{(antisymmetric mode)}, \end{cases} \tag{2.7}$$

with $\nu_{\mathrm{wg}} = 1$ for TE-polarization and $\nu_{\mathrm{wg}} = (k_{\mathrm{cl}}/k_{\mathrm{co}})^2$ for TM-polarization. As indicated in section 2.3, additional incident fields such as plane waves, and finite beams can also be incorporated easily in this context.

In order to introduce the desired system of integral equations, let

$$\Gamma_j = \left(\bigcup_{\ell=1}^{j-1} \Gamma_{\ell j} \right) \bigcup \left(\bigcup_{\ell=j+1}^{N} \Gamma_{j\ell} \right) \tag{2.8}$$

denote the boundary of the domain Ω_j and let $\Gamma = \bigcup_{j=1}^{N} \Gamma_j$ denote the union of all domain boundaries. Then, calling

$$\varphi(\boldsymbol{r}) \equiv u_+(\boldsymbol{r}) \quad \text{and} \quad \psi(\boldsymbol{r}) \equiv \frac{\partial u_+}{\partial \boldsymbol{n}}(\boldsymbol{r}), \quad \boldsymbol{r} \in \Gamma, \tag{2.9}$$

and using Green's theorem in a manner akin to [37] together with the boundary conditions in equation (2.2), the representation formula

$$u(\boldsymbol{r}) = \mathscr{D}[\beta_j \varphi](\boldsymbol{r}) - \mathscr{S}\left[\beta_j \nu_j^{-1} \psi\right](\boldsymbol{r}), \quad \boldsymbol{r} \in \Omega_j \tag{2.10}$$

results, where

$$[\beta_j(\boldsymbol{r}), \nu_j(\boldsymbol{r})] = \begin{cases} [1, 1], & \text{for } \boldsymbol{r} \in \Gamma_{j\ell}\ (j < \ell) \\ [-1, \nu_{\ell j}], & \text{for } \boldsymbol{r} \in \Gamma_{\ell j}\ (j > \ell) \end{cases}, \tag{2.11}$$

and where, letting $G_j(\boldsymbol{r}, \boldsymbol{r}') = \frac{i}{4} H_0^{(1)}(k_j|\boldsymbol{r} - \boldsymbol{r}'|)$ denote the free-space Green function for the Helmholtz equation with wavenumber k_j, the single and double layer potentials $\mathscr{S}$ and $\mathscr{D}$ for a given density η defined in Γ are given by

$$\mathscr{S}[\eta](\boldsymbol{r}) = \int_{\Gamma_j} G_j(\boldsymbol{r}, \boldsymbol{r}')\eta(\boldsymbol{r}')\mathrm{d}s_{\boldsymbol{r}'}, \qquad \boldsymbol{r} \in \Omega_j, \tag{2.12}$$

$$\mathscr{D}[\eta](\boldsymbol{r}) = \int_{\Gamma_j} \frac{\partial G_j(\boldsymbol{r}, \boldsymbol{r}')}{\partial \boldsymbol{n}(\boldsymbol{r}')}\eta(\boldsymbol{r}')\mathrm{d}s_{\boldsymbol{r}'}, \qquad \boldsymbol{r} \in \Omega_j. \tag{2.13}$$

The densities φ and ψ in the representation formula in equation (2.10), which, in view of equation (2.9), are given in terms of the total field, can be expressed as a sum of their incident and scattered components. In other words, $\varphi = \varphi^{\mathrm{inc}} + \varphi^{\mathrm{scat}}$ and $\psi = \psi^{\mathrm{inc}} + \psi^{\mathrm{scat}}$ where, using the indicator function in equation (2.1), for $\boldsymbol{r} \in \Gamma$

$$\varphi^{\mathrm{inc}}(\boldsymbol{r}) \equiv \chi^{\mathrm{inc}}(\boldsymbol{r})u_+^{\mathrm{inc}}(\boldsymbol{r}) \ \text{ and } \ \psi^{\mathrm{inc}}(\boldsymbol{r}) \equiv \chi^{\mathrm{inc}}\frac{\partial u_+^{\mathrm{inc}}(\boldsymbol{r})}{\partial \boldsymbol{n}}, \tag{2.14}$$

$$\varphi^{\mathrm{scat}}(\boldsymbol{r}) \equiv u_+^{\mathrm{scat}}(\boldsymbol{r}) \ \text{ and } \ \psi^{\mathrm{scat}}(\boldsymbol{r}) \equiv \frac{\partial u_+^{\mathrm{scat}}(\boldsymbol{r})}{\partial \boldsymbol{n}}. \tag{2.15}$$

Note the important difference that originates from having an incident field given by bound modes (compared to incident plane waves): the total field—not just the scattered component—has an integral equation representation.

The desired integral equations for the unknown densities φ^{scat} and ψ^{scat} are expressed in terms of certain free-space Green functions and various associated integral operators. The particular Green function used in the definition of each one of these operators depends on $\boldsymbol{r}$: for $\boldsymbol{r} \in \Gamma_{j\ell}$, a "plus" (resp. "minus") operator uses the Green function G_j (resp. G_ℓ) corresponding to the refractive index on the plus side (resp. minus side) of $\Gamma_{j\ell}$. To streamline the notations in this context, for $\boldsymbol{r} \in \Gamma$ let $\Gamma^{\pm}(\boldsymbol{r})$ be defined as follows: if $\boldsymbol{r} \in \Gamma_{j\ell}$, then $\Gamma^{+}(\boldsymbol{r}) = \Gamma_j$ and $\Gamma^{-}(\boldsymbol{r}) = \Gamma_\ell$ (cf. Remark 2.1.1). The necessary integral operators are thus defined by

$$\begin{aligned}
S^{\pm}[\eta](\boldsymbol{r}) &= \int_{\Gamma^{\pm}(\boldsymbol{r})} G^{\pm}(\boldsymbol{r}, \boldsymbol{r}')\eta(\boldsymbol{r}')ds_{\boldsymbol{r}'}, \ \boldsymbol{r} \in \Gamma, \\
D^{\pm}[\eta](\boldsymbol{r}) &= \int_{\Gamma^{\pm}(\boldsymbol{r})} \frac{\partial G^{\pm}(\boldsymbol{r}, \boldsymbol{r}')}{\partial \boldsymbol{n}(\boldsymbol{r}')}\eta(\boldsymbol{r}')ds_{\boldsymbol{r}'}, \ \boldsymbol{r} \in \Gamma, \\
K^{\pm}[\eta](\boldsymbol{r}) &= \int_{\Gamma^{\pm}(\boldsymbol{r})} \frac{\partial G^{\pm}(\boldsymbol{r}, \boldsymbol{r}')}{\partial \boldsymbol{n}(\boldsymbol{r})}\eta(\boldsymbol{r}')ds_{\boldsymbol{r}'}, \ \boldsymbol{r} \in \Gamma, \\
N^{\pm}[\eta](\boldsymbol{r}) &= \int_{\Gamma^{\pm}(\boldsymbol{r})} \frac{\partial^2 G^{\pm}(\boldsymbol{r}, \boldsymbol{r}')}{\partial \boldsymbol{n}(\boldsymbol{r})\partial \boldsymbol{n}(\boldsymbol{r}')}\eta(\boldsymbol{r}')ds_{\boldsymbol{r}'}, \ \boldsymbol{r} \in \Gamma.
\end{aligned} \tag{2.16}$$

As is known (cf. [32] theorems 3.1 and 3.2), the layer potentials from equation (2.13) satisfy the jump conditions at $\boldsymbol{r} \in \Gamma$:

$$\begin{aligned}
\lim_{\delta\to 0^+} \mathscr{S}[\eta](\boldsymbol{r} \pm \delta\boldsymbol{n}(\boldsymbol{r})) &= S^{\pm}[\eta](\boldsymbol{r}),\\
\lim_{\delta\to 0^+} \mathscr{D}[\eta](\boldsymbol{r} \pm \delta\boldsymbol{n}(\boldsymbol{r})) &= \pm\frac{1}{2}\eta(\boldsymbol{r}) + D^{\pm}[\eta](\boldsymbol{r}),\\
\lim_{\delta\to 0^+} \frac{\partial}{\partial\boldsymbol{n}}\mathscr{D}[\eta](\boldsymbol{r} \pm \delta\boldsymbol{n}(\boldsymbol{r})) &= N^{\pm}[\eta](\boldsymbol{r}),\\
\lim_{\delta\to 0^+} \frac{\partial}{\partial\boldsymbol{n}}\mathscr{S}[\eta](\boldsymbol{r} \pm \delta\boldsymbol{n}(\boldsymbol{r})) &= \mp\frac{1}{2}\eta(\boldsymbol{r}) + K^{\pm}[\eta](\boldsymbol{r}).
\end{aligned} \tag{2.17}$$

Thus, adding the limits of the fields in equation (2.10) (resp. the normal derivatives of the fields in equation (2.10)) on the plus and minus sides of Γ, the system of integral equations for $\boldsymbol{r} \in \Gamma$

$$E(\boldsymbol{r})\boldsymbol{\Phi}^{\mathrm{scat}}(\boldsymbol{r}) + T[\boldsymbol{\Phi}^{\mathrm{scat}}](\boldsymbol{r}) = -E(\boldsymbol{r})\boldsymbol{\Phi}^{\mathrm{inc}}(\boldsymbol{r}) - T[\boldsymbol{\Phi}^{\mathrm{inc}}](\boldsymbol{r}), \tag{2.18}$$

results, where $E(\boldsymbol{r}) = \mathrm{diag}\left[1, \dfrac{1+\nu(\boldsymbol{r})}{2\nu(\boldsymbol{r})}\right]$ and

$$\nu(\boldsymbol{r}) = \nu_{\ell j}, \quad \text{for } \boldsymbol{r} \in \Gamma_{j\ell}\ (j < \ell), \tag{2.19}$$

$$T = \begin{bmatrix} D^- - D^+ & S^+ - (1/\nu)S^- \\ N^- - N^+ & K^+ - (1/\nu)K^- \end{bmatrix}, \tag{2.20}$$

and where the density vectors are given by

$$\boldsymbol{\Phi}^{\mathrm{scat}} = [\varphi^{\mathrm{scat}}, \psi^{\mathrm{scat}}]^{\mathrm{T}}, \quad \text{and} \quad \boldsymbol{\Phi}^{\mathrm{inc}} = [\varphi^{\mathrm{inc}}, \psi^{\mathrm{inc}}]^{\mathrm{T}}. \tag{2.21}$$

2.2.2 Oscillatory integrals and the slow-rise windowing function

Special considerations must be taken into account in order to solve the system of equations (2.18) numerically—mainly in view of the slow decay of the associated integrands (equation (2.16)) for a fixed target point $\boldsymbol{r} \in \Gamma$ as $\boldsymbol{r}' \to \infty$. A direct truncation of the integration domain (i.e., replacement of the integrals in (2.16) by corresponding integrals over the domain $\Gamma^{\pm}(\boldsymbol{r}) \cap \{|\boldsymbol{r}| \le A\}$) yields slow convergence, on account of edge effects, as the size A of the truncation domain tends to infinity. Relying on a certain slow-rise windowing technique that smoothly truncates the integration domain, the proposed approach addresses this difficulty—and, in fact, it gives rise to a super-algebraically convergent algorithm. The resulting windowed integral equations can be subsequently discretized by means of any integral solver, including, in particular, the Method of Moments [73], or, indeed, any Nyström,

Galerkin or collocation approach. The particular implementations presented in this chapter are based on the high-order Nyström method described in [32, Sec. 3.5].

The proposed methodology is based on use of an infinitely smooth function $\widetilde{w}_A(d)$, defined for $d \in \mathbb{R}$, which satisfies the following properties: (i) $\widetilde{w}_A(d)$ vanishes for d outside the interval $[-A, A]$; (ii) $\widetilde{w}_A(d)$ equals 1 for $d \in (-\alpha A, \alpha A)$ for some α satisfying $0 < \alpha < 1$; (iii) All of the derivatives $\widetilde{w}_A^{(p)}(d)$ (p a positive integer) vanish at $d = \pm A$ and $d = \pm\alpha A$; and (iv) $\widetilde{w}_A(d)$ exhibits a "slow-rise" from 0 to 1 as $|d|$ goes from $|d| = A$ to $|d| = \alpha A$—in the sense that each derivative of $\widetilde{w}_A$, of any given order, tends to zero everywhere (and, in particular, in the rise intervals $\alpha A \leq |d| \leq A$) as $d \to \infty$. The windowing function used is given by

$$\widetilde{w}_A(d) = \begin{cases} 1, & s < 0 \\ \exp\left(-2\dfrac{\exp\left(-1/|s|^2\right)}{|1-s|^2} \right), & 0 \leq s \leq 1 \\ 0, & s > 1 \end{cases}, \tag{2.22}$$

where $s(d) = \frac{|d|-\alpha A}{A(1-\alpha)}$, but other choices could be equally suitable [13]. (In fact, window functions that only satisfy condition (iii) up to a certain tolerance could be used, such as e.g. window functions based on the error function or the hyperbolic tangent.) As shown in [13] and demonstrated by means of a simple example in section 2.2.3, the properties (i) through (iv) ensure that certain improper integrals with slowly decaying oscillatory integrands—like the integrands in equation (2.16); see Remark 2.2.1—can be evaluated, with super-algebraic accuracy, via windowing based on the function $\widetilde{w}_A(d)$. Suitable centered versions $w_A(\boldsymbol{r})$ (Figure 2.1b) of the window function $\widetilde{w}_A(d)$ are used in section 2.2.4 to window integral operators defined on general waveguide structures.

Remark 2.2.1 *In view of the asymptotic expressions for the Hankel function, each one of the integral kernels involved in the equation system* (2.18) *can be expressed in the form* $h(t)\exp(it)$ *where* $t = k|\boldsymbol{r} - \boldsymbol{r}'| = k|z - z'|\sqrt{1 + (\frac{x-x'}{z-z'})^2}$ *and where* $h(t) \sim t^{-1/2}$ $(t \to \infty)$ *is a function whose derivatives of any order are bounded for all* $t > 1$ *[54, Sec. 5.11] (see also [20, 35]). On the other hand, the scattered densities* φ^{scat} *approach oscillatory asymptotic functions as* $\boldsymbol{r}' = (z', x')$ *tends to infinity along* $\Gamma^{\pm}(\boldsymbol{r})$ *[67]:* $\varphi^{scat} \sim \sum_m A_m^{scat} u_\perp^m(x') e^{-ik_z^m z'}$ *as* $z' \to -\infty$ *and* $\varphi^{scat} \sim \sum_n B_n^{scat} u_\perp^n(x') e^{ik_z^n z'}$ *as* $z' \to +\infty$*, with similar expressions for the density* ψ^{scat}*. Combining the kernel and density asymptotics, it follows that the net integrands*

in the operators (2.16) *equal sums of slowly decaying oscillatory functions with wavenumbers* $\pm(k + k_z^n)$.

2.2.3 Error estimates for a simplified windowed integral

In order to illustrate the properties of the windowed-integration method, it is useful to consider here a simple integration problem presented in [13], namely, the problem of numerical evaluation of the integral

$$I = \int_1^\infty \frac{\mathrm{e}^{i\kappa z}}{\sqrt{z}} dz, \tag{2.23}$$

where κ is a real constant; see, in particular, [13, theorem 3.1]. Letting $I_{\mathrm{tr}}(A) = \int_1^A \frac{\mathrm{e}^{i\kappa z}}{\sqrt{z}} dz$, $I_w(A) = \int_1^A \widetilde{w}_A(z) \frac{\mathrm{e}^{i\kappa z}}{\sqrt{z}} dz$, then, by definition $I = \lim_{A\to\infty} I_{\mathrm{tr}}(A)$. As is known, the value of I is finite—in spite of the slow decay of the integrand (the integral of the function $1/\sqrt{z}$ in the same domain is infinite!). The finiteness of the improper integral between 1 and ∞, which results from cancellation of positive and negative contributions arising from the oscillatory factor $\mathrm{e}^{i\kappa z}$, may be verified by integrating by parts the integral $I_{\mathrm{tr}}(A)$ (differentiating $1/\sqrt{z}$ and integrating $\mathrm{e}^{i\kappa z}$). This procedure produces two terms: (i) An integral with a more rapidly decaying integrand and whose convergence does not rely on cancellations, as well as (ii) Boundary contributions at $z = 1$ and $z = A$. Besides establishing the existence of the limit $\lim_{A\to\infty} I_{\mathrm{tr}}(A)$, this expression tells us that the $z = A$ boundary contribution $1/(i\kappa\sqrt{A})\,\mathrm{e}^{i\kappa A}$ equals the error in the approximation of I by $I_{\mathrm{tr}}(A)$. On the other hand, use of integration by parts on $I_w(A)$ does not give rise to a boundary contribution for $z = A$—on account of the fact that $\widetilde{w}_A(A) = \widetilde{w}'_A(A) = 0$. In fact, since all the derivatives of $\widetilde{w}_A(z)$ vanish at $z = A$, the integration by parts procedure can be performed on $I_w(A)$ an arbitrary number p of times without ever producing a boundary contribution—a fact which lies at the heart of the accuracy resulting from the slow-rise windowing approach. As shown in [13, theorem 3.1], this procedure leads to the error estimates

$$|I - I_{\mathrm{tr}}(A)| = O\left(\frac{1}{\kappa\sqrt{A}}\right), \quad |I - I_w(A)| = O\left(\frac{1}{\sqrt{\kappa}(\kappa A)^{p-\frac{1}{2}}}\right), \tag{2.24}$$

for every $p \geq 1$. These estimates are corroborated by the results in Table 2.1.

2.2.4 Windowed integral equations

Per Remark 2.2.1, for a fixed $\boldsymbol{r} \in \Gamma$, the integrands associated with the operators on the left-hand side of equation (2.18) are oscillatory and slowly decaying at

Table 2.1: Convergence of the windowed integrals $I_{\text{tr}}(A)$ and $I_w(A)$ with $\kappa = 2\pi$ and window parameter $\alpha = 0.5$

A	$\lvert I - I_{\text{tr}}(A)\rvert$	$\lvert I - I_w(A)\rvert$
10	5.0×10^{-2}	3.6×10^{-3}
20	3.6×10^{-2}	5.8×10^{-5}
25	3.2×10^{-2}	9.3×10^{-6}
50	2.2×10^{-2}	3.1×10^{-9}
75	1.8×10^{-2}	3.1×10^{-12}
100	1.6×10^{-2}	1.0×10^{-14}

infinity—just like the integrand in the simplified example presented in section 2.2.3. Thus, it is expected that use of windowing in the integrands of these operators should result in convergence properties analogous to the ones described in that section. Since the integrands on the right-hand side (RHS) of equation (2.18) are known functions, and since, as shown below, the full RHS can be evaluated efficiently (by relying on equation (2.27)), the use of windowing may be restricted to the left-hand side operators.

These considerations lead to the following system of "windowed" integral equations on the *bounded* domain $\widetilde{\Gamma} = \Gamma \cap \{w_A(\boldsymbol{r}) \neq 0\}$:

$$E(\boldsymbol{r})\boldsymbol{\Phi}_w^{\text{scat}}(\boldsymbol{r}) + T[w_A\boldsymbol{\Phi}_w^{\text{scat}}](\boldsymbol{r}) = -E(\boldsymbol{r})\boldsymbol{\Phi}^{\text{inc}}(\boldsymbol{r}) - T[\boldsymbol{\Phi}^{\text{inc}}](\boldsymbol{r}), \tag{2.25}$$

for $\boldsymbol{r} \in \widetilde{\Gamma}$. A discrete version of equations (2.25) can be obtained by substituting all left-hand side integrals by adequate quadrature rules (as mentioned above, the Nyström method [32, Sec. 3.5] is used for this purpose). The windowing function $w_A(\boldsymbol{r})$ used here is selected as follows: (i) $w_A(\boldsymbol{r}) = 1$ on any portion of Γ that is not part of a SIW; (ii) $w_A(\boldsymbol{r}) = \widetilde{w}_A(d_q(\boldsymbol{r}))$ along any portion of Γ that is contained in the q-th SIW, and where $d_q(\boldsymbol{r})$ is the distance to the edge of the aforementioned SIW (see Figure 2.1b). As demonstrated in section 2.3 through a variety of numerical results, the solution $\boldsymbol{\Phi}_w^{\text{scat}}$ of equation (2.25) provides a super-algebraically accurate approximation to $\boldsymbol{\Phi}^{\text{scat}}$ throughout the region $\{w_A(\boldsymbol{r}) = 1\}$.

Note that the net wavenumber of the integrands in the RHS of equation (2.25) can be arbitrarily small, since the phase of the exponentials in (2.5) can be arbitrarily close to the negative of the phase of the kernels (see Remark 2.2.1). Thus a direct windowed computation of $T[\boldsymbol{\Phi}^{\text{inc}}](\boldsymbol{r})$ generally presents a considerable challenge. In order to obtain these integrals, a strategy that doesn't rely on the oscillatory nature of the integrands was devised. To introduce this alternative strategy, consider the

discussion leading to equation (2.18). Clearly, the first (resp. second) component in the quantity $[\xi, \eta]^{\mathrm{T}} = T[\mathbf{\Phi}^{\mathrm{inc}}](\boldsymbol{r})$ for $\boldsymbol{r} \in \widetilde{\Gamma}$ is given by the limit as $\boldsymbol{r}$ tends to $\widetilde{\Gamma}$ of the field u (resp. the normal derivative of the field u) that results as the pair $[\phi, \psi]^{\mathrm{T}}$ in (2.10) is replaced by the incident densities $[\phi^{\mathrm{inc}}, \psi^{\mathrm{inc}}]^{\mathrm{T}} (= \mathbf{\Phi}^{\mathrm{inc}})$. Note that, per equation (2.14), $\mathbf{\Phi}^{\mathrm{inc}}$ vanishes identically outside $\Gamma_j^{\mathrm{inc}} = \Gamma_j \cap \Omega^{\mathrm{inc}}$. Now, given that the illuminating structure is a single SIW whose optical axis coincides with the $z-$axis (as indicated in section 2.2.1), the corresponding integration domain Γ_j^{inc} can be decomposed as the union $\Gamma_j^{\mathrm{inc}} = \widetilde{\Gamma}_j^{\mathrm{inc}} \cup \Gamma_j^{\infty}$ of the two disjoint segments $\widetilde{\Gamma}_j^{\mathrm{inc}} = \Gamma_j^{\mathrm{inc}} \cap \{w_A(\boldsymbol{r}) \neq 0\}$ and $\Gamma_j^{\infty} = \Gamma_j^{\mathrm{inc}} \cap \{w_A(\boldsymbol{r}) = 0\}$. (With reference to Figure 2.1b note that $\Gamma_j^{\mathrm{inc}} = \left(\bigcup_{\ell=1}^{j-1} \Gamma_{\ell j}^{\mathrm{inc}}\right) \bigcup \left(\bigcup_{\ell=j+1}^{N} \Gamma_{j\ell}^{\mathrm{inc}}\right)$ where $\Gamma_{j\ell}^{\mathrm{inc}} = \Gamma_{j\ell} \cap \Omega^{\mathrm{inc}}$; similarly, $\widetilde{\Gamma}_j^{\mathrm{inc}}$ and Γ_j^{∞} are decomposed as the unions of the curves $\widetilde{\Gamma}_{j\ell}^{\mathrm{inc}} = \Gamma_{j\ell}^{\mathrm{inc}} \cap \{w_A(\boldsymbol{r}) \neq 0\}$ and $\Gamma_{j\ell}^{\infty} = \Gamma_{j\ell}^{\mathrm{inc}} \cap \{w_A(\boldsymbol{r}) = 0\}$, respectively. Figure 2.1b only displays the independent components $\widetilde{\Gamma}_{j\ell}^{\mathrm{inc}}$ and $\Gamma_{j\ell}^{\infty}$.) Using the fact that the incident densities φ^{inc} and ψ^{inc} vanish outside Γ_j^{inc}, for $\boldsymbol{r} \in \Omega_j$ the relation

$$\mathscr{D}[\beta_j \varphi^{\mathrm{inc}}] - \mathscr{S}\left[\beta_j \nu_j^{-1} \psi^{\mathrm{inc}}\right] = \int_{\widetilde{\Gamma}_j^{\mathrm{inc}} \cup \Gamma_j^{\infty}} \beta_j \times \left[\frac{\partial G_j(\boldsymbol{r}, \boldsymbol{r}')}{\partial \boldsymbol{n}(\boldsymbol{r}')} \varphi^{\mathrm{inc}}(\boldsymbol{r}') - G_j(\boldsymbol{r}, \boldsymbol{r}') \nu_j^{-1} \psi^{\mathrm{inc}}(\boldsymbol{r}')\right] \mathrm{d}s_{\boldsymbol{r}'}, \tag{2.26}$$

results. The evaluation of the right-hand integral is discussed in what follows.

The integral over the *bounded* curve $\widetilde{\Gamma}_j^{\mathrm{inc}}$ in (2.26) can be computed using any of the standard singular-integration techniques mentioned in section 2.2.2. The curve Γ_j^{∞} extends to infinity, on the other hand, with an integrand that decays slowly (see Remark 2.2.1). Fortunately, however, the Γ_j^{∞} integration problem can be significantly simplified by relying on the fact that $[\varphi^{\mathrm{inc}}, \psi^{\mathrm{inc}}]^{\mathrm{T}} (= \mathbf{\Phi}^{\mathrm{inc}})$ actually coincides with the boundary values of the incident field and its normal derivative, as indicated in equation (2.14). To evaluate the Γ_j^{∞} integral, consider the identity

$$\begin{aligned} &\int_{\Gamma_j^{\infty}} \beta_j \left[\frac{\partial G_j(\boldsymbol{r}, \boldsymbol{r}')}{\partial \boldsymbol{n}(\boldsymbol{r}')} \varphi^{\mathrm{inc}}(\boldsymbol{r}') - G_j(\boldsymbol{r}, \boldsymbol{r}') \nu_j^{-1} \psi^{\mathrm{inc}}(\boldsymbol{r}')\right] \mathrm{d}s_{\boldsymbol{r}'} \\ &= -\int_{\Gamma_j^{\perp}} \beta_j \left[\frac{\partial G_j(\boldsymbol{r}, \boldsymbol{r}')}{\partial \boldsymbol{n}(\boldsymbol{r}')} u^{\mathrm{inc}}(\boldsymbol{r}') - G_j(\boldsymbol{r}, \boldsymbol{r}') \frac{\partial u^{\mathrm{inc}}}{\partial \boldsymbol{n}}(\boldsymbol{r}')\right] \mathrm{d}s_{\boldsymbol{r}'}, \end{aligned} \tag{2.27}$$

for $\boldsymbol{r} \in \{z > -A\}$ that results by using Green's theorem in a manner akin to [37] (the corresponding bounded-domain result can be found e.g. in [31, theorem 3.1]). (Here $\Gamma_j^{\perp} = \Omega_j \cap \{z = -A\}$ is such that $\Gamma_j^{\perp} \cup \Gamma_j^{\infty}$ is the boundary of the region $\Omega_j \cap \{z < -A\}$, see Figure 2.1b.) Equation (2.27) provides an alternative approach

for the evaluation of the integrals over Γ_j^∞ in equation (2.26). While some of the $\Gamma_j^\perp$ curves are unbounded, along such unbounded curves the fields decay *exponentially fast* (see equation (2.6)), and, thus, arbitrary accuracy can efficiently be achieved in the corresponding integrals by truncation of the integration domain to a relatively small bounded portion of $\Gamma_j^\perp$. It is worthwhile to emphasize that the substitution of the right-hand side of (2.25) by quantities evaluated in terms of equations (2.27) and (2.26), as explained above in this section, amounts to a non-standard procedure which significantly facilitates the implementation of the proposed methodology in the case of bound-mode excitations.

The overall WGF method for open waveguides is summarized in points (1) to (3) below. As mentioned above, the bounded-interval numerical integrations mentioned in the points (1) to (3) can be effected by means of any numerical integration method applicable to the kinds of singular integrals (with singular kernels and, at corners, unknown singular densities) associated with the problems under consideration. The implementation used to produce the numerical results in section 2.3 relies on numerical integration methods derived from [32, Sec. 3.5].

The WGF algorithm proceeds as follows:

(1) Evaluate the RHS of equation (2.25) by decomposing the integrals in the operators (2.20) into integrals over $\widetilde{\Gamma}_j^{\text{inc}}$ and Γ_j^∞. The integrals involving the bounded integration domains $\widetilde{\Gamma}_j^{\text{inc}}$ are computed by direct numerical integration. Relying on the exponential decay of the integrands of the RHS of equation (2.27), on the other hand, the integrals over Γ_j^∞ are obtained by truncation of the integrals over $\Gamma_j^\perp$.

(2) Solve for $\mathbf{\Phi}_w^{\text{scat}}$ in equation (2.25) by either inverting directly the corresponding discretized system (as is done here), or by means of a suitable iterative linear-algebra solver, if preferred.

(3) Evaluate the approximate fields u_w using the representation formula (2.10) in conjunction with equation (2.27):

$$\begin{aligned} u_w(\boldsymbol{r}) =& \mathscr{D}[\beta_j w_A \varphi_w^{\text{scat}}](\boldsymbol{r}) - \mathscr{S}\left[\beta_j \nu_j^{-1} w_A \psi_w^{\text{scat}}\right](\boldsymbol{r}) \\ &+ \mathscr{D}[\beta_j \varphi^{\text{inc}}](\boldsymbol{r}) - \mathscr{S}\left[\beta_j \nu_j^{-1} \psi^{\text{inc}}\right](\boldsymbol{r}), \end{aligned} \tag{2.28}$$

for $\boldsymbol{r} \in \Omega_j$, and where the layer potentials involving φ^{inc} and ψ^{inc} are computed as in point 1, that is, by direct evaluation of the integrals over $\widetilde{\Gamma}_j^{\text{inc}}$ and via equation (2.27) for the integrals over Γ_j^∞.

It can be seen [20] that, as $A \to \infty$, the fields in point 3 are super-algebraically accurate in any bounded region in the plane.

2.3 Numerical examples

This section demonstrates the character of the WGF method introduced in section 2.2 through a variety of numerical results. These results were obtained by means of a MATLAB implementation of the algorithms described in section 2.2.4 on a six-core 3.40 GHz Intel i7-4930K Processor with 12 Mb of cache and 32 GB of RAM. As mentioned in section 2.2.2, a Nyström method was utilized, where the number of points per wavelength was selected in such a way that the dominant error arises from the windowed truncation. The simulations in this section resulted from discretizations containing a number of eight to twelve points per wavelength, as needed to guarantee the accuracy reported for each numerical solution. The reported errors were evaluated via the expression

$$\text{Error} = \sqrt{\frac{\sum_{i=1}^{N_d} |u_w(\boldsymbol{r}_i) - u^{\text{ref}}(\boldsymbol{r}_i)|^2}{\sum_{i=1}^{N_d} |u^{\text{ref}}(\boldsymbol{r}_i)|^2}} \tag{2.29}$$

with $N_d = 100$, and where the N_d points $\boldsymbol{r}_i$ lie along certain curves, selected in different manners for each test case, along which significant features of the numerically computed fields were observed. The errors in all the nonuniform waveguide problems were evaluated on the basis of equation (2.29) with reference solutions u^{ref} produced by means of window functions w_A with $A/\lambda > 20$. In what follows, for a length unit $[L]$ relevant in a given application, the quantities A, λ and h (resp. k) below are taken to quantify lengths in the unit $[L]$ (resp. $[L]^{-1}$). If the selection $[L] = \mu m$ were made for the COUPLER test case, for example, the quantities k_{co} and k_{cl} would equal $2\pi\ \mu m^{-1}$ and $\pi\ \mu m^{-1}$, while h and the waveguide separation would equal $0.5\ \mu m$ and $0.2\ \mu m$, respectively. Of course, any other length units could be used, e.g. $[L] = \lambda_0$, where λ_0 denotes the electromagnetic wavelength in vacuum.

The first numerical example considered here is a simple uniform waveguide—for which, physically, a single mode (equation (2.6)), or even a superposition of such modes, can propagate from $-\infty$ to $+\infty$ without disturbance. This simple problem provides a direct test for the accuracy of the proposed WGF approach, for which errors were evaluated by using exact solutions as references: $u^{\text{ref}} = u$ in this case. The incident field was prescribed on the region $\Omega^{\text{inc}} = \{z \leq 0\}$. The observed error as a function of the window size is displayed in Figure 2.2 under the label "FLAT."

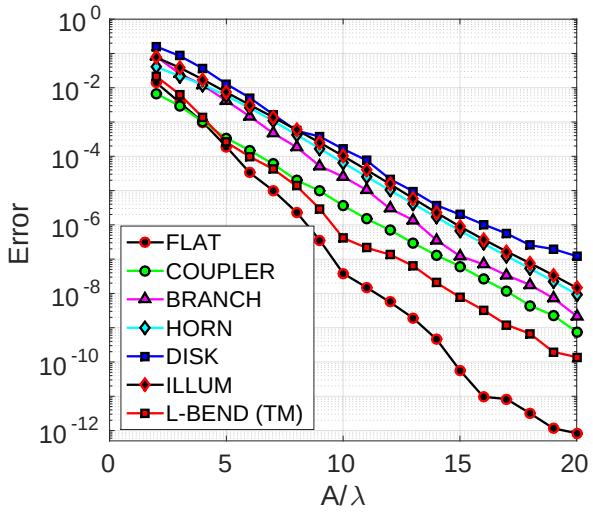

Figure 2.2: Super-algebraic convergence of the WGF method for various test configurations. In all cases, a sufficiently fine numerical grid was used (eight to twelve points per wavelength) to ensure the leading error is caused by the WGF's slow-rise boundary truncation. Here the scaled window size A/λ is varied while $\lambda = \max_j(2\pi/k_j)$ is kept fixed. The values of k_j are described in the text for each test case.

Error curves for a number of additional configurations are also included in Figure 2.2, and corresponding near field images are displayed in Figures 2.3 and 2.4. (The "trivial" near field image for the uniform waveguide mentioned above is not included in Figures 2.3 and 2.4.) The configurations considered (under TE or TM polarizations, as indicated in each case) are as follows:

- COUPLER (TE). Optical coupler illuminated by the first symmetric mode incoming from the top-left SIW. Waveguide core wavenumber $k_{\text{co}} = 2\pi$, cladding wavenumber $k_{\text{cl}} = \pi$ and waveguide half-width $h = 0.5$ were used. The waveguide separation in the cross-talk region was set to 0.2.

- BRANCH (TE). Branching waveguide structure illuminated by the first antisymmetric mode incoming from the left SIW. The half-widths of the horizontal, top-right and bottom-right SIWs are 1, 0.5 and 0.25, respectively, and the angle between the two branching waveguides is $5\pi/12$ radians. The bottom-right SIW is a single-mode waveguide: only one specific mode can propagate along this structure. The wavenumbers in the core, cladding and circular obstacle regions are $k_{\text{co}} = 2\pi$, $k_{\text{cl}} = \pi$ and $k_{\text{ob}} = 5\pi/2$, respectively.

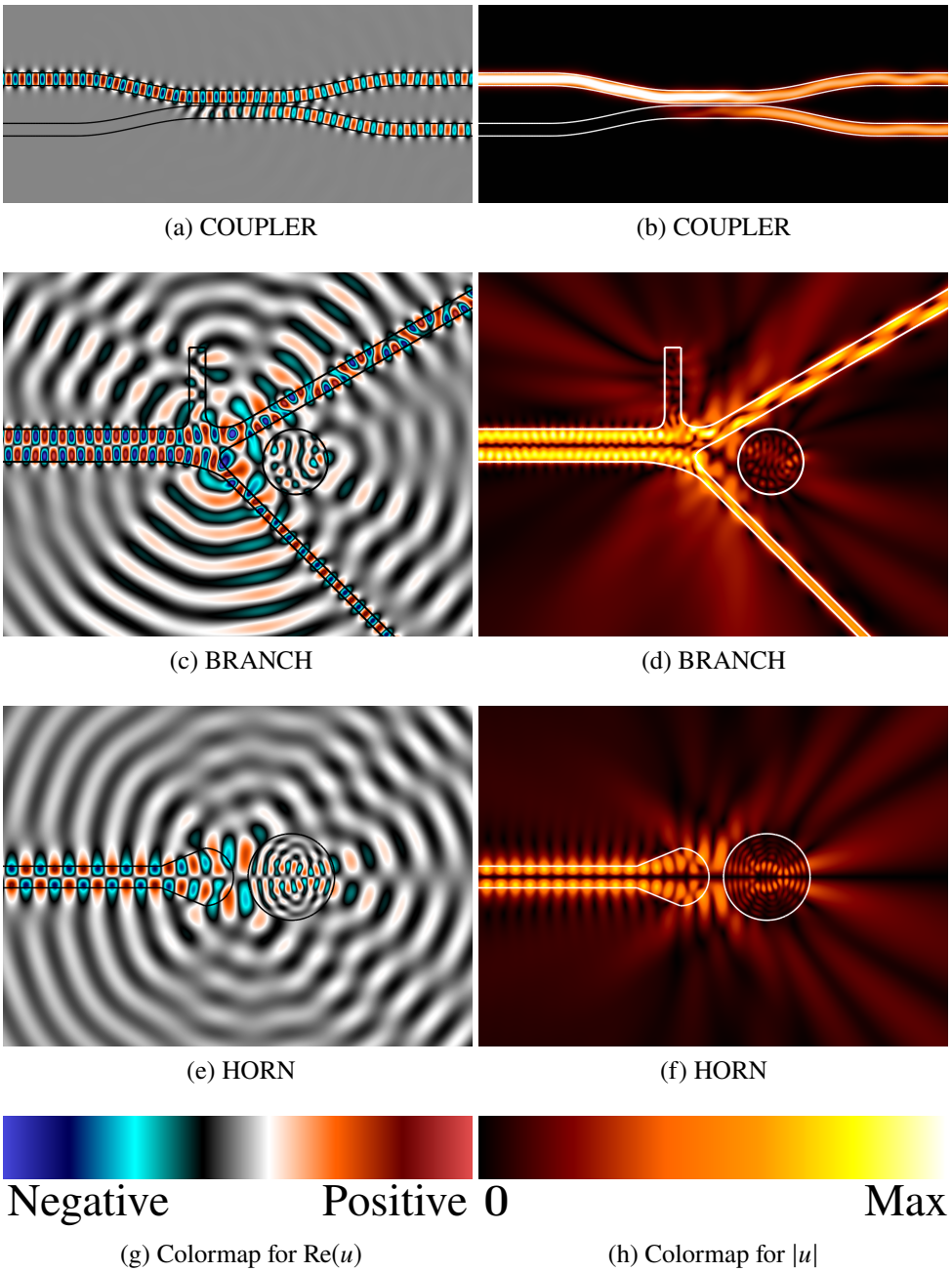

(a) COUPLER (b) COUPLER

(c) BRANCH (d) BRANCH

(e) HORN (f) HORN

(g) Colormap for Re(u) (h) Colormap for $|u|$

Figure 2.3: Real part and absolute value of u_w (left and right columns, respectively) produced by the WGF method for several open-waveguide problems.

- HORN (TE). Terminated waveguide horn antenna illuminating a dielectric circular obstacle. The system is illuminated by the first antisymmetric mode of the waveguide. The core and cladding wavenumbers are $k_{\text{co}} = 2\pi$ and $k_{\text{cl}} = 4\pi/3$ respectively, and the circular obstacle wavenumber is $k_{\text{ob}} = 4\pi$. The half-width of the waveguide is $h = 0.5$ and the radius of the obstacle is 2.

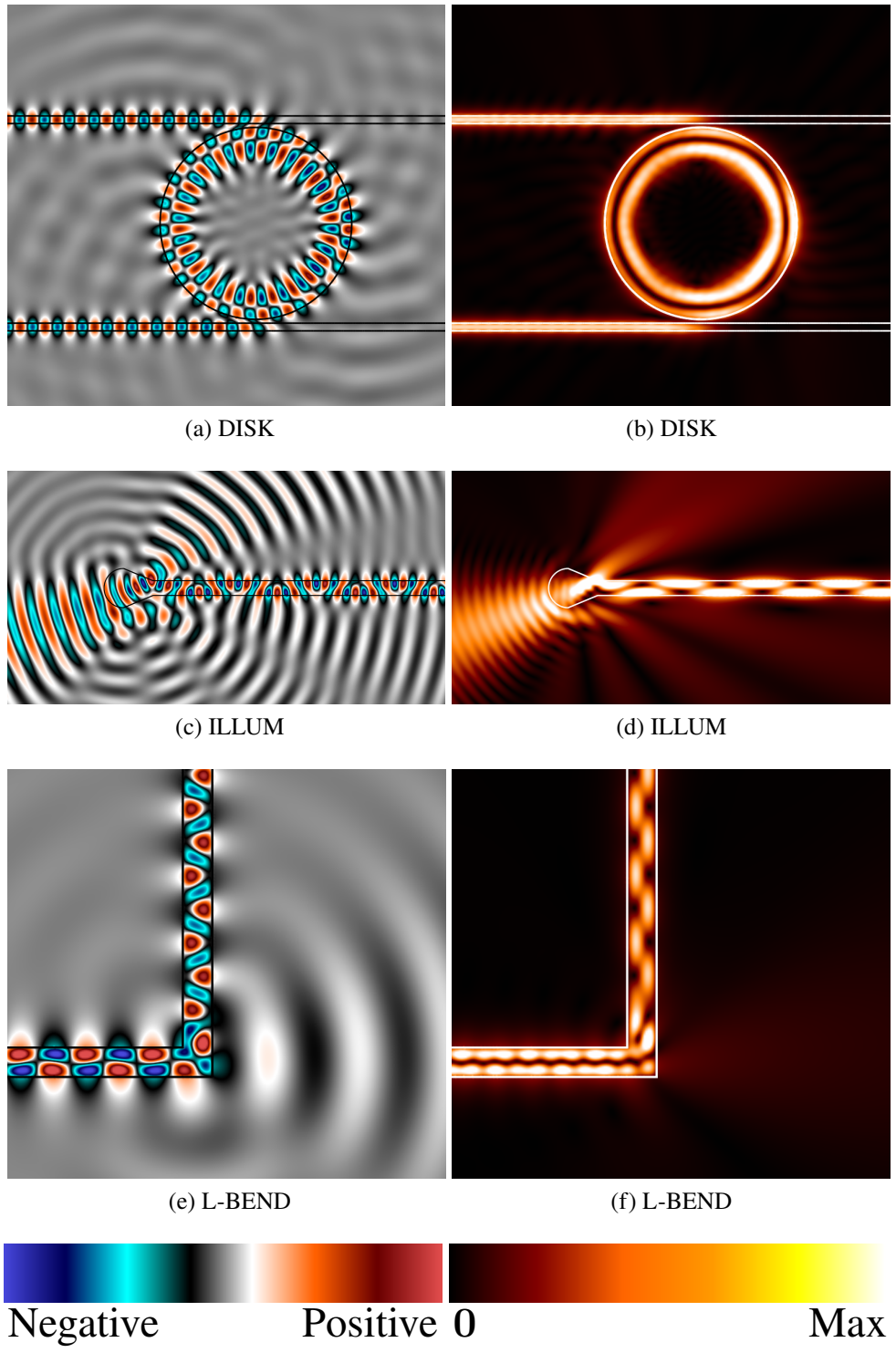

(a) DISK (b) DISK

(c) ILLUM (d) ILLUM

(e) L-BEND (f) L-BEND

(g) Colormap for Re(u) (h) Colormap for $|u|$

Figure 2.4: Real part and absolute value of u_w (left and right columns, respectively) produced by the WGF method for several open-waveguide problems.

- DISK (TE). Circular disk resonator [76, Sec. 16.5] illuminated by the first symmetric mode incoming from the top-left waveguide. The core and cladding wavenumbers in both waveguides are $k_{\text{co}} = 250\pi/127$ and $k_{\text{cl}} = 125\pi/127$, respectively, and the disk wavenumber equals k_{co}. The waveguide half-widths are both $h = 0.2$, the disk has radius 5, and separation between the waveguides and the disk is 0.2. The wavenumbers were selected to excite a near resonance in the circular cavity.

- ILLUM (TE). Excitation of waveguide modes in a terminated waveguide. The structure is illuminated by a beam incoming from the left at an angle $\pi/10$ radians below the horizontal. (A description of the illuminating field is presented below.) The core and cladding wavenumbers are given by $k_{\text{co}} = 2\pi$ and $k_{\text{cl}} = 4\pi/3$ respectively, while the half-width of the waveguide is $h = 0.5$.

- L-BEND (TM). Sharp $L-$bend illuminated by the first antisymmetric mode incoming from the left waveguide. The core and cladding wavenumbers are $k_{\text{co}} = 2\pi$ and $k_{\text{cl}} = 2\pi/3$ respectively, and the waveguide half-width is given by $h = 0.5$.

The labels used here (COUPLER, BRANCH, etc.) correspond to those used in Figure 2.2 and Figure 2.3. The computing times required to achieve an accuracy better than 1.0×10^{-6} are presented in Table 2.2.

The illuminating field used for the configuration ILLUM is given by the angular spectrum representation [37, equation (49)]

$$u^{\text{inc}}(r,\theta) = \int_{-\pi/2}^{\pi/2} F(\alpha) e^{ik_1 r\cos(\theta+\alpha)} \mathrm{d}\alpha, \tag{2.30}$$

with $F(\alpha) = e^{-12.5(\alpha+\pi/10)^2}$. Note that equation (2.18) does not directly apply in this case since the illuminating field used here is not a waveguide mode. But only slight modifications are necessary: the relevant windowed equation in this case is

$$E(\boldsymbol{r})\boldsymbol{\Phi}(\boldsymbol{r}) + T[w_A\boldsymbol{\Phi}](\boldsymbol{r}) = \boldsymbol{\Phi}^{\text{inc}}(\boldsymbol{r}), \quad \boldsymbol{r} \in \Gamma. \tag{2.31}$$

This equation can be solved by a procedure analogous to that presented in section 2.2.4.

Table 2.2: Computing times (in seconds) required by the WGF method to produce the densities $\mathbf{\Phi}^{\text{scat}}$ and to evaluate the fields u_w (on a 128×128 evaluation grid), with an accuracy better than 1.0×10^{-6}, for the various test cases mentioned in the text.

Problem	#-Unknowns	A/λ	Time-$\mathbf{\Phi}^{\text{scat}}$	Time-u_w
FLAT	1752	9	1.06	3.47
COUPLER	6450	12	13.05	9.23
BRANCH	5978	14	13.82	8.13
HORN	2902	15	3.28	7.69
DISK	6556	16	11.62	5.09
ILLUM	1374	15	0.83	3.34
L-BEND	2516	12	2.03	3.80

Chapter 3

MODE FINDER ALGORITHM FOR ELECTROMAGNETIC WAVEGUIDES

In Chapter 2, we described a methodology to model non-uniform two-dimensional electromagnetic waveguides, which approximate finite-sized slab waveguides when the width is much larger compared to the height. However, many applications require three-dimensional waveguides whose cross section has similar dimensions in all directions—hence the two-dimensional approximation does not provide a meaningful result.

The accurate simulation of dielectric waveguide problems presents significant challenges since the fields are not bound to the interior of the waveguide. Furthermore, the boundaries between the dielectric materials extend to infinity. Hence, it's natural to tackle different parts of the waveguide problem in separate ways. For instance, the WGF method from Chapter 2 deals with nonuniform two-dimensional waveguides. Conversely, for the more complex three-dimensional problem, we'll separate it into two problems: (1) find the modes of uniform waveguides with arbitrary transverse shape, and (2) model nonuniform waveguides. The first problem is the subject of this chapter, while the second one is left to Chapter 6—where the WGF method is generalized for the three-dimensional case.

This chapter describes an adaptation of the method presented in [2, 3] to find the bound modes of dielectric waveguides of arbitrary transverse shape. The method in [3] was designed to find eigenpairs of the Zaremba problem using integral equations, together with a modified method to avoid spurious solutions which was introduced in [10]. We show that these ideas can be successfully applied to electromagnetic waveguides by reformulating the mode equations into a set of integral equations with appropriate boundary conditions. In particular, the method can handle arbitrary waveguides with C^2 boundaries, and it can handle modes corresponding to multiple eigenvalues.

3.1 Mode equations

Consider a dielectric material with infinite boundaries along the $z-$axis—which we will take as the optical axis—and a constant, finite shape across any xy-plane

(see Figure 3.1). Let the interior and exterior domains of the structure be denoted as Ω_1, and Ω_2, with respective refractive indices n_1 and n_2, and boundary Γ. In order to have a guiding dielectric structure—i.e. a waveguide—we require $n_1 > n_2$, which ensures that total internal reflection can occur inside the waveguide [46]. In the optics literature, the domain Ω_1 is often referred as the waveguide *core*, while Ω_2 is the waveguide *cladding* [75].

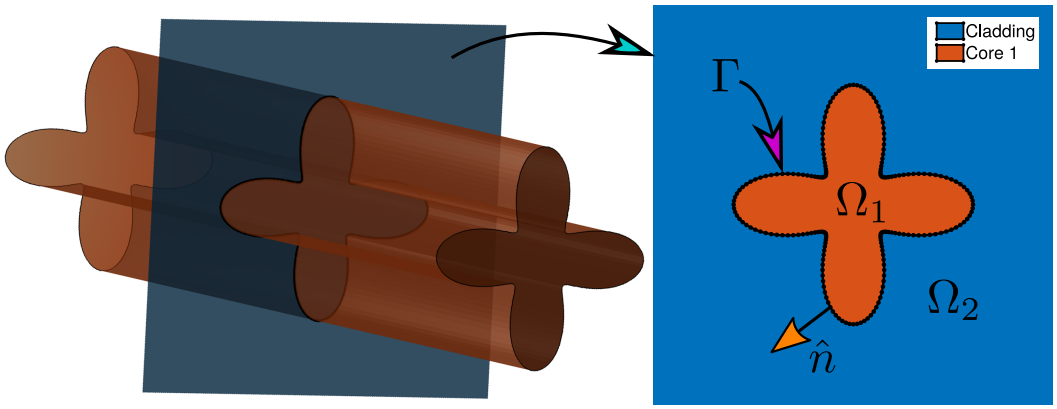

Figure 3.1: Illustration of a uniform dielectric waveguide with arbitrary cross section.

The electromagnetic fields satisfy Maxwell's equations with the relevant boundary conditions at the interface between dielectrics. Throughout a time-harmonic dependence with angular frequency ω is assumed but suppressed (see e.g. section 1.2). Furthermore, since we are looking for guided fields, i.e. fields that do not decay inside the core as they propagate, we can also assume a harmonic factor in the $z-$direction, that is, we have that the total electromagnetic fields $\tilde{\mathbf{E}} = (\tilde{E}_x, \tilde{E}_y, \tilde{E}_z)$, and $\tilde{\mathbf{H}} = (\tilde{H}_x, \tilde{H}_y, \tilde{H}_z)$ are given by the ansatz

$$\tilde{\mathbf{E}}(x, y, z, t) = \mathbf{E}(x, y) \exp(ik_z z - i\omega t), \tag{3.1a}$$

$$\tilde{\mathbf{H}}(x, y, z, t) = \mathbf{H}(x, y) \exp(ik_z z - i\omega t), \tag{3.1b}$$

where k_z denotes the propagation constant.

It is important to note that not all solutions to Maxwell's equations for this problem can be written in the form of equation (3.1). In fact, those that do satisfy equation (3.1) for some propagation constant, together with the appropriate boundary conditions and the Silver-Müller radiation condition [63], are known as the *bound modes* (or *guiding modes*) of the waveguide [75]. The bound modes enjoy the unique property of concentrating all the energy to a vicinity of the waveguide

core—a bound mode propagating in a waveguide has zero loss, independently of the propagation distance.

To find the bound modes, we need to identify the values of k_z and modal fields **E**, **H** so that equation (3.1) satisfy Maxwell's equations with the right boundary and radiation conditions. Using the ansatz equation (3.1), and defining the transverse wavenumbers

$$\gamma_i(k_z) \equiv \sqrt{n_i^2 \frac{\omega^2}{c^2} - k_z^2} \quad \text{for i = 1, 2 ,} \tag{3.2}$$

we have that Maxwell's equations reduce to a set of PDEs for the longitudinal (with respect to the optical axis) components of the fields [46][1]

$$\left.\begin{aligned} \Delta H_z + \gamma_i^2 H_z = 0 \\ \Delta E_z + \gamma_i^2 E_z = 0 \end{aligned}\right\} \text{in } \Omega_i\,, \quad \text{for i = 1, 2 ,} \tag{3.3}$$

coupled by the boundary conditions

$$E_z^+ - E_z^- = 0\,, \quad \text{on } \Gamma, \tag{3.4a}$$

$$H_z^+ - H_z^- = 0\,, \quad \text{on } \Gamma, \tag{3.4b}$$

$$\frac{\varepsilon_1}{\gamma_1^2}\frac{\partial E_z^-}{\partial \boldsymbol{n}} - \frac{\varepsilon_2}{\gamma_2^2}\frac{\partial E_z^+}{\partial \boldsymbol{n}} + \frac{\omega\mu_0}{k_z}\left(\frac{\varepsilon_1}{\gamma_1^2} - \frac{\varepsilon_2}{\gamma_2^2}\right)\frac{\partial H_z}{\partial T} = 0\,, \quad \text{on } \Gamma, \tag{3.4c}$$

$$\frac{1}{\gamma_1^2}\frac{\partial H_z^-}{\partial \boldsymbol{n}} - \frac{1}{\gamma_2^2}\frac{\partial H_z^+}{\partial \boldsymbol{n}} + \frac{\omega}{k_z}\left(\frac{\varepsilon_2}{\gamma_2^2} - \frac{\varepsilon_1}{\gamma_1^2}\right)\frac{\partial E_z}{\partial T} = 0\,, \quad \text{on } \Gamma, \tag{3.4d}$$

where $\boldsymbol{n}$ denotes the outward normal vector, T is the tangential vector in counter-clockwise direction, and the fields at the boundaries are defined by

$$E_z^\pm \equiv \lim_{\delta\to 0} E_z(\boldsymbol{r} \pm \delta\boldsymbol{n})\,, \tag{3.5a}$$

$$H_z^\pm \equiv \lim_{\delta\to 0} H_z(\boldsymbol{r} \pm \delta\boldsymbol{n})\,. \tag{3.5b}$$

Once the longitudinal components of the field are found, the transverse components can be computed from the relation

$$(E_x, E_y) = \frac{i}{\gamma^2}\left(k_z \nabla E_z - \omega\mu_0 \hat{z} \times \nabla H_z\right), \tag{3.6a}$$

$$(H_x, H_y) = \frac{i}{\gamma^2}\left(k_z \nabla H_z + \omega\varepsilon_0 n^2 \hat{z} \times \nabla E_z\right), \tag{3.6b}$$

[1] The differential operators used are to be understood depending on the dimension of the field for which they act on. For example, Δu is the Laplacian in $\mathbb{R}^n$ if u is an n-dimensional field.

with

$$\gamma(\boldsymbol{r}) = \gamma_i, \quad \boldsymbol{r} \in \Omega_i\,, \tag{3.7a}$$

$$n(\boldsymbol{r}) = n_i, \quad \boldsymbol{r} \in \Omega_i\,. \tag{3.7b}$$

In order for the modal fields to be purely propagating modes, the propagation constant needs to be within the bounds $n_2\omega/c < k_z < n_1\omega/c$—a condition that ensures that total internal reflection can take place [75], or, mathematically, that γ_1 is purely real, while at the same time γ_2 is purely imaginary. This results in equation (3.3) being the Helmholtz equation for Ω_1, and the modified Helmholtz equation [8] for Ω_2, for which the fundamental solution decays exponentially, and thus ensures that all of the energy of the electromagnetic fields is restricted to a neighborhood of the waveguide core.

3.2 Bound modes of a circular waveguide

One extremely important case, for both theoretical and applied settings, is that of a circular waveguide, which provides a practical model to optical fibers used in telecommunications. Another key point on why this problem is of great consequence, is that a solution can be found using the method of separation of variables—consequently the fields can be expressed in terms of special functions.

Inside the core of the waveguide Ω_1, the longitudinal fields satisfy the Helmholtz equation, and enforcing the fields to be finite at the center of the core, the solution is then given in terms of the Bessel function of the first kind. For the cladding region Ω_2, and imposing the fields to be bounded at infinity, results in the solution being in terms of the modified Bessel function of the second kind—alternatively, in terms of the Hankel function with imaginary argument [1, Eq. 9.6.4]. Using the cylindrical coordinate system $r = \sqrt{x^2 + y^2}$, $\theta = \arctan(y/x)$, a bound mode for a circular waveguide of radius one is given by [46, 75]

$$\begin{bmatrix} E_z, & H_z \end{bmatrix}^T = \begin{cases} \begin{bmatrix} A_1, & B_1 \end{bmatrix}^T J_m(|\gamma_1|r)\ \exp(im\theta), & r \le 1 \\ \begin{bmatrix} A_2, & B_2 \end{bmatrix}^T H_m^{(1)}(i|\gamma_2|r)\ \exp(im\theta), & r > 1 \end{cases}, \tag{3.8}$$

for an integer m and constants A_1, A_2, B_1, B_2 so that the boundary conditions in equation (3.4) are satisfied. However, a solution exists only for certain combinations of k_z and m. In order to find the admissible values of these parameters, we can formulate the problem as finding the values of k_z and m for which a certain 4×4 matrix $A_m(k_z)$, derived in what follows, has a non-trivial null space.

In order to obtain the matrix $A_m(k_z)$, we apply the boundary conditions equation (3.4) to the separation-of-variables solution equation (3.8), and using the shorthand notations

$$J_m \equiv J_m(\gamma_1), \tag{3.9a}$$

$$H_m \equiv H_m^{(1)}(\gamma_2), \tag{3.9b}$$

$$\Delta J_m \equiv J_{m-1} - J_{m+1}, \tag{3.9c}$$

$$\Delta H_m \equiv H_{m-1} - H_{m+1}, \tag{3.9d}$$

we obtain

$$A_m(k_z) \equiv \begin{bmatrix} J_m & -H_m & 0 & 0 \\ 0 & 0 & J_m & -H_m \\ \frac{\varepsilon_1}{2\gamma_1}\Delta J_m & -\frac{\varepsilon_2}{2\gamma_2}\Delta H_m & \frac{im\omega\mu_0}{k_z}\left(\frac{\varepsilon_1}{\gamma_1^2} - \frac{\varepsilon_2}{\gamma_2^2}\right) J_m & 0 \\ \frac{im\omega}{k_z}\left(\frac{\varepsilon_2}{\gamma_2^2} - \frac{\varepsilon_1}{\gamma_1^2}\right) J_m & 0 & \frac{1}{2\gamma_1}\Delta J_m & -\frac{1}{2\gamma_2}\Delta H_m \end{bmatrix}, \tag{3.10}$$

which, in order to have a waveguide mode, must satisfy the condition

$$A_m(k_z)\begin{bmatrix} A_1, & A_2, & B_1, & B_2 \end{bmatrix}^T = 0 \tag{3.11}$$

for a non-trivial vector $[A_1, A_2, B_1, B_2]^T$.

Then, to find the modes of the circular waveguide, one has to find the values of m and k_z for which A_m in equation (3.10) has non-trivial null space. This can be done by performing a root search on the minimum singular value of A_m as a function of k_z—the corresponding right-singular vectors can be used to find the values of A_1, A_2, B_1 and B_2 that can be used to compute the longitudinal fields of the mode using equation (3.8).

The specific implementation of the mode-finding algorithm used for the circular case is shown in Algorithm 3.1, and in fact, it serves as a simplified case of the mode-finding algorithm that is shown in section 3.4. The method is a variation of the methodology presented in [3].

Algorithm 3.1 Mode finder algorithm for a circular waveguide

Set $m_{\max}$: Maximum number of integer angular frequencies m
Set Δk_z: Resolution for $\sigma_{\min}$ sampling
Set tol_σ: Tolerance for zero singular value
$N_{kz} = \lfloor (k_2 - k_1)/(\Delta k_z) \rfloor$
$c = 0$: Mode counter
for $m = 0, 1, \ldots, m_{\max}$ **do** $\rightarrow$ Angular frequencies
    for $\ell = 1, 2, \ldots, N_{kz} - 1$ **do** $\rightarrow$ Initial $\sigma_{\min}$ sampling
        $k_z^\ell = k_2 + \ell \Delta k_z$,
        $s_\ell = \sigma_{\min}(A_m(k_z^\ell))$
    end for
    for $\ell = 2, 3, \ldots, N_{kz} - 2$ **do** $\rightarrow$ Estimate intervals for the minima
        if $s_\ell \leq s_{\ell+1}$ & $s_\ell \leq s_{\ell-1}$ **then**
            $(k_z^{\min}, s_{\min})$ = Golden-section search with interval $[k_z^{\ell-1}, k_z^{\ell+1}]$
            if $s_{\min} < \text{tol}_\sigma$ **then**
                $c = c + 1$
                $k_z^{\text{mode}}(c) = k_z^{\min}$
                $m^{\text{mode}}(c) = m$
            end if
        end if
    end for
end for
return $k_z^{\text{mode}}, m^{\text{mode}}$

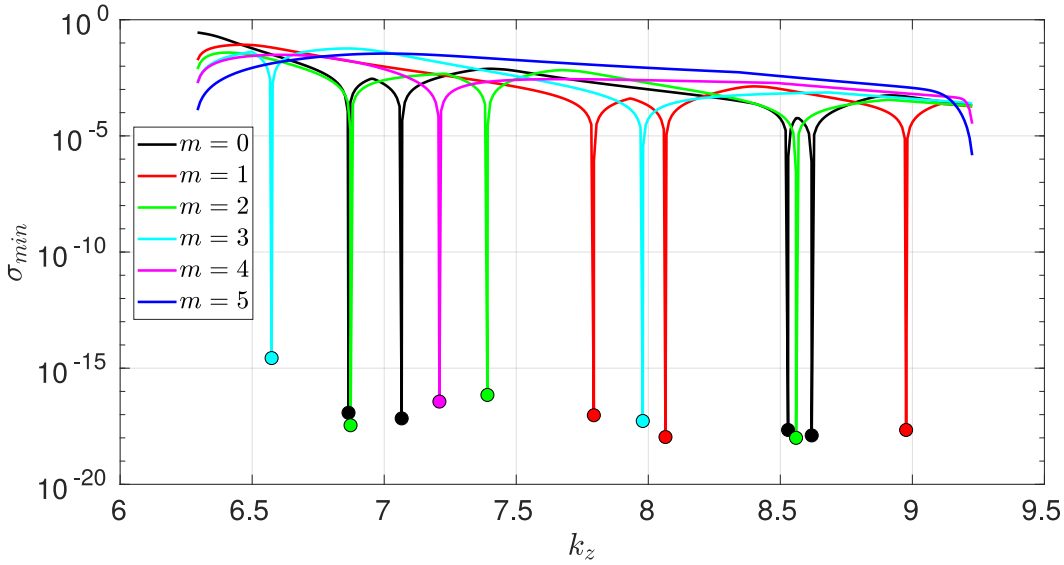

Figure 3.2: Minimum singular value as a function of the propagation constant obtained using Algorithm 3.1. The parameters for this circular waveguide of radius equal one are $n_{\text{co}} = 1.47$, $n_{\text{cl}} = 1.00$, $\lambda_0 = 1.0$.

3.3 Integral equation formulation

We now turn our attention to the more general case of a step-index waveguide with an arbitrary C^2 curve as the boundary at any given cross section. In this section, we use integral equations to reformulate the problem, finding a system analogous to that in equation (3.10) for which a mode search algorithm —such as that in [3]—can be applied.

The integral representation used here is based on a combined field that results in only weakly-singular kernels—allowing us to use standard techniques for the numerical computation of integral equations such as those described in [32, Ch. 3].

Given that E_z and H_z satisfy the Helmholtz equation (3.3), these fields can be expressed in terms of the single- and double-layer potential [32]:

$$E_z(\boldsymbol{r}) = \begin{cases} \mathscr{S}_1[\mu^E](\boldsymbol{r}) + (C^E)^{-1}\mathscr{D}_1[\eta^E](\boldsymbol{r}), & \boldsymbol{r} \in \Omega_1 \\ \mathscr{S}_2[\mu^E](\boldsymbol{r}) + \mathscr{D}_2[\eta^E](\boldsymbol{r}), & \boldsymbol{r} \in \Omega_2 \end{cases} \tag{3.12a}$$

$$H_z(\boldsymbol{r}) = \begin{cases} \mathscr{S}_1[\mu^H](\boldsymbol{r}) + (C^H)^{-1}\mathscr{D}_1[\eta^H](\boldsymbol{r}), & \boldsymbol{r} \in \Omega_1 \\ \mathscr{S}_2[\mu^H](\boldsymbol{r}) + \mathscr{D}_2[\eta^H](\boldsymbol{r}), & \boldsymbol{r} \in \Omega_2 \end{cases} \tag{3.12b}$$

where the k_z-dependent quantities

$$C^E(k_z) \equiv \left(\frac{\gamma_2(k_z)}{\gamma_1(k_z)}\right)^2 \frac{\varepsilon_1}{\varepsilon_2}, \tag{3.13a}$$

$$C^H(k_z) \equiv \left(\frac{\gamma_2(k_z)}{\gamma_1(k_z)}\right)^2, \tag{3.13b}$$

are chosen so that the system of integral equations involves only weakly singular kernels. (We'll drop the explicit dependence on k_z, but it is worth keeping in mind that $\gamma_{1,2}$ are functions of this variable.)

Define the values

$$F^E \equiv \frac{\gamma_2^2 \omega \mu_0}{\varepsilon_2 k_z}\left(\frac{\varepsilon_1}{\gamma_1^2} - \frac{\varepsilon_2}{\gamma_2^2}\right), \tag{3.14a}$$

$$F^H \equiv \frac{\gamma_2^2 \omega}{k_z}\left(\frac{\varepsilon_2}{\gamma_2^2} - \frac{\varepsilon_1}{\gamma_1^2}\right), \tag{3.14b}$$

and the vector density

$$\varphi \equiv \begin{bmatrix} \eta^E & \eta^H & \mu^E & \mu^H \end{bmatrix}^T, \tag{3.15}$$

and the operator matrices

$$\widetilde{I} \equiv \begin{bmatrix} \frac{1}{2}\left(1+\frac{1}{C^E}\right) I & 0 & 0 & 0 \\ 0 & \frac{1}{2}\left(1+\frac{1}{C^H}\right) I & 0 & 0 \\ 0 & 0 & -\frac{1}{2}\left(1+C^E\right) I & 0 \\ 0 & 0 & 0 & -\frac{1}{2}\left(1+C^H\right) I \end{bmatrix}, \tag{3.16a}$$

$$M \equiv \begin{bmatrix} D_2 - \frac{1}{C^E} D_1 & 0 & S_2 - S_1 & 0 \\ 0 & D_2 - \frac{1}{C^H} D_1 & 0 & S_2 - S_1 \\ N_2 - N_1 & -\frac{F^E}{C^H} T\left(-\frac{1}{2} I + D_1\right) & K_2 - C^E K_1 & -F^E T S_1 \\ -\frac{F^H}{C^E} T\left(-\frac{1}{2} I + D_1\right) & N_2 - N_1 & -F^H T S_1 & K_2 - C^H K_1 \end{bmatrix}, \tag{3.16b}$$

$$\widetilde{A}(k_z) \equiv \widetilde{I} + M. \tag{3.16c}$$

Then, using the jump conditions [32, Theorem 3.1] together with the boundary conditions in equation (3.4) we obtain that for a bound mode, the following integral equations must be satisfied

$$\widetilde{A}\varphi = 0. \tag{3.17}$$

We will denote as A_B—for boundary—the discrete version of $\widetilde{A}$.

3.4 Mode-finding algorithm

A first approach to find the modes of a waveguide on the basis of the integral representation of the previous section could be attempted via an algorithm similar to the one we used for the circular case (Algorithm 3.1), but instead of taking the minimum singular value of equation (3.10), one would take the minimum singular value of A_B. Unfortunately, doing so introduces some *spurious* modes that are not true bound modes. These spurious solutions are a consequence of the Riemann-Lebesgue lemma (see [3, Remark 6.3]), which, roughly speaking, implies that highly-oscillatory densities can produce small integral values. In [10], a method to avoid spurious solutions of a similar kind was introduced for the method of particular solutions, and in [3] the same idea was successfully implemented to regularize the σ_{min} curve in the context of the integral-equation formulation of the Zaremba eigenvalue problem. We will show that for the problem considered in this chapter, the aforementioned modified method provides an effective tool to bypass the undesired spurious modes in the root finding search.

The modified method laid out by [10, section 5] is based on extending the matrix A by a set of rows on which the fields are evaluated. In the context of our problem, we have

$$A(k_z) = \begin{bmatrix} A_B(k_z) \\ A_I(k_z) \end{bmatrix} \tag{3.18}$$

where A_I is a rectangular matrix that evaluates E_z and H_z in a set of interior (of the core's waveguide) points[2]. Then, the QR factorization of A has the form

$$Q(k_z) = \begin{bmatrix} Q_B(k_z) \\ Q_I(k_z) \end{bmatrix}. \tag{3.19}$$

By performing a root-finding search on the smallest singular value of Q_B, one can ensure that the resulting densities of the mode produce fields that have close to unit norm on the sampled interior values of the fields, thus avoiding the spurious solutions that are characterized by high-oscillations at the boundary, but close to zero field values away from it.

Algorithm 3.2 Integral-equation mode finder algorithm for waveguides with arbitrary cross section.

Set Δk_z: Resolution for $\sigma_{\min}$ sampling
Set tol_σ: Tolerance for zero singular value
$N_{kz} = \lfloor (k_2 - k_1)/(\Delta k_z) \rfloor$
$c = 0$: Mode counter
for $\ell = 1, 2, ..., N_{kz} - 1$ **do** → Initial $\sigma_{\min}$ sampling
    $k_z^\ell = k_2 + \ell \Delta k_z$,
    $s_\ell = \sigma_{\min}(Q_B(k_z^\ell))$ → Equation (3.19)
end for
for $\ell = 2, 3, ..., N_{kz} - 2$ **do** → Estimate intervals for the minima
    if $s_\ell \leq s_{\ell+1}$ & $s_\ell \leq s_{\ell-1}$ **then**
        $(k_z^{\min}, s_{\min})$ = Golden-section search with interval $[k_z^{\ell-1}, k_z^{\ell+1}]$
        if $s_{\min} < \text{tol}_\sigma$ **then**
            $c = c + 1$
            $k_z^{\text{mode}}(c) = k_z^{\min}$
        end if
    end if
end for
return k_z^{mode}

[2]The underscores B and I refer respectively to "boundary" and "interior."

3.5 Numerical examples

This section presents some numerical examples that demonstrate the effectiveness of the integral-equation mode finder algorithm for open waveguides described in section 3.4 and summarized in Algorithm 3.2.

3.5.1 Circular waveguide

In our first example, we consider the circular waveguide problem, whose exact solution—derived in section 3.5.1—is used for reference. Figure 3.3 displays the smallest singular values for the modified and the unmodified method (in solid black and red respectively), together with the k_z values found by the separation of variables method—presented in the colored vertical dashed lines. We can see that the modified method successfully removes the spurious solutions, and at the same time smoothens out the σ_{min} curve, which consequently improves the performance of the root-finding algorithm. Additionally, Figure 3.4 presents the convergence of the propagation constants for each one of the modes considered. In particular, the figure demonstrates the exponential rate of convergence provided by the integral solver for the propagation constant k_z.

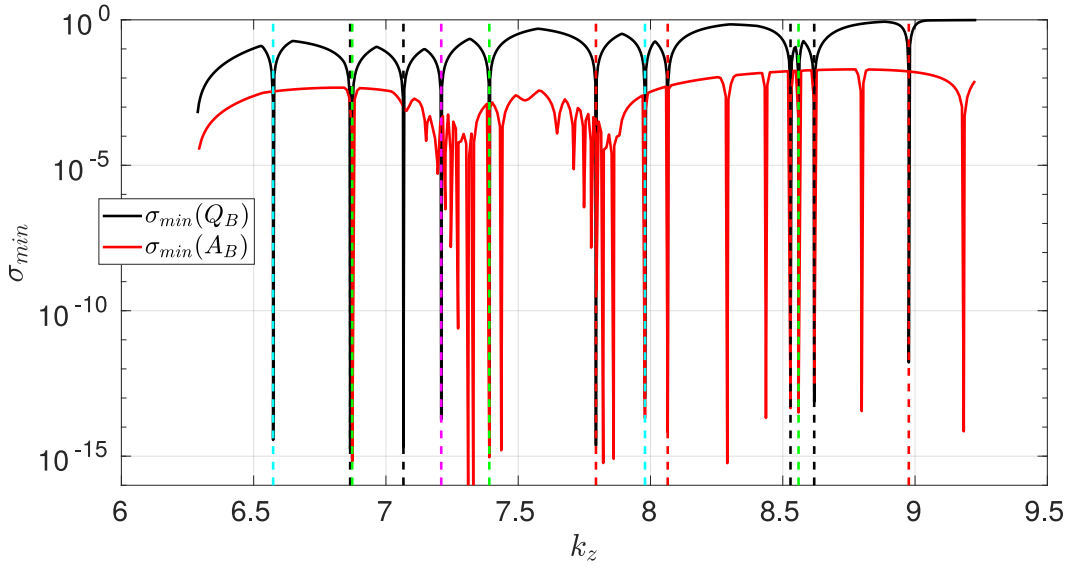

Figure 3.3: Comparison between the direct and modified mode search methods. The solid black shows the minimum singular value for the matrix Q_B in equation (3.19), which provides a modified method that gets rid of the spurious solutions. On the other hand, the solid red line is the minimum singular value for A_B, the discretized version from equation (3.16c). The dashed lines represent the values obtained from the mode search using the analytical expressions. In this case, the parameters are $n_{\text{co}} = 1.47$, $n_{\text{cl}} = 1.00$, $\lambda_0 = 1.0$.

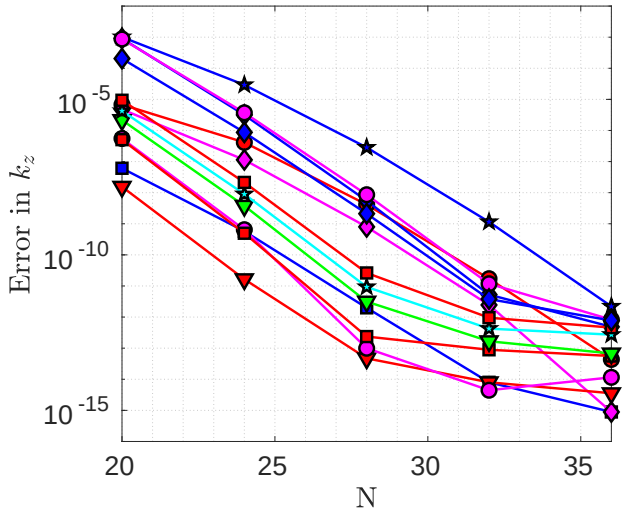

Figure 3.4: Convergence in the 13 different propagation constants for the case of a circular waveguide. In this case, the waveguide parameters are $n_{\text{co}} = 1.47$, $n_{\text{cl}} = 1.00$, $\lambda_0 = 1.0$.

3.5.2 Flower waveguide

In our second example, we consider a waveguide whose cross section is a four-petal "flower." The shape of this boundary, which includes some symmetries as well as sharp curvatures at the edges between petals, makes it an interesting case study. Figure 3.6 presents the results for the mode search and the $z-$fields for two corresponding modes. We see that the σ_{min} curve behaves similarly to that of the circular waveguide, while the field values associated with the various modes reflect the geometrical symmetry. The electromagnetic parameters used for this simulation are $n_{\text{co}} = 1.47$, $n_{\text{cl}} = 1.00$, $\lambda_0 = 2.0$.

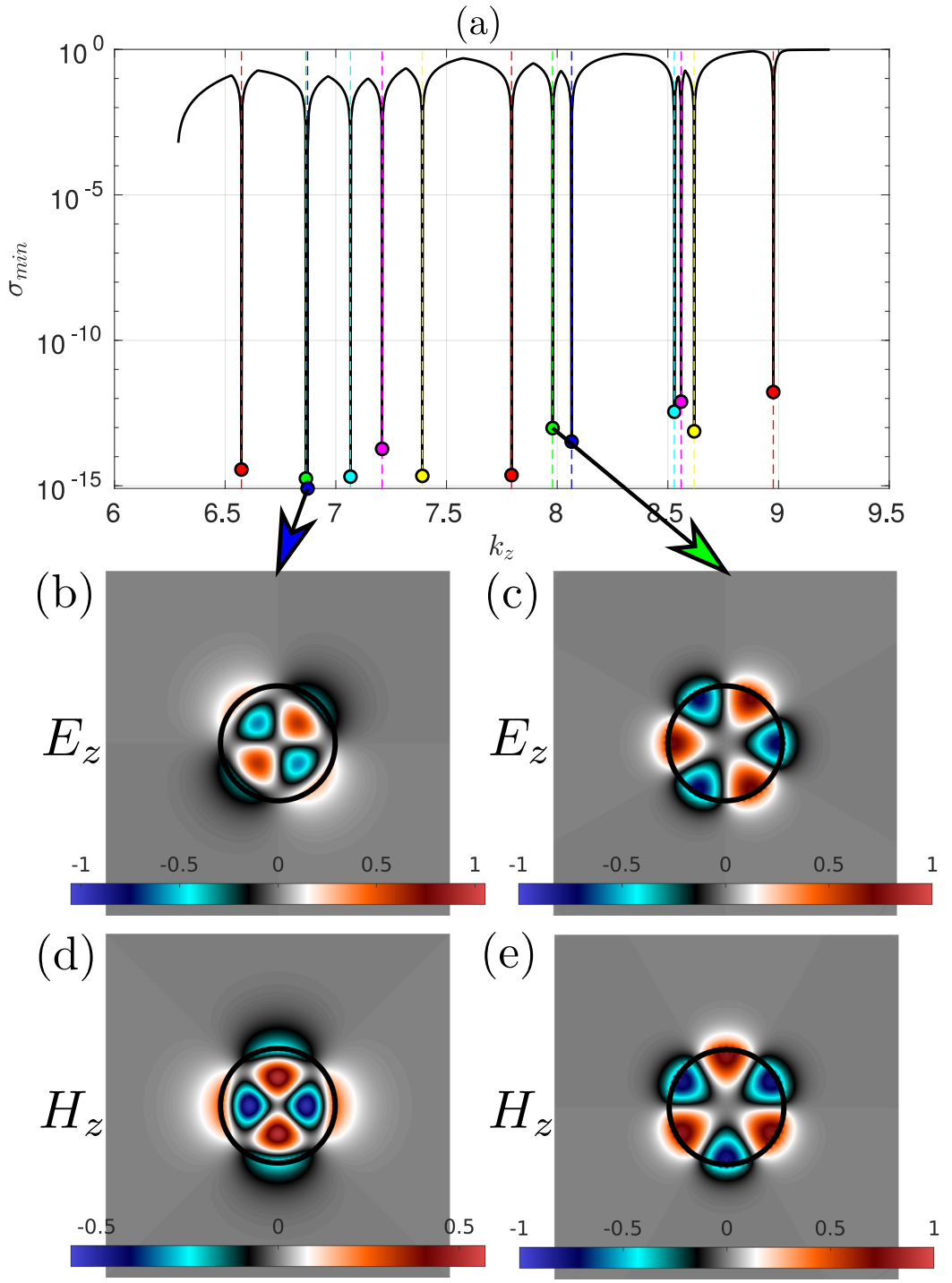

Figure 3.5: Results of the integral-equation mode search algorithm applied to a circular waveguide of radius equal one. In this case, we used a total number of 60 boundary points, and the parameters $n_{\mathrm{co}} = 1.47$, $n_{\mathrm{cl}} = 1.00$, $\lambda_0 = 1.0$ were used.

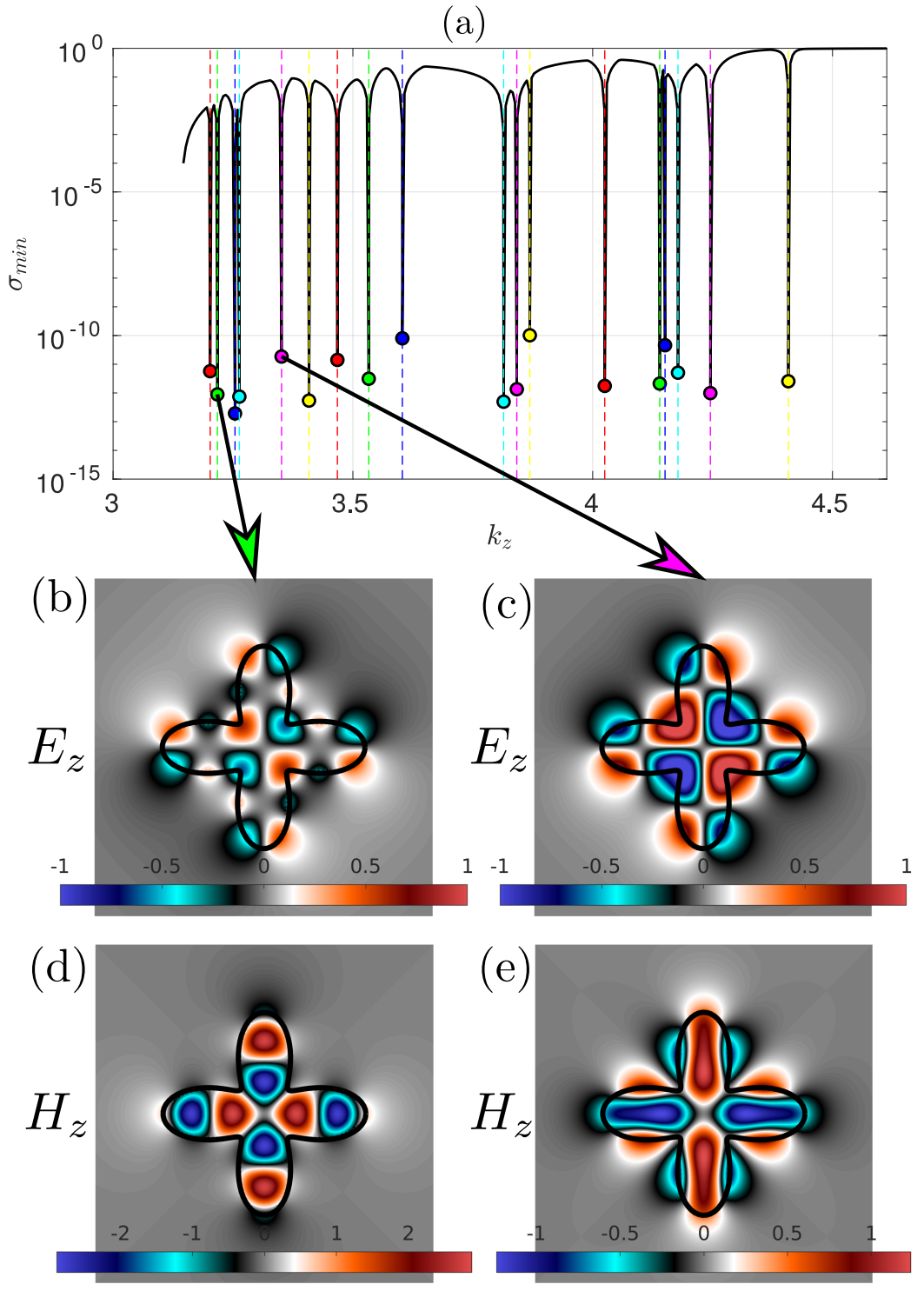

Figure 3.6: Results of the mode search algorithm using a total number of 200 boundary points, and with parameters $n_{\text{co}} = 1.47$, $n_{\text{cl}} = 1.00$, $\lambda_0 = 2.0$. The values of σ_{min} as a function of the propagation constant k_z are shown in (a), E_z and H_z for the second mode are displayed in (b) and (d), while (c) and (e) show also the E_z and H_z fields for the fifth mode found.

3.5.3 Multiple core waveguide

For the purpose of demonstrating the versatility of the method we presented in this chapter, the last example is that of a waveguide consisting of two separate cores. The two cores considered here have the shapes of a four-petal "flower" and a "kite" shape. Figure 3.7 displays the geometry, as well as the interior points we selected for this case—which were arbitrarily chosen to lie on spiral curves near the centers of the cores. Having multiple waveguide cores located near each other provides an interesting case given that the modal solutions are not just the modes of each waveguide, but rather solutions that include perturbations caused by coupling effects. In fact, this is the well-known phenomenon in fiber optics known as *crosstalk*. The results of applying Algorithm 3.2 to this problem are presented in Figure 3.8 which clearly demonstrates the aforementioned coupling effects.

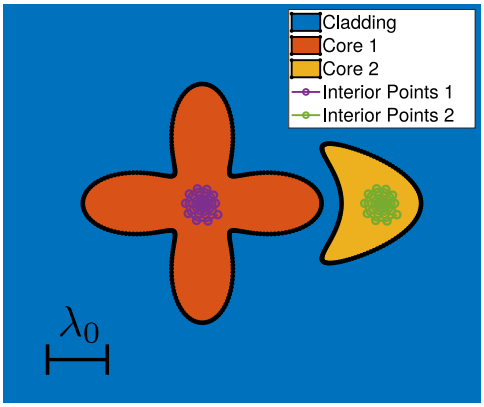

Figure 3.7: Illustration of the two-core example. For this case, we used a set of interior points—for the modified algorithm—along spiral curves in the interiors of both cores.

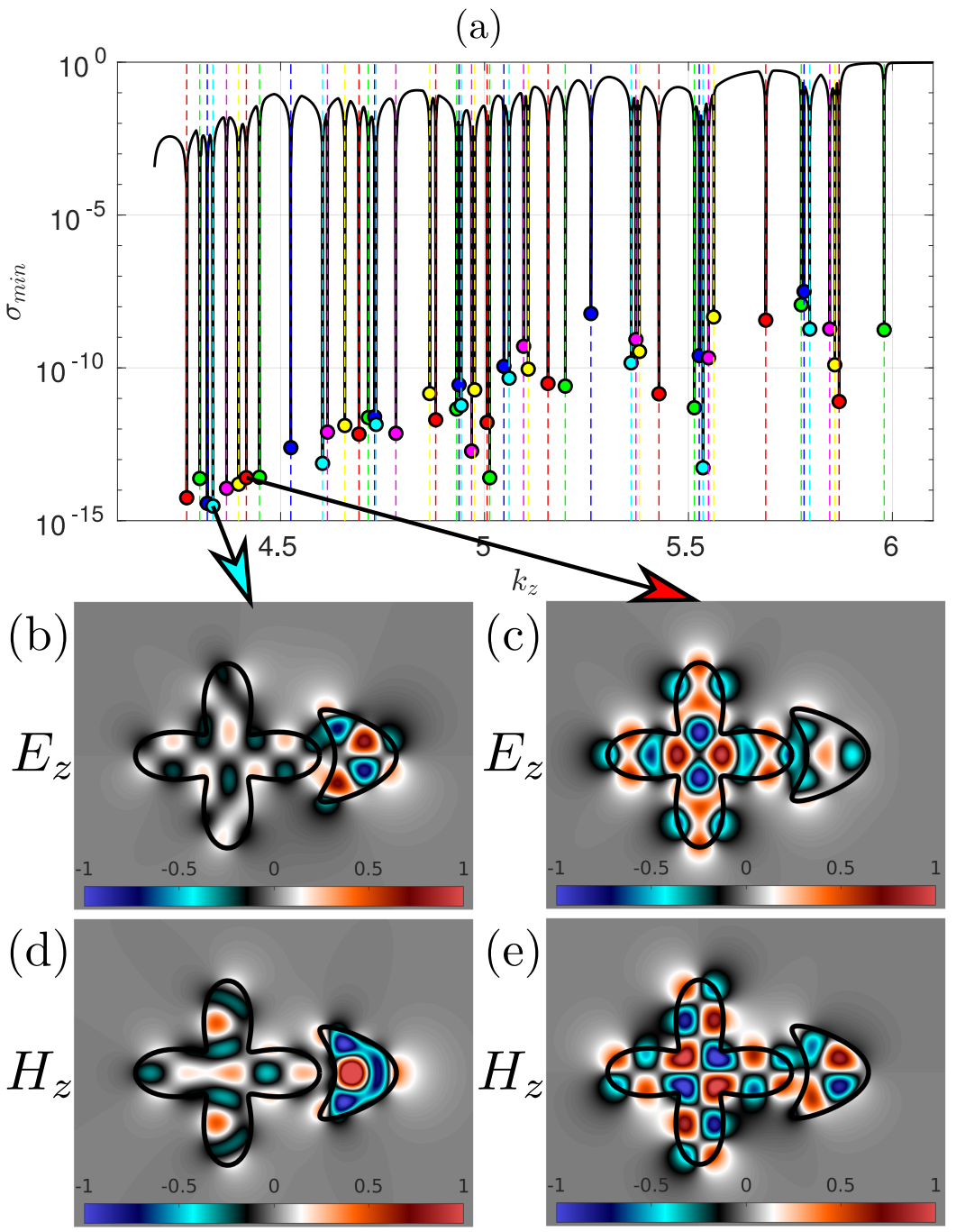

Figure 3.8: In (a), the σ_{min} curve is shown for the two-core waveguide from Figure 3.7. The E_z and H_z fields for the fourth mode found are shown in (b) and (d) respectively, while (c) and (e) depict the E_z and H_z fields (respectively) of the seventh mode. The parameters $n_{\text{co}} = 1.47$, $n_{\text{cl}} = 1.00$, $\lambda_0 = 1.5$ were used.

Three-dimensional problems

Chapter 4

RECTANGULAR-POLAR METHOD FOR SINGULAR INTEGRAL OPERATORS

The solution of scattering problems by means of boundary integral representations has proven to be a game-changer when the ratio of volume to surface scattering is large, where volumetric solvers become intractable due to memory requirements and computational cost. At the heart of every boundary integral equation (BIE) solver lies an integration strategy that must be able to handle the weakly singular integrals associated with the integral formulations of e.g. acoustic and electromagnetic scattering. Several approaches have been proposed to deal with this difficulty, most notably those put forward in [12, 15, 40, 50, 69, 70].

For the problem of scattering by two-dimensional surfaces in three-dimensional space, which reduces to two-dimensional weakly-singular integral equations over the scatterer's surface, there is no simple high-order quadrature rule of the type put forth in [32, 52, 58] for evaluation of weakly-singular operators associated with curves in two-dimensional space. This makes the three-dimensional problem considerably more difficult than its two dimensional counterpart. Therefore, a number of approaches have been proposed—including, notably, Nyström, collocation and Galerkin methodologies—for the evaluation of integral operators over two-dimensional surfaces. Nyström methods use a quadrature rule to evaluate integrals from a point-mesh discretization, with testing on the set of integration points; the collocation approach finds a solution on a finite-dimensional space which satisfies the continuous BIE at a set of collocation points; the Galerkin approach solves the BIE in a discrete weak form, using finite-element spaces for both solution representation and testing.

In this contribution, a Nyström method is presented in which, as in [78], the far interactions are computed via Fejér's first quadrature rule, which yields spectrally accurate results for smooth integrands. On the other hand, the integrals involving singular and near-singular kernels are obtained by relying on highly-accurate precomputed integrals (which are produced by means of rectangular-polar changes of variables that vary with the observation point) of the kernels times Chebyshev polynomials, together with Chebyshev expansions of the densities. The derivatives

of the rectangular-polar change of variables vanish at the kernel-singularity and geometric-singularity points, producing respectively "floating" and fixed clustering around those points, and thus giving rise to high-order accuracy. The floating changes of variables are analogous to those in the polar integration method [15], but differ in the fact that it is applied on a rectangular mesh, hence the "rectangular-polar" terminology we use. The *sinh* transform [47, 48] was also tested as an alternative to the change of variables we eventually selected: the latter method was preferred as the *sinh* change of variables does not appear to allow sufficient control on the distribution of discretization points along the integration mesh, which is needed in order to accurately resolve the wavelength without use of an excessively fine discretization mesh near singularities.

The proposed rectangular-polar approach, which yields high-order accuracy, leads to several additional desirable properties. The proposed use of Chebyshev representations for the density, for example, allows for the evaluation of differential geometry quantities needed for electromagnetic BIE by means differentiation of corresponding Chebyshev series. Additionally, the nodes for Fejér's first quadrature are the same as the nodes for the discrete orthogonality property of Chebyshev polynomials, which make the computation of the Chebyshev transforms straightforward. In addition to scattering by a bounded obstacle, this integral equation solver can also be used in the context of the Windowed Green function method for scattering by unbounded obstacles such as layered media [18, 20, 68] and waveguides [22].

This chapter is organized as follows. After basic preliminaries are put forth in section 4.1, the proposed surface representation structure is described in section 4.2. The overall rectangular-polar integration strategy, including details concerning the methodologies used to produce integrals for smooth, singular and near-singular kernels as well as edge-singular integral densities, is presented in section 4.3. A variety of numerical results for open and closed scattering surfaces are then presented in section 4.4, emphasizing the convergence properties of both the forward map (which evaluates the action of the integral operator for a given density) as well as the full scattering solver, and demonstrating the accuracy, generality, and speed of the proposed approach. Results of an application to a problem of scattering by a geometry generated by CAD software is also presented in that section, demonstrating the applicability of the proposed method to complex geometrical designs in science and engineering.

4.1 Preliminaries

For conciseness, we consider the problem of acoustic scattering by a sound-soft obstacle, though the methodology proposed is also applicable to electromagnetic scattering and other integral-equation problems involving singular kernels.

Let Ω denote the complement of an obstacle D in three-dimensional space, let Γ denote the boundary of the obstacle, and call U^{inc}, U^{scat} and $U = U^{\text{scat}} + U^{\text{inc}}$ the incident, scattered and total fields, respectively. Then, the total field $U = U^{\text{scat}} + U^{\text{inc}}$ satisfies the Helmholtz equation

$$\Delta U(\boldsymbol{r}) + k^2 U(\boldsymbol{r}) = 0, \quad \boldsymbol{r} \in \mathbb{R}^3 \setminus \overline{\Gamma}, \tag{4.1}$$

with wavenumber $k = 2\pi/\lambda$, and the scattered field U^{scat} satisfies the Sommerfeld radiation condition as well as the boundary condition

$$U^{\text{scat}}(\boldsymbol{r}) = -U^{\text{inc}}(\boldsymbol{r}), \quad \boldsymbol{r} \in \Gamma. \tag{4.2}$$

As is well known [32], the scattered field can be represented in terms of layer potentials—which reduce the scattering problem to a boundary integral equation that contains singular kernels. The single- and double-layer potentials are defined by

$$\mathscr{S}[\,\widetilde{\varphi}\,](\boldsymbol{r}) = \int_\Gamma G(\boldsymbol{r}, \boldsymbol{r}')\, \widetilde{\varphi}(\boldsymbol{r}')\, \mathrm{d}\sigma(\boldsymbol{r}'), \quad \boldsymbol{r} \in \mathbb{R}^3 \setminus \overline{\Gamma}, \tag{4.3}$$

$$\mathscr{D}[\,\widetilde{\varphi}\,](\boldsymbol{r}) = \int_\Gamma \frac{\partial G(\boldsymbol{r}, \boldsymbol{r}')}{\partial \boldsymbol{n}(\boldsymbol{r}')}\, \widetilde{\varphi}(\boldsymbol{r}')\, \mathrm{d}\sigma(\boldsymbol{r}'), \quad \boldsymbol{r} \in \mathbb{R}^3 \setminus \overline{\Gamma}, \tag{4.4}$$

respectively, where $G(\boldsymbol{r}, \boldsymbol{r}') = \exp(ik|\boldsymbol{r} - \boldsymbol{r}'|)/4\pi|\boldsymbol{r} - \boldsymbol{r}'|$ is the free-space Green function of the Helmholtz equation, $\boldsymbol{n}$ is the outward-pointing normal vector, and $\widetilde{\varphi}$ is the surface density.

In this chapter, we demonstrate the proposed methodology through applications to two main scattering problems under a unified scheme, namely, the problems of scattering by closed and open surfaces. These two important scattering problems are briefly described in the following two sections.

4.1.1 Closed surfaces

For the case of a closed, bounded obstacle, we use a standard combined-field formulation [32]

$$U^{\text{scat}}(\boldsymbol{r}) = \mathscr{D}[\,\widetilde{\varphi}\,](\boldsymbol{r}) - ik\mathscr{S}[\,\widetilde{\varphi}\,](\boldsymbol{r}), \quad \boldsymbol{r} \in \mathbb{R}^3 \setminus \overline{\Gamma}, \tag{4.5}$$

which leads to the second-kind integral equation at the boundary

$$\frac{1}{2}\,\widetilde{\varphi}(\boldsymbol{r}) + D[\,\widetilde{\varphi}\,](\boldsymbol{r}) - ikS[\,\widetilde{\varphi}\,](\boldsymbol{r}) = -U^{\mathrm{inc}}(\boldsymbol{r}), \quad \boldsymbol{r} \in \Gamma, \tag{4.6}$$

where the single- and double-layer boundary operators are defined as

$$S[\,\widetilde{\varphi}\,](\boldsymbol{r}) = \int_\Gamma G(\boldsymbol{r},\boldsymbol{r}')\,\widetilde{\varphi}(\boldsymbol{r}')\,\mathrm{d}\sigma(\boldsymbol{r}'), \quad \boldsymbol{r} \in \Gamma, \tag{4.7}$$

$$D[\,\widetilde{\varphi}\,](\boldsymbol{r}) = \int_\Gamma \frac{\partial G(\boldsymbol{r},\boldsymbol{r}')}{\partial \boldsymbol{n}(\boldsymbol{r}')}\,\widetilde{\varphi}(\boldsymbol{r}')\,\mathrm{d}\sigma(\boldsymbol{r}'), \quad \boldsymbol{r} \in \Gamma, \tag{4.8}$$

respectively.

This formulation is guaranteed to provide a unique density solution to the scattering problem considered here [32], and due to the nature of this second-kind integral equation, the number of iterations for GMRES remains essentially bounded as k is increased.

4.1.2 Open surfaces

The combined field formulation (4.5) is not applicable for problems of scattering by open surfaces—since, for example, the jump conditions for the double-layer potential over Γ imply different field values on the two sides of Γ; hence, this potential cannot satisfy a nontrivial Dirichlet boundary value problem on Γ. A single-layer formulation can be used for such purpose, however; in this case we have

$$U^{\mathrm{scat}}(\boldsymbol{r}) = \mathscr{S}[\,\widetilde{\varphi}\,](\boldsymbol{r}), \quad \boldsymbol{r} \in \mathbb{R}^3 \setminus \overline{\Gamma}, \tag{4.9}$$

which, for the boundary conditions (4.2), leads to a first-kind integral equation

$$S[\,\widetilde{\varphi}\,](\boldsymbol{r}) = -U^{\mathrm{inc}}(\boldsymbol{r}), \quad \boldsymbol{r} \in \Gamma. \tag{4.10}$$

This is in fact the formulation recommended in [17] for the Dirichlet problem (see e.g. [section 12]), even in the presence of the better-conditioned, but more expensive second-kind formulation introduced in that contribution. (In the Neumann case, which, for definiteness we do not consider here, the second-kind formulation is highly beneficial [17, section 12].)

We use the formulation (4.9), as recommended, but it adopts an alternative quadrature approach, which is based once again on the proposed rectangular-polar

paradigm. An important aspect of the open-surface case is that the solution $\widetilde{\varphi}(\boldsymbol{r})$ is singular at the edge, with a singularity of the form

$$\widetilde{\varphi} \sim \frac{\Phi}{\sqrt{d}}, \tag{4.11}$$

where d is the distance to the edge and Φ is an infinitely differentiable function throughout the boundary, including the edge, as reviewed in [17]. In that paper, a strategy based on quadrature rules for the exact singularity form were introduced, together with the polar integration method [15]. We propose an alternative approach in which, in addition of the polar-rectangular setup, a change of variables is introduced in the parametrization of the surface, whose derivatives vanish at the edges and thus smoothens the integrands. Although not specifically tailored to the exact form of the singularity at open-surface edges, the proposed algorithm does provide a robust, highly-accurate, efficient and simple approach for the treatment of the density-singularities that arise for open surfaces—which, importantly, applies seamlessly to the closed-surface edge case, for which the degree of the singularity depends on the edge angle, which may itself vary along the edge.

4.2 Surface representation

The proposed method assumes that the scattering surface, whether closed or open, is described by a set of M non-overlapping "logically-quadrilateral" (LQ) parametrized patches. This geometrical description is particularly well suited for designs generated by CAD software, which generally can export surface representations in terms of NURBS-based models—that is, parametrizations expressed in terms of certain types of Rational B-Splines. In fact, the potential afforded by direct use of CAD-exported representations (without the expense, difficulty and accuracy deterioration inherent in the use of surface triangulations) provided the driving force leading to this chapter: each NURBS trimmed surface can be "quadrilateralized" without great difficulty, which lends the method an essentially complete geometric generality and a remarkable ease of use.

In the proposed approach, then, the scattering surface Γ is partitioned on the basis of a finite number M of parametrizations

$$\widetilde{\boldsymbol{r}}^{\,q} : [-1,1]^2 \to \mathbb{R}^3 \quad (q = 1, 2, \ldots, M),$$

each one of which maps the unit square $[-1,1]^2$ in the (s,t)-plane onto an LQ patch within Γ. Since we require the system of LQ patches to cover Γ, we have, in

particular

$$\Gamma = \bigcup_{q=1}^{M} \left\{ \widetilde{\boldsymbol{r}}^{\,q}(s,t) \;\middle|\; (s,t) \in [-1,1]^2 \right\}. \tag{4.12}$$

Clearly, any $\boldsymbol{r}$-dependent combination $I = I(\boldsymbol{r})$ of integrals over Γ, of the types considered in sections 4.1.1 and 4.1.2, can be decomposed as a sum of integrals $I^q(\boldsymbol{r})$ over the various patches. In particular, the integral representations and boundary operators considered in those sections can be expressed in the form

$$I(\boldsymbol{r}) = \sum_{q=1}^{M} I^q(\boldsymbol{r}), \quad \text{where} \tag{4.13}$$

$$I^q(\boldsymbol{r}) = \int_{\Gamma^q} \widetilde{\mathrm{H}}(\boldsymbol{r},\boldsymbol{r}')\,\widetilde{\varphi}(\boldsymbol{r}')\,\mathrm{d}\sigma(\boldsymbol{r}'), \tag{4.14}$$

with

$$\widetilde{\mathrm{H}}(\boldsymbol{r},\boldsymbol{r}') = \begin{cases} \dfrac{\partial G(\boldsymbol{r},\boldsymbol{r}')}{\partial \boldsymbol{n}(\boldsymbol{r}')} - ikG(\boldsymbol{r},\boldsymbol{r}'), & \text{(Closed surface)}, \\ G(\boldsymbol{r},\boldsymbol{r}'), & \text{(Open surface)}. \end{cases} \tag{4.15}$$

In the following section, we propose a methodology for accurate numerical evaluation of the integrals $I^q(\boldsymbol{r})$ for a given discrete approximation of the density $\widetilde{\varphi}(\boldsymbol{r}')$. The solution to the integral equation problem then follows via an application of the iterative linear-algebra solver GMRES.

4.3 Integration strategy

The integration scheme we present consists of three main components: (1) Use of Fejér's first quadrature rule to compute integrals between patches that are "far" away from each other, (2) A rectangular-polar high-order accurate quadrature rule for self-patch and near-patch singular integrals, and (3) A change of variables that resolves the density singularities that arise at the edges.

Using, for each q, the parametrization $\widetilde{\boldsymbol{r}}^{\,q}$, the integral (4.14) can be expressed in the form

$$I^q(\boldsymbol{r}) = \int_{-1}^{1}\int_{-1}^{1} \widetilde{\mathrm{H}}^q(\boldsymbol{r},s,t)\widetilde{J}^q(s,t)\widetilde{\varphi}^q(s,t)\mathrm{d}s\,\mathrm{d}t, \quad (\boldsymbol{r} \in \Gamma), \tag{4.16}$$

where $\widetilde{J}^q(s,t)$ denotes the surface Jacobian, and where

$$\widetilde{\mathrm{H}}^q(\boldsymbol{r},s,t) = \widetilde{\mathrm{H}}\left(\boldsymbol{r},\widetilde{\boldsymbol{r}}^{\,q}(s,t)\right), \tag{4.17}$$

$$\widetilde{\varphi}^q(s,t) = \widetilde{\varphi}\left(\widetilde{\boldsymbol{r}}^{\,q}(s,t)\right). \tag{4.18}$$

The strategy proposed for evaluation of the integral in equation (4.16) depends on the proximity of the point $\boldsymbol{r}$ to the q-th patch. For points $\boldsymbol{r}$ that are "far" from the patch, Fejér's first quadrature rule is used as detailed in section 4.3.2. A special technique, the rectangular-polar method, is then presented in section 4.3.3 to treat the case in which $\boldsymbol{r}$ is either "close to" or within the q-th patch. Prior to the presentation of these smooth, singular and near-singular integration methods, section 4.3.1 describes the singular character of integral-equation densities at edges, and proposes a methodology, which is incorporated in the subsequent sections, for edge treatment in a high-order accurate fashion.

4.3.1 Density singularities along edges

The sharp edges encountered in general geometric structures have provided a persistent source of difficulties to integral equation methods and other scattering solvers. The presence of edges leads to (integrable) singularities in the density solutions in both the open-surface [17] and closed-surface [33, 57] cases. The strength of the singularity, however, depends on the formulation and, for closed-surfaces, on the angle at the edge, which is generally not constant.

In order to tackle this difficulty in a general and robust manner, we introduce a change of variables on the parametrization variables (s, t), a number of whose derivatives vanish along edges. Such changes of variables can be devised on the basis of mappings such as the one presented in [32, Sec. 3.5], which is given by

$$w(\tau) = 2\pi \frac{[v(\tau)]^p}{[v(\tau)]^p + [v(2\pi - \tau)]^p}, \quad 0 \le \tau \le 2\pi, \tag{4.19}$$

where

$$v(\tau) = \left(\frac{1}{p} - \frac{1}{2}\right)\left(\frac{\pi - \tau}{\pi}\right)^3 + \frac{1}{p}\left(\frac{\tau - \pi}{\pi}\right) + \frac{1}{2}. \tag{4.20}$$

It is easy to check that the derivatives of $w(\tau)$ up to order $p - 1$ vanish at the endpoints. The function $w(\tau)$ can then be used to construct a change of variables to accurately resolve the edge singularities while mapping the interval $[-1, 1]$ to itself. The change-of-variable mappings we use are given by

$$s = \eta_s^q(u) = \begin{cases} u, & \text{No edge on } s \\ -1 + \frac{1}{\pi} w\left(\pi[u+1]\right), & \text{Edges at } s \pm 1 \\ -1 + \frac{2}{\pi} w\left(\frac{\pi}{2}[u+1]\right), & \text{Edge at } s = -1 \text{ only} \\ -3 + \frac{2}{\pi} w\left(\pi + \frac{\pi}{2}[u+1]\right), & \text{Edge at } s = 1 \text{ only} \end{cases} \tag{4.21}$$

and similarly

$$t = \eta_t^q(v) = \begin{cases} v, & \text{No edge on } t \\ -1 + \frac{1}{\pi} w\left(\pi[v+1]\right), & \text{Edges at } t \pm 1 \\ -1 + \frac{2}{\pi} w\left(\frac{\pi}{2}[v+1]\right), & \text{Edge at } t = -1 \text{ only} \\ -3 + \frac{2}{\pi} w\left(\pi + \frac{\pi}{2}[v+1]\right), & \text{Edge at } t = 1 \text{ only} \end{cases} \tag{4.22}$$

Incorporating the changes of variables (4.21) and (4.22), the integral in equation (4.16) becomes an integral in which a weakly singular kernel is applied to a finitely smooth function:

$$I^q(\boldsymbol{r}) = \int_{-1}^{1} \int_{-1}^{1} \mathrm{H}^q(\boldsymbol{r}, u, v) J^q(u, v) \frac{d\eta_s^q}{du}(u) \frac{d\eta_t^q}{dv}(v) \varphi^q(u, v) \mathrm{d}u \, \mathrm{d}v, \quad \boldsymbol{r} \in \Gamma, \tag{4.23}$$

where

$$\mathrm{H}^q(\boldsymbol{r}, u, v) = \widetilde{\mathrm{H}}^q\left(\boldsymbol{r}, \eta_s^q(u), \eta_t^q(v)\right), \tag{4.24}$$

$$\varphi^q(u, v) = \widetilde{\varphi}^q\left(\eta_s^q(u), \eta_t^q(v)\right), \tag{4.25}$$

$$\boldsymbol{r}^q(u, v) = \widetilde{\boldsymbol{r}}^q\left(\eta_s^q(u), \eta_t^q(v)\right), \tag{4.26}$$

$$J^q(u, v) = \widetilde{J}^q(s, t). \tag{4.27}$$

(The high-order edge-vanishing factors in the integrand smooth-out any possible edge singularities in the density φ^q [32].) The proposed algorithm evaluates such integrals by means of the "smooth-density methods" described in sections 4.3.2 and 4.3.3 below.

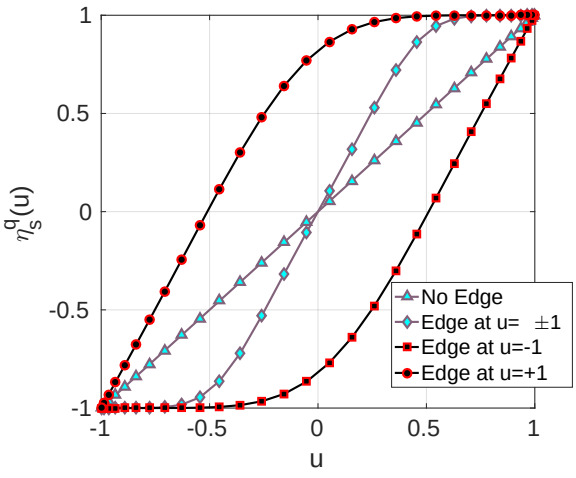

Figure 4.1: Changes of variables (equations (4.21) and (4.22)) used to resolve edge-singularities in the density.

4.3.2 Non-adjacent integration

The algorithm we use for the evaluation of the quantity $I^q(\boldsymbol{r})$, defined by (4.16), is based on the reformulation (4.23)—which, in view of (4.21) and (4.22), takes into account all the possible edge/no-edge combinations that may occur within an integration patch. (The algorithm does assume that geometric singularities may only appear along patch boundaries.)

In the "non-adjacent" integration case considered in this section, in which the point $\boldsymbol{r}$ is far from the integration patch, the integrand in (4.23) is smooth—in view of the changes of variables inherent in that equation, which, in particular, give rise to edge-vanishing derivative factors that smooth out any possible edge-singularity in the density φ^q itself. (Using well known asymptotics of edge singularities it is easy to check [19, 32] that the vanishing derivatives indeed smooth out all possible edge singularities, to any desired order of smoothness, provided a sufficiently high value of p is used. Values of p as low as $p = 2$ are often found to be adequately useful, for accuracies of the order of 1%. Use of larger values of p, of the orders of four to six or above, can enable significantly faster convergence and lower computing costs for higher accuracies. But use of such values do require special treatment of certain types of Green-function cancellations that occur in the case of the double-layer operator. Such discussions lie beyond the scope of the present chapter, and will be left for future work.

In view of the smoothness of the integrands for the non-adjacent cases considered presently ($\boldsymbol{r}$ is far from the integration patch), the integral in (4.23) can be evaluated accurately on the basis of any given high-order quadrature rule. Our implementation utilizes Fejér's first quadrature rule [79], which effectively exploits the discrete orthogonality property satisfied by the Chebyshev polynomials in the Chebyshev meshes used. The Chebyshev discrete orthogonality property also enables straightforward computation of the two-dimensional Chebyshev transforms that are required as part of the singular and near-singular integration algorithms described in section 4.3.3.

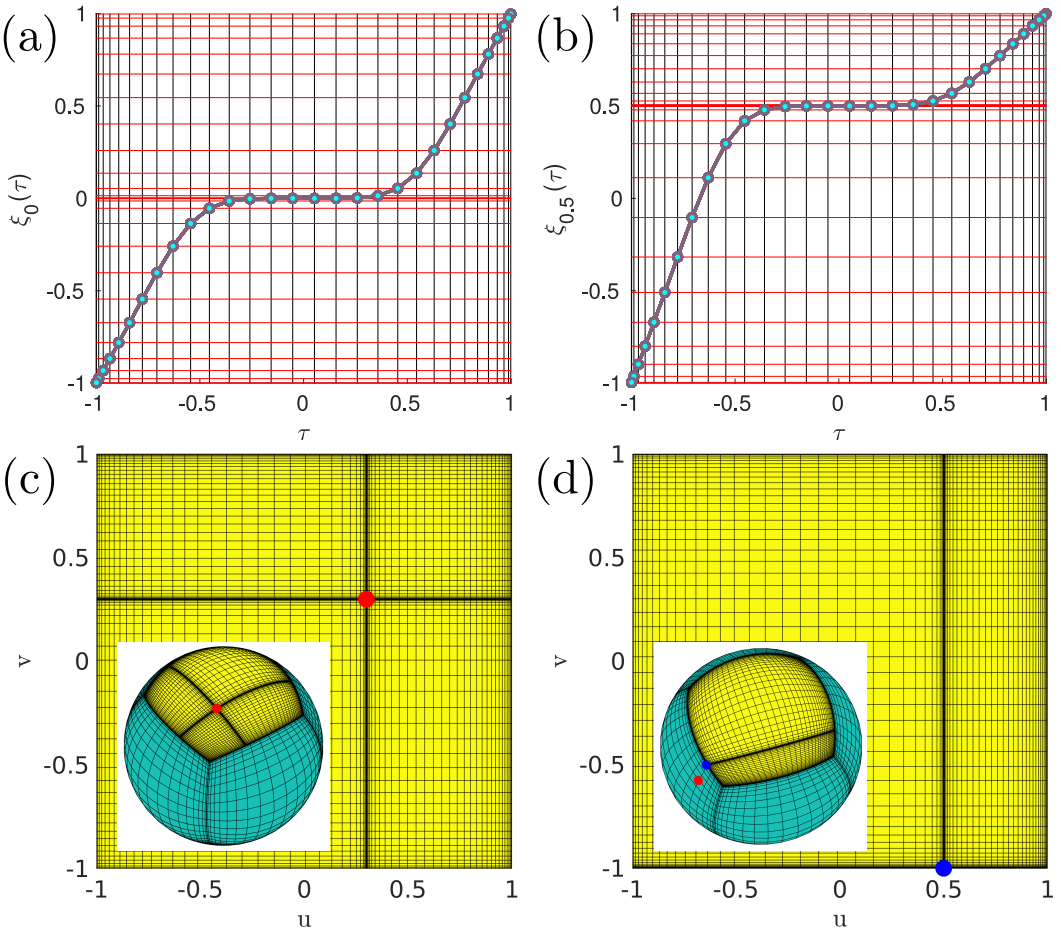

Figure 4.2: Figures (a) and (b) show the changes of variables (equation (4.40)) used to resolve the kernel singularity for two different values of α. Figure (c) presents the mesh, in both parameter and, in inset, real space, produced by the rectangular-polar change of variables to resolve the kernel singularity located at the point marked in red. Figure (d) presents the case for which the target point in red is off-patch from the near source patch (in yellow), with the projection point depicted in blue.

For a discretization using N points, the nodes and weights of Fejér's first quadrature rule are given by

$$x_j = \cos\left(\pi \frac{2j+1}{2N}\right), \quad j = 0, \ldots, N-1, \tag{4.28}$$

$$w_j = \frac{2}{N}\left(1 - 2\sum_{\ell=1}^{\lfloor N/2 \rfloor} \frac{1}{4\ell^2 - 1}\cos\left(\ell\pi \frac{2j+1}{N}\right)\right), \quad j = 0, \ldots, N-1, \tag{4.29}$$

respectively. Then using the Cartesian-product discretization $\{u_i = x_i | i = 0, \ldots, N_u^q - 1\} \times \{v_j = x_j | j = 0, \ldots, N_v^q - 1\}$, the integral in (4.16) can be approximated by the

quadrature expression

$$I^q(\boldsymbol{r}) \approx \sum_{j=0}^{N_v^q-1} \sum_{i=0}^{N_u^q-1} \mathrm{H}^q(\boldsymbol{r}, u_i, v_j) J^q(u_i, v_j) \frac{d\eta_s^q}{du} \frac{d\eta_t^q}{dv} w_i w_j \, \varphi^q(u_i, v_j), \quad \boldsymbol{r} \in \Omega_q^f. \tag{4.30}$$

where Ω_q^f represents the set of points that are "sufficiently far" from the q-th integration patch.

4.3.3 Singular "rectangular-polar" integration algorithm and a new edge-resolved integral unknown

Like section 4.3.2, the present section concerns the problem of evaluation of the quantity $I^q(\boldsymbol{r})$ on the basis of the reformulation (4.23). In contrast with section 4.3.2, however, the treatment presented here concerns the singular and near-singular cases—in which the evaluation point $\boldsymbol{r}$ is either on the q-th integration patch or "sufficiently close" to it—for which the Green function singularity cannot be ignored without compromising accuracy. The set of all singular and near-singular points will be denoted by Ω_q^c. The problem of evaluation of I^q for $\boldsymbol{r} \in \Omega_q^c$ presents a significant challenge in view of the singularity of the kernel $\widetilde{\mathrm{H}}(\boldsymbol{r}, \boldsymbol{r}')$ at $\boldsymbol{r} = \boldsymbol{r}'$.

In order to deal with this difficulty, we utilize once again smoothing changes of variables whose derivatives vanish at the singularity or, for nearly singular problems, at the point in the q-th patch that is closest to the singularity. In previous implementations [15, 17], such changes of variables required interpolation of the density φ^q from the fixed nodes (u_i, v_j) to the new integration points. The interpolation step, though viable, can amount to a significant portion of the overall cost. We thus propose, instead, use of a precomputation scheme for which integrals of the kernel times Chebyshev polynomials are evaluated with high accuracy (cf. (4.35)). Since Chebyshev polynomials can easily be evaluated at any point in their domain of definition, this approach does not require an interpolation step. And, since these integrals are independent of the density, they need only be computed once at the beginning of any application of the algorithm, and reused in the algorithm as part of any necessary integration processes in subsequent linear-algebra (GMRES) iterations. Thus, for a given density φ^q, the overall quantity $I^q(\boldsymbol{r})$ with $\boldsymbol{r} \in \Omega_q^c$ can be computed by first obtaining the Chebyshev expansion

$$\psi^q(u, v) = \sum_{m=0}^{N_v^q-1} \sum_{n=0}^{N_u^q-1} a_{n,m}^q T_n(u) T_m(v), \tag{4.31}$$

of the modified edge-resolved (smooth) density

$$\psi^q(u,v) = \frac{d\eta_s^q}{du}(u)\frac{d\eta_t^q}{dv}(v)\varphi^q(u,v),$$

and then applying the precomputed integrals for Chebyshev densities.

In detail, the necessary Chebyshev coefficients $a_{n,m}^q$ are given by the relation [72]

$$a_{n,m}^q = \frac{\alpha_n\alpha_m}{N_u^q N_v^q}\sum_{j=0}^{N_v^q-1}\sum_{i=0}^{N_u^q-1}\psi^q(u_i,v_j)T_n(u_i)T_m(v_j) \tag{4.32}$$

that results from the discrete-orthogonality property enjoyed by Chebyshev polynomials, where

$$\alpha_n = \begin{cases} 1, & n = 0, \\ 2, & n \neq 0. \end{cases} \tag{4.33}$$

As is well known, the Chebyshev coefficients $a_{n,m}^q$ can be computed in a fast manner either by means of the FFT algorithm or, for small expansion orders, by means of partial summation [11, Sec. 10.2]. In practice, relatively small orders and numbers of discretization points are used, and we thus opted for the partial summation strategy.

Using the expansion (4.31), we then obtain

$$I^q(\boldsymbol{r}) = \int_{-1}^{1}\int_{-1}^{1}\mathrm{H}^q(\boldsymbol{r},u,v)J^q(u,v)\left(\sum_{m=0}^{N_v^q-1}\sum_{n=0}^{N_u^q-1}a_{n,m}^q T_n(u)T_m(v)\right)\mathrm{d}u\,\mathrm{d}v \tag{4.34}$$

from which, exchanging the integrals with the sum, it follows that

$$I^q(\boldsymbol{r}) = \sum_{m=0}^{N_v^q-1}\sum_{n=0}^{N_u^q-1}a_{n,m}^q\int_{-1}^{1}\int_{-1}^{1}\mathrm{H}^q(\boldsymbol{r},u,v)J^q(u,v)T_n(u)T_m(v)\,\mathrm{d}u\,\mathrm{d}v. \tag{4.35}$$

As mentioned above, the double integrals on the right-hand side of this equation are independent of the density: for each q, they only depend on the geometry, the kernel, and the target point $\boldsymbol{r} \in \Omega_q^c$. For the computation of the forward map, we need, in particular, to evaluate $I^q(\boldsymbol{r})$ for all *discretization points* $\boldsymbol{r} \in \Omega_q^c$. Thus, in the proposed strategy, the integral in (4.35) must be precomputed for each q and for each combination of a target point $\boldsymbol{r} \in \Omega_q^c$ and a relevant product of Chebyshev polynomials. Denoting the set of all discretization points by

$$\chi = \left\{\widetilde{\boldsymbol{r}}^{\,q}\left(\eta_s^q(u_i),\eta_t^q(v_j)\right)\,\middle|\,q = 1,\ldots,M,\ i = 0,\ldots,N_u^q-1,\ j = 0,\ldots,N_v^q-1\right\}, \tag{4.36}$$

and using the weights

$$\beta_{n,m}^{q,\ell} = \int_{-1}^{1}\int_{-1}^{1} \mathrm{H}^q(\boldsymbol{r}_\ell, u, v) J^q(u,v) T_n(u) T_m(v)\,\mathrm{d}u\,\mathrm{d}v, \quad \text{for each } \boldsymbol{r}_\ell \in \left\{\chi \cap \Omega_q^c\right\}, \tag{4.37}$$

equation (4.35) becomes

$$I^q(\boldsymbol{r}_\ell) = \sum_{m=0}^{N_v^q-1}\sum_{n=0}^{N_u^q-1} a_{n,m}^q\, \beta_{n,m}^{q,\ell}\ . \tag{4.38}$$

We now turn our attention to the accurate evaluation of the integrals in equation (4.37). The previous method [15] utilizes (in a different context, and without precomputations) a polar change of variables that cancels the kernel singularity and thus gives rise to high-order integration. Reference [15] relies on overlapping parametrized patches and partitions of unity to facilitate the polar-integration step. In the case in which non-overlapping LQ patches are utilized, the use of polar integration requires design of complex quadratures near all patch boundaries [17]. To avoid these difficulties, we propose use of certain "rectangular-polar" changes of variables which, like the edge changes-of-variables utilized in section 4.3.2, are based on use of the functions (4.19)–(4.20) for suitable values of p.

We thus seek to devise a rectangular-polar integration strategy that can accurately treat the kernel singularity for both the self-patch problem (in which the singularity lies on the integration patch and for which changes of variables should have vanishing derivatives at the target point $\boldsymbol{r}_\ell$), and the near-singular problem (in which vanishing change-of-variable derivatives should occur at the point in the q-th patch that is closest to the observation point $\boldsymbol{r}$). To achieve this, it is necessary to consider the value

$$\left(\overline{u}_\ell^q, \overline{v}_\ell^q\right) = \underset{(u,v)\in[-1,1]^2}{\arg\min}\ |\,\boldsymbol{r}_\ell - \boldsymbol{r}^{\,q}(u,v)\,|, \tag{4.39}$$

which can be found by means of an appropriate minimization algorithm. In view of its robustness and simplicity, our method utilizes the golden section search algorithm (see [72, Sec. 10.2]) for this purpose, with initial bounds obtained from a direct minimization over all of the original discretization points $\boldsymbol{r}_\ell$ in the patch. Relying on the coordinates (4.39) of the projection point in the near-singular case, and using the same notation $\left(\overline{u}_\ell^q, \overline{v}_\ell^q\right)$ for the coordinates of the singular point in the self-patch problem, the relevant rectangular-polar change of variable can be

constructed on the basis of the one-dimensional change of variables

$$\xi_\alpha(\tau) = \begin{cases} \alpha + \left(\dfrac{\operatorname{sgn}(\tau) - \alpha}{\pi}\right) w\left(\pi|\tau|\right), & \text{for } \alpha \neq \pm 1, \\ \alpha - \left(\dfrac{1+\alpha}{\pi}\right) w\left(\pi\left|\dfrac{\tau-1}{2}\right|\right), & \text{for } \alpha = 1, \\ \alpha + \left(\dfrac{1-\alpha}{\pi}\right) w\left(\pi\left|\dfrac{\tau+1}{2}\right|\right), & \text{for } \alpha = -1. \end{cases} \tag{4.40}$$

Figure 4.2 depicts the rectangular-polar change of variables for α values of (a) 0 and (b) 0.5, as well as the resulting two-dimensional grids for the case where the target point lies in the source patch (c) and when the target point is off-patch (d).

Indeed, a new use of Fejér's first quadrature rule now yields

$$\beta_{n,m}^{q,\ell} \approx \sum_{j=0}^{N_\beta^v - 1} \sum_{i=0}^{N_\beta^u - 1} \mathrm{H}^q\left(\boldsymbol{r}_\ell, u_i^{q,\ell}, v_j^{q,\ell}\right) J^q\left(u_i^{q,\ell}, v_j^{q,\ell}\right) T_n\left(u_i^{q,\ell}\right) T_m\left(v_j^{q,\ell}\right) \mu_i^{u,q,\ell} \mu_j^{v,q,\ell} w_i\, w_j, \tag{4.41}$$

where

$$u_i^{q,\ell} = \xi_{\overline{u}_\ell^q}\left(x_i\right), \quad \text{for } i = 0, \ldots, N_\beta^u - 1, \tag{4.42}$$

$$v_j^{q,\ell} = \xi_{\overline{v}_\ell^q}\left(x_j\right), \quad \text{for } j = 0, \ldots, N_\beta^v - 1, \tag{4.43}$$

are the new quadrature points, and where

$$\mu_i^{u,q,\ell} = \frac{d\xi_{\overline{u}_\ell^q}}{d\tau}\left(x_i\right), \quad \text{for } i = 0, \ldots, N_\beta^u - 1, \tag{4.44}$$

$$\mu_j^{v,q,\ell} = \frac{d\xi_{\overline{v}_\ell^q}}{d\tau}\left(x_j\right), \quad \text{for } j = 0, \ldots, N_\beta^v - 1, \tag{4.45}$$

denote the corresponding change-of-variable weights. Using sufficiently large numbers N_β^u and N_β^v of discretization points along the u and v directions to accurately resolve the challenging integrands, all singular and near-singular problems can be treated with high accuracy under discretizations that are not excessively fine (see Figure 4.3). For points that are closer than a certain prescribed tolerance, usually of the order 10^{-14}, the kernel values are set to zero to avoid zero denominators.

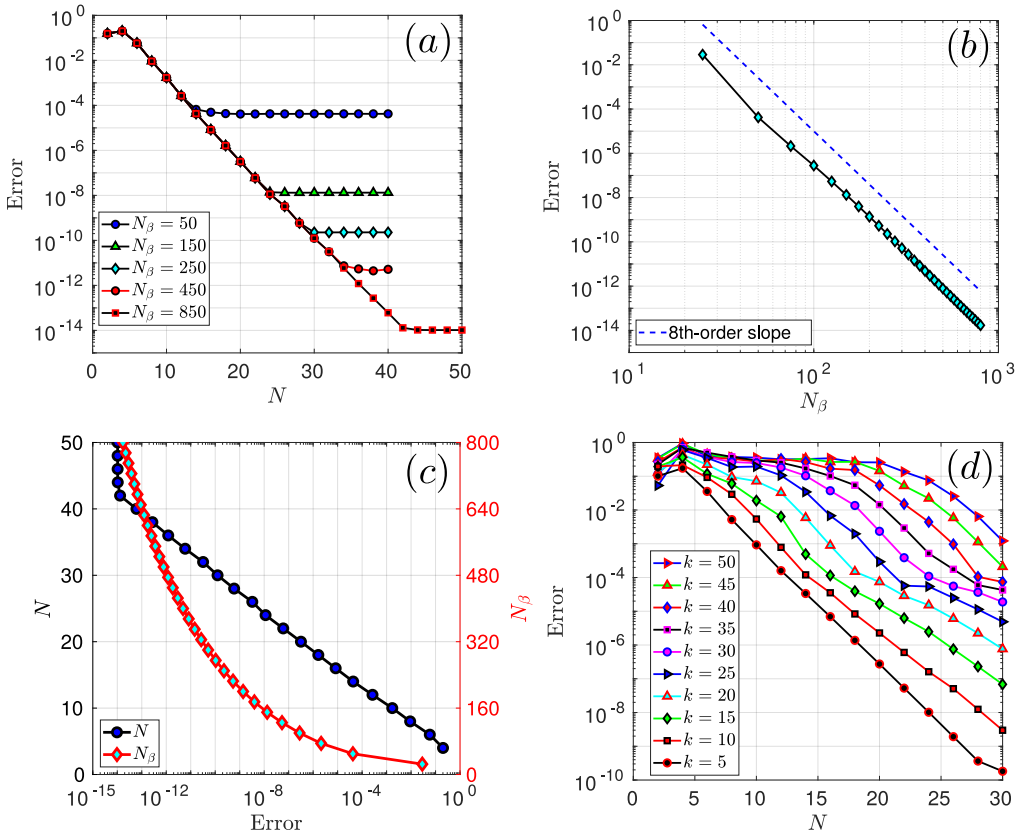

Figure 4.3: Forward-map convergence for the combined field formulation over the unit sphere. Figure (a) displays the error as the number N of points per patch per dimension is increased for different values of N_β. Figure (b) demonstrates the high-order convergence for the singular integrals as N_β is increased. Figure (c) displays the optimal values of N and N_β for a given prescribed error. In (a)-(c), we have $k = 2\pi$. Figure (d) demonstrates the convergence for a range of values of k while keeping the number of patches fixed.

4.3.4 Computational cost

Let us now estimate the computational cost for the proposed method, focusing on the adjacent (singular and near-singular) integration problem. (The cost of the non-adjacent interactions arises trivially from a double sum, and can be accelerated by means of either an equivalent source scheme [15, 16] or by a fast multipole approach [43].)

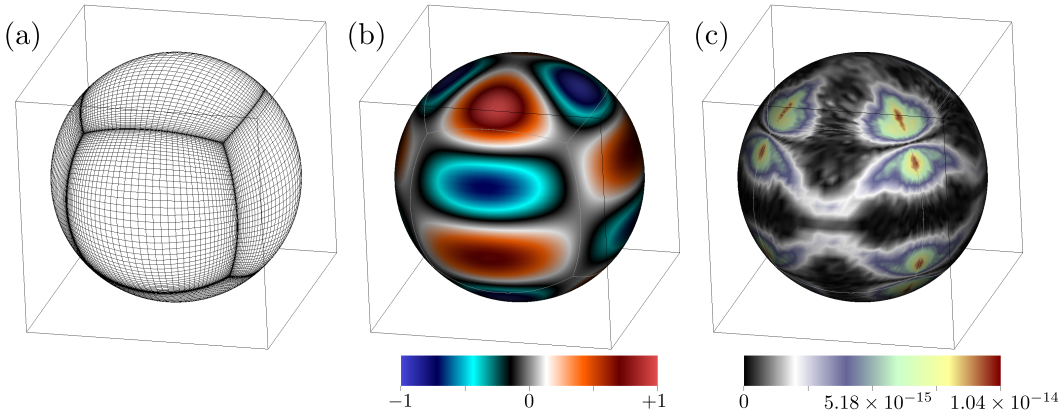

Figure 4.4: (a) Mesh, (b) Forward map, and (c) Pointwise error for a (5, 2)-spherical-harmonic density using a mesh with $N = 50$ and $N_\beta = 850$. The error is uniformly close to machine precision.

For the purposes of our computing-time estimates, let N denote the maximum of the one dimensional discretization sizes N_u^q and N_v^q over all patches ($1 \leq q \leq M$), and let N'_{close} denote the maximum, over all the patches, of the numbers of discretization points that are close to the patch (i.e., that are contained in Ω_q^c), but which are not contained in the q-th patch. Additionally, let $N_\beta^u = N_\beta^v = N_\beta$ denote the number of quadrature points used for singular precomputations. With these notations, we obtain the following estimates in terms of the (bounded) integer N (of the order of one to a few tens); the (large, proportional to the square of the frequency, for large frequencies) number M of patches, and the related (bounded) parameters N_β (of the order of one to a few hundreds):

- Cost of precomputations: $O(MN_\beta^2 N(N^2 + N'_{\text{close}}))$ (partial summation).
- Cost of forward map:
  - Chebyshev transform (partial summation): $O(MN^3)$
  - Singular and near-singular interactions: $O(MN^2(N^2 + N'_{\text{close}}))$
  - Non-adjacent interactions $O((M-1)^2N^4)$ (or $M^\alpha N^4$ with α significantly smaller than two if adequate acceleration algorithms are utilized).

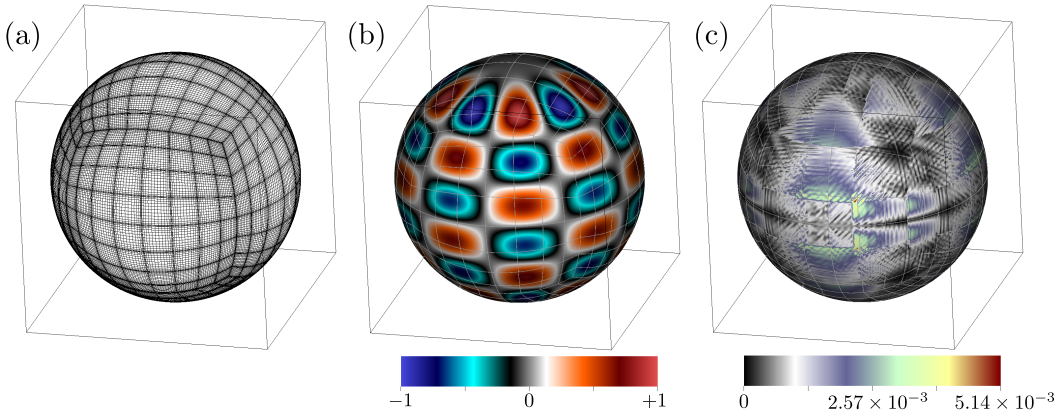

Figure 4.5: (a) Mesh, (b) Forward map, and (c) Pointwise error for the $(10, 5)$-spherical-harmonic density. The figures demonstrate the effect of the patch splitting strategy for high frequencies. In this case $k = 100$ which corresponds to scattering by a sphere 31.8λ in diameter, using $6 \times 8 \times 8$ patches (8×8 subpatches in each one of 6 initial patches) with $N = 14$.

4.3.5 Patch splitting for large problems

Each patch requires creation and storage of a set of self-interaction weights $\beta_{n,m}^{q,\ell}$, for $q = 1, \ldots, M$, $n = 1, \ldots, N$, $m = 1, \ldots, N$ and $\ell = 1, \ldots, N^2$, at a total storage cost of $O(MN^4)$ double-precision complex-valued numbers. Additionally, weights also need to be stored for the N'_{close} near-singular points for each patch, and are dependent on the target point. Hence, the total storage for the singular and near-singular weights is $O(MN^4 + MN^2N'_{\text{close}})$.

In order to eliminate the need to evaluate and store a large number of weights that result as N is increased, it is possible to instead increase the number of patches M—which causes the necessary number of weights to grow only linearly. In these regards, it is useful to consider the following rule of thumb: in practice, as soon as the wavelength is accurately resolved by the single-patch algorithm, due to the spectral accuracy of Fejér's first quadrature, only a few additional points per patch are needed to produce accuracies of the order of several digits. In view of the estimates in this and the previous section, parameter selections can easily be made by seeking to optimize the overall computing time given the desired accuracy and available memory.

4.4 Numerical results

This section presents a variety of numerical examples demonstrating the effectiveness of the proposed methodology. The particular implementation for the

numerical experiments was programmed in Fortran and parallelized using OpenMP. The runs were performed on a single node of a dual socket Dell R420 with two Intel Xenon E5-2670 v3 2.3 GHz, 128 GB of RAM. Unless otherwise stated, all runs where performed using 24 cores. Visualization of the three-dimensional geometries and acoustic fields was done using VisIt [26].

4.4.1 Forward map convergence

The accuracy of the overall solver depends crucially on the accuracy of the forward map computation. In this section, we verify that the proposed methodology yields uniformly accurate evaluations of the action of the integral operator throughout the surface of the scatterer. To do so, we consider the eigenfunctions and eigenvalues of the single- and double-layer operators for Helmholtz equation [63, Sec. 3.2.3]:

$$S[Y_\ell^m(\theta,\varphi)] = k\, j_\ell(k) h_\ell^{(1)}(k) Y_\ell^m(\theta,\varphi), \tag{4.46}$$

$$D[Y_\ell^m(\theta,\varphi)] = \frac{k^2}{2}\left[j_\ell(k) \frac{\mathrm{d}}{\mathrm{d}k} h_\ell^{(1)}(k) + h_\ell^{(1)} \frac{\mathrm{d}}{\mathrm{d}k} j_\ell(k) \right] Y_\ell^m(\theta,\varphi), \tag{4.47}$$

where $j_\ell(k)$ and $h_\ell^{(1)}(k)$ are the spherical Bessel function of the first kind and spherical Hankel function, respectively, and where $Y_\ell^m(\theta,\varphi)$ are the spherical harmonics. (For the spherical Hankel function $h_\ell^{(1)}(z)$, we have used the convention in [63]: $h_\ell^{(1)}(z) = -y_\ell(z) + i\ j_\ell(z)$, where y_ℓ is the ℓ-th Neumann function.)

Figure 4.3 demonstrates the convergence that results as the proposed discrete combined field operator is applied to the spherical-harmonic $(5, 2)$, demonstrating, in particular, that the method is capable of obtaining accuracies close to machine precision in the evaluation of forward maps. Figure 4.4 displays the spatial distribution of the (near-machine-precision) forward-map error resulting from the discretization described in the figure caption. It is worth noting that for the double-layer operator, the evaluation of the quantity $\boldsymbol{n}(\boldsymbol{r}') \cdot (\boldsymbol{r} - \boldsymbol{r}')/|\boldsymbol{r} - \boldsymbol{r}'|^2$ is particularly prone to cancellation errors, and to achieve small errors (10^{-6} or smaller), special treatment is required. For the particular case of the sphere, the aforementioned quantity can be computed exactly (which is used to obtain the plots in Figure 4.3), while for more complex geometries, a special treatment based on the curvature of the surface can be used [15].

As indicated in section 4.3.5, for high-frequency problems it is beneficial to split the patches into smaller ones rather than increasing the number of points per patch, given that the storage only grows linearly as the number of patches is increased

N	N_β	Patches	Points per λ	Unknowns	Time (prec.)	Time (1 iter.)	Error
8	50	$6\times5\times5$	1.7	9600	1.39 s	0.18 s	71.3%
12	60	$6\times5\times5$	2.6	21600	3.40 s	0.83 s	2.16%
16	80	$6\times5\times5$	3.5	38400	9.26 s	2.41 s	0.0814%
8	50	$6\times10\times10$	3.5	38400	16.74 s	2.78 s	0.336%
12	70	$6\times10\times10$	5.2	86400	47.26 s	13.01 s	0.0238%
16	90	$6\times10\times10$	6.9	153600	126.09 s	40.29 s	0.000355%

Table 4.1: Errors in the forward map (relative to the maximum forward map value) of the combined field operator for various patch splitting configurations and a spherical harmonic density (5,2). For the results in this table, $k = 100$, a sphere of diameter 31.8λ was used, and all times reported where obtained using 24 computing cores.

while keeping the number of points per patch constant. In order to determine the optimal balance between accuracy and efficiency, it must be considered that there are two factors that determine the accuracy of the method: (1) The order N of the Chebyshev expansions used (i.e. the number of points per patch per dimension), and (2) The number of points per wavelength. Figure 4.5 displays the pointwise error in the forward map for a high frequency case, and Table 4.1 presents test results for several simple patch-splitting configurations, where the number of points per wavelength is calculated by the formula

$$\text{Points per } \lambda = \frac{N}{L/\lambda}, \tag{4.48}$$

where $L^2 = 4\pi/M$ is the average area of the quadrilateral patches for the sphere. Clearly the method rapidly produces very high accuracies for small numbers of points-per-wavelength.

4.4.2 Edge geometries

As mentioned previously, the important problem of scattering by obstacles containing edges and corners presents a number of difficulties, including density and kernel singularities at the edges. In Figure 4.6(a), we demonstrate the performance of the method for a cube geometry, by computing the error in the far field with respect to a reference solution obtained by using a very fine discretization. Figure 4.7 shows the scattering solution by a cube of side 5λ.

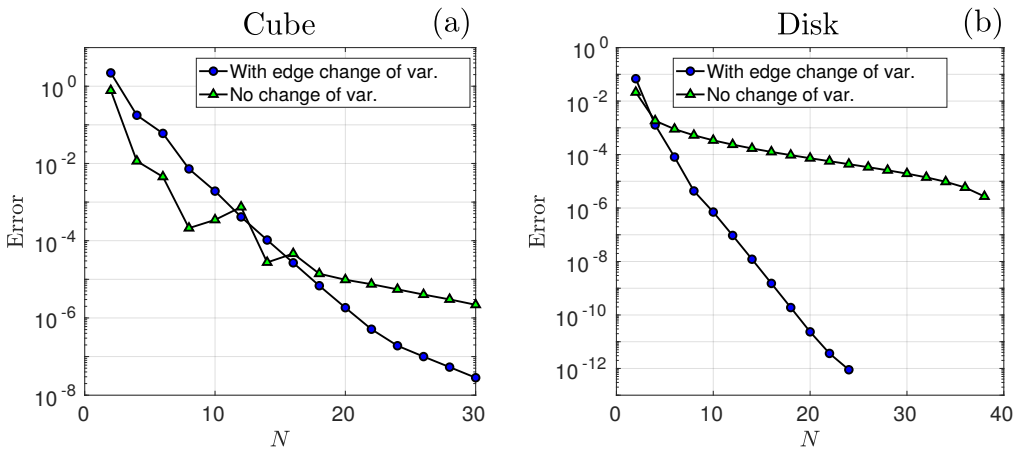

Figure 4.6: (a) Maximum (absolute) far-field error for the problem of scattering by a cube of size $2 \times 2 \times 2$ with $k = 1$. The plot shows results obtained excluding use of an edge change of variables (in green triangles) and including an edge change of variables with $p = 2$ (in blue circles). The maximum value of the far field for the reference solution equals 2.144. (b) Maximum (absolute) far-field error for the problem of scattering by a disk of radius 1 with $k = 1$. The plot shows both the curve excluding changes of variables (in green) and including a $p = 4$ change of variables (in blue). The maximum value of the far field for the reference solution equals 0.7284.

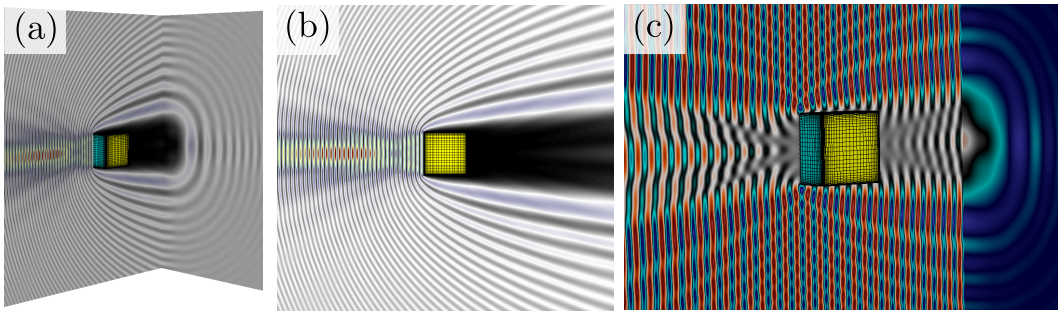

Figure 4.7: Scattering by a $5\lambda \times 5\lambda \times 5\lambda$ cube. The intensity profile $|U|^2$ is shown in (a) and (b), while (c) shows the real part of the total field.

4.4.3 Open surfaces

Methods for open surfaces typically suffer from low accuracies, or, alternatively, they require complex treatment at edges. The approach presented here is a straightforward application of the rectangular-polar method, with a change of variables at the edges, as described in section 4.3.3. As demonstrated in Figure 4.6(b), which presents the convergence plot for the far field solution scattered by a disk, the method is robust and high-order accurate. Figure 4.8 shows the scattering solution for the problem of scattering by a disk 5λ in radius.

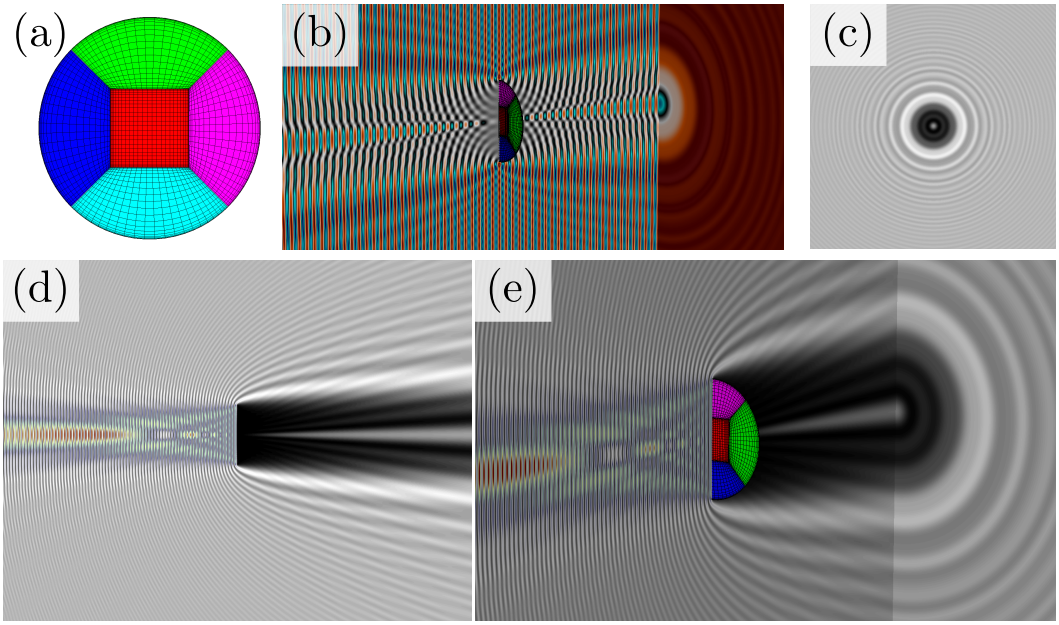

Figure 4.8: Scattering by a disk of diameter 10λ with an incident field perpendicular to the disk. Figure (a) displays the patch discretization, Figure (b) presents the real part of the field, and Figures (c)-(e) display three different views of the intensity $|U|^2$. In particular, these figures demonstrate the appearance of the well-known Poisson spot (also known as Arago spot and Fresnel bright spot) clearly visible at the center of Figure (c).

4.4.4 CAD geometries

As indicated in section 4.2, CAD designs can be re-expressed as a union of logically-quadrilateral explicitly parametrized patches, and they are thus particularly well suited for use in conjunction with the proposed rectangular-polar solver. To demonstrate the applicability of the solver to such general type of geometry descriptions, Figure 4.9 presents a convergence test for the acoustic scattering by a glider CAD design [39] consisting of 148 patches. Figure 4.10 shows the resulting fields by an incident plane wave incoming from above the glider—in this case, the patches where split into a total of 334 patches to have pairwise similar dimensions and accurately resolve the wavelength.

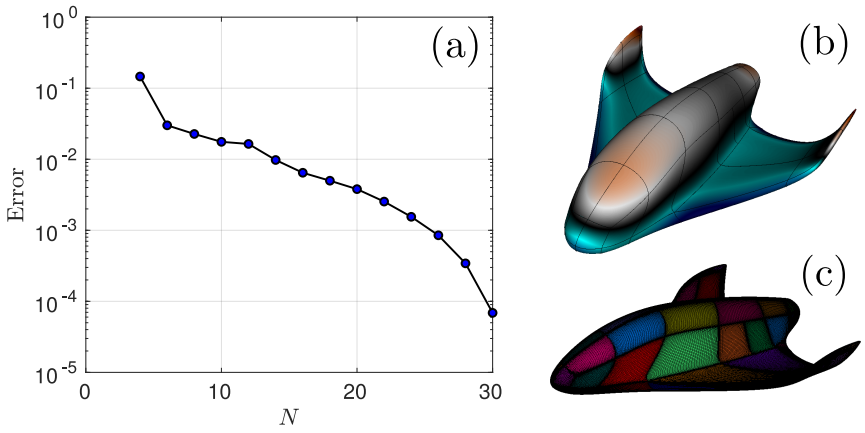

Figure 4.9: Figure (a) shows the maximum (absolute) far-field error for the problem of scattering by a glider geometry with $k = 1$. The reference density solution is shown in (b), and (c) shows the 148 patch discretization. For this convergence test, the longest distance between any two points on the aircraft surface is ~ 2.09 wavelengths, while the wingspan is ~ 1.43 wavelengths.

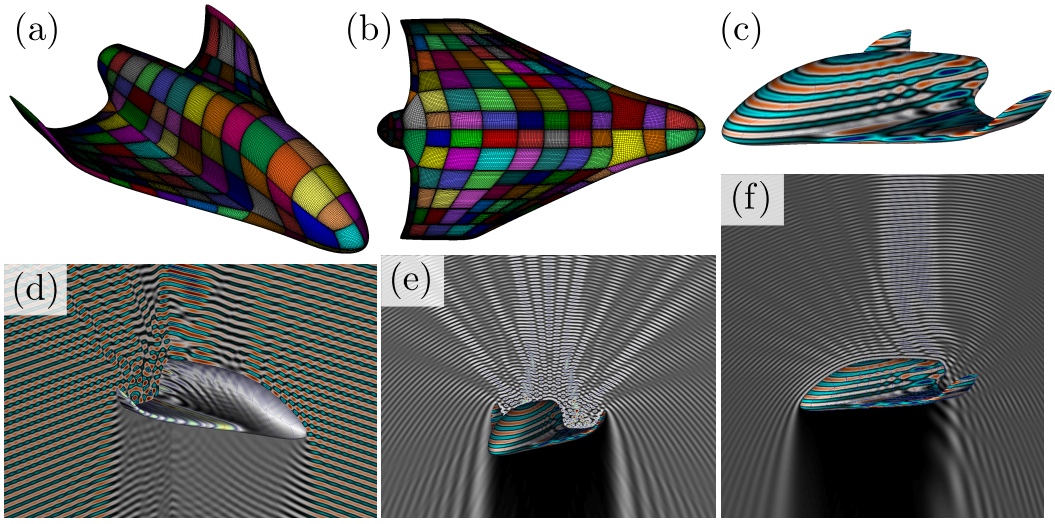

Figure 4.10: Scattering by the glider geometry. In this case, $\lambda = 0.5$ which results in about 26 wavelengths from the nose to the tail of the aircraft, and 18 wavelengths across the wingspan. The patches were subdivided to obtain, in all, 334 patches of pairwise similar dimensions. Figures (a) and (b) display the discretization and patch structure of the geometry. The real part of the density is shown in Figure (c). Figure (d) displays the real part of the scattered field along with the absolute value squared of the density at the surface. The intensity of the fields are presented in Figures (e) and (f) for two different view angles.

Chapter 5

ELECTROMAGNETIC BOUNDARY INTEGRAL EQUATIONS

This chapter presents the electromagnetic boundary integral formulations we use for three-dimensional problems of scattering by dielectric materials. First, we present some background material needed for the electromagnetic boundary integral equations (EM-BIE)—which is primarily a summary of key content from [63, section 2.5.6 and Chapter 5]. This background content is the backbone of the integral formulations for the three-dimensional electromagnetic problem, which are used throughout this thesis. In section 5.5, we explain how the rectangular-polar method can be used to solve the EM-BIE. Finally, section 5.6 briefly demonstrates the applicability of the rectangular-polar algorithm presented in Chapter 4 for dielectric-scattering problems.

5.1 Background on three-dimensional EM-BIE

This section presents key elements and tools that are used in the formulation and solution of three-dimensional electromagnetic integral equations. Two main subsections are included: one covering basic differential-geometry concepts, and a second one which, relying on the first one, presents the basic electromagnetic potentials and boundary integral operators. These operators are subsequently used in section 5.2 to present the electromagnetic representation theorems and associated integral equations we use.

5.1.1 Some concepts from differential geometry

Although the solver for the three-dimensional acoustic case (Chapter 4) requires some simple differential geometry quantities—mainly the normal vector and surface area element—the electromagnetic integral equations depend upon vector calculus quantities over surfaces. These concepts are introduced in what follows; a more detailed description can be found in [63, section 2.5.6].

Just as in Chapter 4, we assume the surface description is given by a set of M non-overlapping patches $\boldsymbol{r}^p(u, v)$ for $p = 1, \ldots M$. Based on this representation of the surface Γ, we introduce the following definitions:

Basis for the tangent plane:

$$\boldsymbol{e}_1(\boldsymbol{r}^p(u,v)) = \frac{\partial \boldsymbol{r}^p}{\partial u}, \tag{5.1a}$$

$$\boldsymbol{e}_2(\boldsymbol{r}^p(u,v)) = \frac{\partial \boldsymbol{r}^p}{\partial v}. \tag{5.1b}$$

Any vector $\boldsymbol{w}$ in the tangent plane (contravariant vector) can be written as

$$\boldsymbol{w} = w^1 \boldsymbol{e}_1 + w^2 \boldsymbol{e}_2. \tag{5.2}$$

The unit normal vector is given by

$$\boldsymbol{n} = \alpha \boldsymbol{e}_1 \times \boldsymbol{e}_2, \tag{5.3a}$$

$$|\alpha| = |\boldsymbol{e}_1 \times \boldsymbol{e}_2|^{-1}, \tag{5.3b}$$

where the sign of α depends on the orientation of the normal.

Metric tensor:

$$g_{ij} = (\boldsymbol{e}_i \cdot \boldsymbol{e}_j), \tag{5.4}$$

and its inverse g^{-1} with components

$$(g^{-1})_{ij} = g^{ij}. \tag{5.5}$$

Basis for the cotangent plane:

$$\boldsymbol{e}^i = g^{ij} \boldsymbol{e}_j, \tag{5.6}$$

Any vector $\boldsymbol{w}$ in the cotangent plane (covariant vector) can be expressed in the form

$$\boldsymbol{w} = w_1 \boldsymbol{e}^1 + w_2 \boldsymbol{e}^2. \tag{5.7}$$

Orthogonality:

The vector basis for the tangent and cotangent planes satisfy the orthogonality condition:

$$\boldsymbol{e}^i \cdot \boldsymbol{e}_j = \delta_{ij}, \tag{5.8}$$

where δ_{ij} denotes the Kronecker delta.

Surface area element:

$$\mathrm{d}\sigma(\boldsymbol{r}') = |\boldsymbol{e}_1 \times \boldsymbol{e}_2|\mathrm{d}u\,\mathrm{d}v = \sqrt{\det g}\;\mathrm{d}u\,\mathrm{d}v. \tag{5.9}$$

Surface gradient:

$$\nabla_\Gamma f = \frac{\partial f}{\partial u}\boldsymbol{e}^1 + \frac{\partial f}{\partial v}\boldsymbol{e}^2. \tag{5.10}$$

Surfacic divergence of a contravariant vector:

$$\mathrm{div}_\Gamma \boldsymbol{w} = \frac{1}{\sqrt{\det g}}\left(\frac{\partial}{\partial u}\left[\sqrt{\det g}\;w^1\right] + \frac{\partial}{\partial v}\left[\sqrt{\det g}\;w^2\right]\right). \tag{5.11}$$

5.1.2 Electromagnetic potentials and integral operators

For a wavenumber k and a density $\boldsymbol{d}$ in the tangent plane of the surface Γ, we define the vector potential operators [63]

$$\mathscr{S}[\boldsymbol{d}](\boldsymbol{r}) \equiv \int_\Gamma G(\boldsymbol{r},\boldsymbol{r}')\boldsymbol{d}(\boldsymbol{r}')\;\mathrm{d}\sigma(\boldsymbol{r}'), \tag{5.12a}$$

$$\mathscr{D}[\boldsymbol{d}](\boldsymbol{r}) \equiv \nabla \times \int_\Gamma G(\boldsymbol{r},\boldsymbol{r}')\boldsymbol{d}(\boldsymbol{r}')\;\mathrm{d}\sigma(\boldsymbol{r}'), \tag{5.12b}$$

$$\mathscr{K}[\boldsymbol{d}](\boldsymbol{r}) \equiv \nabla \int_\Gamma G(\boldsymbol{r},\boldsymbol{r}')\,\mathrm{div}_\Gamma \boldsymbol{d}(\boldsymbol{r}')\;\mathrm{d}\sigma(\boldsymbol{r}'), \tag{5.12c}$$

where, as in Chapter 4, $G(\boldsymbol{r},\boldsymbol{r}') = \exp(ik|\boldsymbol{r}-\boldsymbol{r}'|)/(4\pi|\boldsymbol{r}-\boldsymbol{r}'|)$ is the free-space Green's function of the Helmholtz equation. These potentials play an analogous role to that of the single- and double-layer of the acoustic scattering case.

Associated with the potentials in equation (5.12) are the tangential boundary integral operators

$$\mathrm{S}[\boldsymbol{d}](\boldsymbol{r}) \equiv -\boldsymbol{n}(\boldsymbol{r}) \times \int_\Gamma G(\boldsymbol{r},\boldsymbol{r}')\boldsymbol{d}(\boldsymbol{r}')\;\mathrm{d}\sigma(\boldsymbol{r}'), \tag{5.13a}$$

$$\mathrm{R}[\boldsymbol{d}](\boldsymbol{r}) \equiv -\boldsymbol{n}(\boldsymbol{r}) \times \nabla \times \int_\Gamma G(\boldsymbol{r},\boldsymbol{r}')\boldsymbol{d}(\boldsymbol{r}')\;\mathrm{d}\sigma(\boldsymbol{r}'), \tag{5.13b}$$

$$\mathrm{T}[\boldsymbol{d}](\boldsymbol{r}) \equiv -\boldsymbol{n}(\boldsymbol{r}) \times \nabla \int_\Gamma G(\boldsymbol{r},\boldsymbol{r}')\,\mathrm{div}_\Gamma \boldsymbol{d}(\boldsymbol{r}')\;\mathrm{d}\sigma(\boldsymbol{r}'), \tag{5.13c}$$

which are defined on the boundary $\boldsymbol{r} \in \Gamma$. Along with these tangential operators, we will also need the operators

$$\mathrm{S}^s[\varphi](\boldsymbol{r}) = \int_\Gamma G(\boldsymbol{r}, \boldsymbol{r}')\varphi(\boldsymbol{r}') \, \mathrm{d}\sigma(\boldsymbol{r}'), \tag{5.14a}$$

$$\overrightarrow{\mathrm{S}}[\boldsymbol{d}](\boldsymbol{r}) = \int_\Gamma G(\boldsymbol{r}, \boldsymbol{r}')\boldsymbol{d}(\boldsymbol{r}') \, \mathrm{d}\sigma(\boldsymbol{r}'), \tag{5.14b}$$

$$\overrightarrow{K}[\boldsymbol{d}](\boldsymbol{r}) = \int_\Gamma \frac{\partial G}{\partial \boldsymbol{n}(\boldsymbol{r})}(\boldsymbol{r}, \boldsymbol{r}')\boldsymbol{d}(\boldsymbol{r}') \, \mathrm{d}\sigma(\boldsymbol{r}'). \tag{5.14c}$$

5.2 Representation theorems

As stated above, the treatment of the three-dimensional time-harmonic Maxwell's equations by means of integral equations resembles the treatment for the acoustic scattering case. The main difference lies in the vectorial character of the electromagnetic fields—which makes the integral representations more complex. The representation formulas are central to this thesis, hence in what follows we present a summary of the necessary details [63, Theorem 5.5.1].

Denote Ω_i a bounded interior domain, Ω_e the complementary exterior domain, and Γ the boundary between the two domains, with $\boldsymbol{n}$ the normal unit vector pointing towards Ω_e. Consider also $\mathbf{E}$ and $\mathbf{H}$ to be solutions to Maxwell's equations, in both Ω_i and Ω_e with the *same* wavenumber k, where additionally, $\mathbf{E}$ and $\mathbf{H}$ satisfy the Silver-Müller radiation conditions [63] in the exterior domain. Define also the boundary tangential densities

$$\boldsymbol{j} = \mathbf{H}^- \times \boldsymbol{n} - \mathbf{H}^+ \times \boldsymbol{n}, \tag{5.15a}$$

$$\boldsymbol{m} = \mathbf{E}^- \times \boldsymbol{n} - \mathbf{E}^+ \times \boldsymbol{n}, \tag{5.15b}$$

where

$$\begin{cases} \mathbf{E}^\pm(\boldsymbol{r}) = \lim\limits_{\delta \to 0} \mathbf{E}(\boldsymbol{r} + \delta \boldsymbol{n}(\boldsymbol{r})), \\ \mathbf{H}^\pm(\boldsymbol{r}) = \lim\limits_{\delta \to 0} \mathbf{H}(\boldsymbol{r} + \delta \boldsymbol{n}(\boldsymbol{r})), \end{cases} \qquad \boldsymbol{r} \in \Gamma. \tag{5.16}$$

The densities $\boldsymbol{j}$ and $\boldsymbol{m}$ are known as the electric and magnetic currents, respectively.

Then, the electromagnetic fields admit the following representation formula for both the interior and exterior domains:

$$\mathbf{E}(\boldsymbol{r}) = i\omega\mu\mathscr{S}[\boldsymbol{j}](\boldsymbol{r}) + \frac{i}{\omega\varepsilon}\mathscr{K}[\boldsymbol{j}](\boldsymbol{r}) + \mathscr{D}[\boldsymbol{m}](\boldsymbol{r}), \qquad \boldsymbol{r} \notin \Gamma, \tag{5.17a}$$

$$\mathbf{H}(\boldsymbol{r}) = -i\omega\varepsilon\mathscr{S}[\boldsymbol{m}](\boldsymbol{r}) - \frac{i}{\omega\mu}\mathscr{K}[\boldsymbol{m}](\boldsymbol{r}) + \mathscr{D}[\boldsymbol{j}](\boldsymbol{r}), \qquad \boldsymbol{r} \notin \Gamma. \tag{5.17b}$$

Moreover, the interior and exterior values of the tangential components of the electromagnetic fields at the boundary ($\boldsymbol{r} \in \Gamma$) satisfy[1]

$$(\mathbf{E}^{\pm} \times \boldsymbol{n})(\boldsymbol{r}) = \mp \frac{\boldsymbol{m}(\boldsymbol{r})}{2} + \mathrm{R}[\boldsymbol{m}](\boldsymbol{r}) + i\omega\mu\, \mathrm{S}[\boldsymbol{j}](\boldsymbol{r}) + \frac{i}{\omega\varepsilon}\, \mathrm{T}[\boldsymbol{j}](\boldsymbol{r}), \tag{5.18a}$$

$$(\mathbf{H}^{\pm} \times \boldsymbol{n})(\boldsymbol{r}) = \mp \frac{\boldsymbol{j}(\boldsymbol{r})}{2} + \mathrm{R}[\boldsymbol{j}](\boldsymbol{r}) - i\omega\varepsilon\, \mathrm{S}[\boldsymbol{m}](\boldsymbol{r}) - \frac{i}{\omega\mu}\, \mathrm{T}[\boldsymbol{m}](\boldsymbol{r}). \tag{5.18b}$$

Remark 5.2.1 *In these representation formulas, the wavenumber is the same for both the interior and exterior, and the solutions inside and outside are independent from each other in the sense that, as long as one uses the definitions of the densities in equation* (5.15)*, the representation formula in equation* (5.17) *and limiting values in equation* (5.18) *hold.*

5.3 Dielectric integral equations

In this section, we present a derivation of the integral equations for a transmission problem defined in what follows. For conciseness, we limit the problem to two dielectric materials, one immersed in the other, occupying the interior and exterior regions Ω_i and Ω_e, respectively. Together with a wavelength λ_0 and the corresponding refractive indices n_i and n_e for the interior and exterior materials, we seek a solution of the scattering problem for incident electromagnetic fields $\mathbf{E}^{\mathrm{inc}}$ and $\mathbf{H}^{\mathrm{inc}}$ impinging on the obstacle. The total electromagnetic field—that is, the sum of the incident and the scattered field—satisfy the transmission boundary conditions.

As in the acoustic case, various kinds of integral formulations exist for the electromagnetic problem. In some cases, formulations are preferred which involve only weakly-singular kernels. This is one of the driving motivations leading to the Müller formulation [62, 80]. Throughout this thesis we use a *direct*[2] Müller formulation—such as the one presented in [63, section 5.6.3]. For the sake of clarity, we make the following assumptions:

- We only have two domains, each representing a linear homogeneous dielectric material: Ω_i bounded with a refractive index of n_i, and the associated exterior domain Ω_e with a refractive index of n_e.
- The incident fields $\mathbf{E}^{\mathrm{inc}}$ and $\mathbf{H}^{\mathrm{inc}}$ are non-zero only in the exterior domain.

[1] For the limiting expressions of the normal components of the fields, and a proof of the representation theorem, we refer the reader to [63, Chapter 5.5].

[2] A direct formulation is one that uses directly the representation formulas.

These two assumptions can easily be generalized to multiple domains and incident fields on every domain.

In order to find the total electromagnetic fields that satisfy the transmission boundary conditions (see equation (1.10)), we use two auxiliary formulations—one for each domain—directly from the representation theorem:

Formulation 1. Let k_i denote the interior wavenumber, and let $\mathbf{E}_i$ and $\mathbf{H}_i$ denote the scattered fields in Ω_i and choose the exterior field in this case to be zero everywhere in Ω_e. The representation formula in equation (5.17) yields

$$\boldsymbol{j}_i = \mathbf{H}_i \times \boldsymbol{n}, \tag{5.19a}$$

$$\boldsymbol{m}_i = \mathbf{E}_i \times \boldsymbol{n}, \tag{5.19b}$$

$$i\omega\mu_i \mathscr{S}_i[\boldsymbol{j}_i](\boldsymbol{r}) + \frac{i}{\omega\varepsilon_i}\mathscr{K}_i[\boldsymbol{j}_i](\boldsymbol{r}) + \mathscr{D}_i[\boldsymbol{m}_i](\boldsymbol{r}) = \begin{cases} \mathbf{E}_i(\boldsymbol{r}), & \boldsymbol{r} \in \Omega_i, \\ 0, & \boldsymbol{r} \notin \Omega_i, \end{cases} \tag{5.20a}$$

$$-i\omega\varepsilon_i \mathscr{S}_i[\boldsymbol{m}_i](\boldsymbol{r}) - \frac{i}{\omega\mu_i}\mathscr{K}_i[\boldsymbol{m}_i](\boldsymbol{r}) + \mathscr{D}_i[\boldsymbol{j}_i](\boldsymbol{r}) = \begin{cases} \mathbf{H}_i(\boldsymbol{r}), & \boldsymbol{r} \in \Omega_i, \\ 0, & \boldsymbol{r} \notin \Omega_i. \end{cases} \tag{5.20b}$$

Formulation 2. Let k_e denote the exterior wavenumber, and let $\mathbf{E}_e$ and $\mathbf{H}_e$ denote the scattered fields in Ω_e and choose the interior field in this case to be zero everywhere in Ω_i. In this case, the representation equation (5.17) becomes

$$\boldsymbol{j}_e = -\mathbf{H}_e \times \boldsymbol{n}, \tag{5.21a}$$

$$\boldsymbol{m}_e = -\mathbf{E}_e \times \boldsymbol{n}, \tag{5.21b}$$

$$i\omega\mu_e \mathscr{S}_e[\boldsymbol{j}_e](\boldsymbol{r}) + \frac{i}{\omega\varepsilon_e}\mathscr{K}_e[\boldsymbol{j}_e](\boldsymbol{r}) + \mathscr{D}_e[\boldsymbol{m}_e](\boldsymbol{r}) = \begin{cases} \mathbf{E}_e(\boldsymbol{r}), & \boldsymbol{r} \in \Omega_e, \\ 0, & \boldsymbol{r} \notin \Omega_e, \end{cases} \tag{5.22a}$$

$$-i\omega\varepsilon_e \mathscr{S}_e[\boldsymbol{m}_e](\boldsymbol{r}) - \frac{i}{\omega\mu_e}\mathscr{K}_e[\boldsymbol{m}_e](\boldsymbol{r}) + \mathscr{D}_e[\boldsymbol{j}_e](\boldsymbol{r}) = \begin{cases} \mathbf{H}_e(\boldsymbol{r}), & \boldsymbol{r} \in \Omega_e, \\ 0, & \boldsymbol{r} \notin \Omega_e. \end{cases} \tag{5.22b}$$

These two formulations can be linked by using the fact that the total electromagnetic fields are given by a sum of the incident and scattered fields:

$$\mathbf{E} = \begin{cases} \mathbf{E}_i & \text{in } \Omega_i, \\ \mathbf{E}_e + \mathbf{E}^{\text{inc}} & \text{in } \Omega_e, \end{cases} \tag{5.23a}$$

$$\mathbf{H} = \begin{cases} \mathbf{H}_i & \text{in } \Omega_i, \\ \mathbf{H}_e + \mathbf{H}^{\text{inc}} & \text{in } \Omega_e. \end{cases} \tag{5.23b}$$

For an interface along dielectric materials, the boundary conditions in equation (1.10) state that the tangential components of the fields must be continuous:

$$\mathbf{E}_i \times \boldsymbol{n} = \mathbf{E}_e \times \boldsymbol{n} + \mathbf{E}^{\text{inc}} \times \boldsymbol{n}, \tag{5.24a}$$

$$\mathbf{H}_i \times \boldsymbol{n} = \mathbf{H}_e \times \boldsymbol{n} + \mathbf{H}^{\text{inc}} \times \boldsymbol{n}, \tag{5.24b}$$

and by defining the incident densities

$$\boldsymbol{j}^{\text{inc}} = -\mathbf{H}^{\text{inc}} \times \boldsymbol{n}, \tag{5.25a}$$

$$\boldsymbol{m}^{\text{inc}} = -\mathbf{E}^{\text{inc}} \times \boldsymbol{n}, \tag{5.25b}$$

and the total densities

$$\boldsymbol{j} = \boldsymbol{j}_i, \tag{5.26a}$$

$$\boldsymbol{m} = \boldsymbol{m}_i, \tag{5.26b}$$

we have that the exterior densities can be written in terms of the total and incident densities:

$$\boldsymbol{j}_e = -(\boldsymbol{j} + \boldsymbol{j}^{\text{inc}}), \tag{5.27a}$$

$$\boldsymbol{m}_e = -(\boldsymbol{m} + \boldsymbol{m}^{\text{inc}}). \tag{5.27b}$$

Having used the boundary conditions to relate the interior and exterior densities, a first set of integral equations can be obtained as indicated as follows:

1. Evaluate the exterior electric field using equation (5.18). Multiply the result by $\omega\varepsilon_e$.

2. Evaluate the interior electric field using equation (5.18). Multiply the result by $\omega\varepsilon_i$.

3. Add the results from steps (1) and (2).

4. Use the definitions of the densities to simplify $\mathbf{E} \times \boldsymbol{n}$.

These steps yield the following vectorial integral equation:

$$\begin{aligned}\left(\frac{\omega\varepsilon_e + \omega\varepsilon_i}{2}\right)\boldsymbol{m}(\boldsymbol{r}) + \omega\left(\varepsilon_e \mathrm{R}_e - \varepsilon_i \mathrm{R}_i\right)[\boldsymbol{m}](\boldsymbol{r}) + i\left(k_e^2 \mathrm{S}_e - k_i^2 \mathrm{S}_i\right)[\boldsymbol{j}](\boldsymbol{r}) \\ + i\left(\mathrm{T}_e - \mathrm{T}_i\right)[\boldsymbol{j}](\boldsymbol{r}) = -\Bigg(\frac{\omega\varepsilon_e}{2}\boldsymbol{m}^{\mathrm{inc}}(\boldsymbol{r}) + \omega\varepsilon_e \mathrm{R}_e[\boldsymbol{m}^{\mathrm{inc}}](\boldsymbol{r}) \\ + ik_e^2 \mathrm{S}_e[\boldsymbol{j}^{\mathrm{inc}}](\boldsymbol{r}) + i\,\mathrm{T}_e[\boldsymbol{j}^{\mathrm{inc}}](\boldsymbol{r})\Bigg)\end{aligned} \tag{5.28}$$

where the subscript in the operators indicate the wavenumber to be used in the definitions in equation (5.13)—namely, e for k_e and i for k_i. Additionally, the right-hand side in equation (5.28) can be simplified by using a third auxiliary formulation involving the incident field.

Formulation 3. Define auxiliary fields to be such that they satisfy Maxwell's equations in Ω_i with wavenumber k_e (note that these are reversed), and in the interior they are the continuation of the incident fields. Then, these auxiliary fields satisfy the following representation formulas

$$i\omega\mu_i \mathscr{S}_i[\boldsymbol{j}^{\mathrm{inc}}](\boldsymbol{r}) + \frac{i}{\omega\varepsilon_i}\mathscr{K}_i[\boldsymbol{j}^{\mathrm{inc}}](\boldsymbol{r}) + \mathscr{D}_i[\boldsymbol{m}^{\mathrm{inc}}](\boldsymbol{r}) = \begin{cases} -\mathbf{E}^{\mathrm{inc}}(\boldsymbol{r}), & \boldsymbol{r} \in \Omega_i, \\ 0, & \boldsymbol{r} \notin \Omega_i, \end{cases} \tag{5.29a}$$

$$-i\omega\varepsilon_i \mathscr{S}_i[\boldsymbol{m}^{\mathrm{inc}}](\boldsymbol{r}) - \frac{i}{\omega\mu_i}\mathscr{K}_i[\boldsymbol{m}^{\mathrm{inc}}](\boldsymbol{r}) + \mathscr{D}_i[\boldsymbol{j}^{\mathrm{inc}}](\boldsymbol{r}) = \begin{cases} -\mathbf{H}^{\mathrm{inc}}(\boldsymbol{r}), & \boldsymbol{r} \in \Omega_i, \\ 0, & \boldsymbol{r} \notin \Omega_i, \end{cases} \tag{5.29b}$$

where the negative sign in the right-hand side comes from the opposite signs from the definition of the incident densities. Evaluating the electric field on the exterior side, we obtain the relation

$$0 = -\frac{\boldsymbol{m}^{\mathrm{inc}}}{2} + \mathrm{R}_e[\boldsymbol{m}^{\mathrm{inc}}] + i\omega\mu_e \mathrm{S}_e[\boldsymbol{j}^{\mathrm{inc}}] + \frac{i}{\omega\varepsilon_e}\mathrm{T}_e[\boldsymbol{j}^{\mathrm{inc}}] \tag{5.30}$$

which simplifies equation (5.28) to

$$\begin{aligned}\left(\frac{\omega\varepsilon_e + \omega\varepsilon_i}{2}\right)\boldsymbol{m}(\boldsymbol{r}) + \omega\left(\varepsilon_e \mathrm{R}_e - \varepsilon_i \mathrm{R}_i\right)[\boldsymbol{m}](\boldsymbol{r}) + i\left(k_e^2 \mathrm{S}_e - k_i^2 \mathrm{S}_i\right)[\boldsymbol{j}](\boldsymbol{r}) \\ + i\left(\mathrm{T}_e - \mathrm{T}_i\right)[\boldsymbol{j}](\boldsymbol{r}) = \omega\varepsilon_e\, \mathbf{E}^{\mathrm{inc}} \times \boldsymbol{n}.\end{aligned} \tag{5.31}$$

Using the same procedure for the **H** field, but multiplying by $\omega\mu$ instead of $\omega\varepsilon$, and defining

$$\mathrm{R}_\alpha^\Delta \equiv \frac{2}{\alpha_e + \alpha_i}\left(\alpha_e \mathrm{R}_e - \alpha_i \mathrm{R}_i\right), \tag{5.32a}$$

$$\mathrm{S}_\alpha^\Delta \equiv \frac{2i}{\omega(\alpha_e + \alpha_i)}\left(k_e^2 \mathrm{S}_e - k_i^2 \mathrm{S}_i\right), \tag{5.32b}$$

$$\mathrm{T}_\alpha^\Delta \equiv \frac{2i}{\omega(\alpha_e + \alpha_i)}\left(\mathrm{T}_e - \mathrm{T}_i\right), \tag{5.32c}$$

where the subindex α represents either the dielectric constant symbol, $\alpha = \varepsilon$, or the magnetic permeability symbol, $\alpha = \mu$, we arrive to the system of integral equations for the dielectric problem:

$$\boldsymbol{m}(\boldsymbol{r}) + \mathrm{R}_\varepsilon^\Delta[\boldsymbol{m}](\boldsymbol{r}) + \mathrm{S}_\varepsilon^\Delta[\boldsymbol{j}](\boldsymbol{r}) + \mathrm{T}_\varepsilon^\Delta[\boldsymbol{j}](\boldsymbol{r}) = \frac{2\varepsilon_e}{\varepsilon_e + \varepsilon_i}\mathbf{E}^{\mathrm{inc}} \times \boldsymbol{n}, \qquad \boldsymbol{r} \in \Gamma \tag{5.33a}$$

$$\boldsymbol{j}(\boldsymbol{r}) + \mathrm{R}_\mu^\Delta[\boldsymbol{j}](\boldsymbol{r}) - \mathrm{S}_\mu^\Delta[\boldsymbol{m}](\boldsymbol{r}) - \mathrm{T}_\mu^\Delta[\boldsymbol{m}](\boldsymbol{r}) = \frac{2\mu_e}{\mu_e + \mu_i}\mathbf{H}^{\mathrm{inc}} \times \boldsymbol{n}, \quad \boldsymbol{r} \in \Gamma. \tag{5.33b}$$

Remark 5.3.1 *The system of integral equations in equation* (5.33) *involves only weakly-singular kernels in view of the kernel cancellations that arise in the operator difference* $\mathrm{T}_\alpha^\Delta \propto \mathrm{T}_e - \mathrm{T}_i$.

5.4 Incident electromagnetic fields

Any solution to the time-harmonic Maxwell's equations can play the role of an incident field; in this section, we present well-known expressions that are often used to model external excitations in electromagnetic scattering. We divide them into three groups: (1) multipole solutions, (2) plane waves, and (3) electromagnetic beams.

5.4.1 Multipole solutions

Out of the multipole solutions, the best know solution is that of the electric dipole—which represents the fields produced by two charges, one positive and one negative, placed in very close proximity of each other. At the same time, Maxwell's equations allow for higher-order solutions of a similar type, and these multipole solutions can be classified into two different groups, namely, transverse electric and transverse magnetic multipoles.

In order to present these multipole solutions, we first introduce the spherical harmonics [63, p. 24]:

$$Y_\ell^m(\theta,\phi) = (-1)^m \left[\frac{(\ell+1/2)}{2\pi}\frac{(\ell-m)!}{(\ell+m)!}\right] e^{im\phi}\mathbb{P}_\ell^m(\cos\theta) \tag{5.34}$$

and the vector spherical harmonics [63, pp. 37-38]:

$$I_\ell^m(\boldsymbol{r}) = \nabla_S Y_{\ell+1}^m(\boldsymbol{r}) + (\ell+1)Y_{\ell+1}^m(\boldsymbol{r})\,\boldsymbol{r}, \tag{5.35}$$

$$T_\ell^m(\boldsymbol{r}) = \nabla_S Y_\ell^m(\boldsymbol{r}) \times \boldsymbol{r}, \tag{5.36}$$

$$N_\ell^m(\boldsymbol{r}) = -\nabla_S Y_{\ell-1}^m(\boldsymbol{r}) + \ell Y_{\ell-1}^m(\boldsymbol{r})\,\boldsymbol{r}. \tag{5.37}$$

Thereupon, the multipole solutions are given as follows.

Transverse electric multipole solutions [63, p. 186] and [32, p. 218][3]:

$$\mathbf{E}_\ell^m(\boldsymbol{r}) = h_\ell^{(1)}(kr)T_\ell^m(\theta,\phi), \tag{5.38a}$$

$$\mathbf{H}_\ell^m(\boldsymbol{r}) = -\frac{i}{\omega\mu}\nabla\times\mathbf{E}_\ell^m \tag{5.38b}$$

$$= -\frac{i\sqrt{\varepsilon/\mu}}{(2\ell+1)}\left[(\ell+1)h_{\ell-1}^{(1)}(kr)I_{\ell-1}^m(\theta,\phi) + \ell h_{\ell+1}^{(1)}(kr)N_{\ell+1}^m(\theta,\phi)\right], \tag{5.38c}$$

which satisfy $\mathbf{E}\cdot\boldsymbol{r} = 0$, hence the name.

Transverse magnetic multipole solutions [63, p. 186] and [32, p. 218]:

$$\mathbf{H}_\ell^m(\boldsymbol{r}) = h_\ell^{(1)}(kr)T_\ell^m(\theta,\phi), \tag{5.39a}$$

$$\mathbf{E}_\ell^m(\boldsymbol{r}) = \frac{i}{\omega\varepsilon}\nabla\times\mathbf{E}_\ell^m \tag{5.39b}$$

$$= \frac{i\sqrt{\mu/\varepsilon}}{(2\ell+1)}\left[(\ell+1)h_{\ell-1}^{(1)}(kr)I_{\ell-1}^m(\theta,\phi) + \ell h_{\ell+1}^{(1)}(kr)N_{\ell+1}^m(\theta,\phi)\right], \tag{5.39c}$$

which satisfy $\mathbf{H}\cdot\boldsymbol{r} = 0$.

Remark 5.4.1 *Both the transverse and magnetic multipole solutions satisfy the Silver-Müller radiation conditions. They also form a basis for the radiating solutions of Maxwell's equations—consequently, any solution on the exterior of a sphere that fully contains all the scatterers can be written in terms of a superposition of multipoles [63].*

[3] We use the definition of the spherical Hankel function given by Nedelec [63], in which $h_\ell^{(1)}(z) = -y_\ell(z) + i\; j_\ell(z)$.

5.4.2 Plane waves

Plane wave solutions model the behavior of the fields generated by sources that are located far away from the observation region. The electromagnetic plane wave fields are given by [63, p. 5]:

$$\begin{cases} \mathbf{E}^{\mathrm{pw}}(\boldsymbol{r}) = \mathbf{E}_0 e^{i\boldsymbol{k}\cdot\boldsymbol{r}}, \\ \mathbf{H}^{\mathrm{pw}}(\boldsymbol{r}) = \mathbf{H}_0 e^{i\boldsymbol{k}\cdot\boldsymbol{r}}, \end{cases} \tag{5.40}$$

where $\mathbf{E}_0$ and $\mathbf{H}_0$ are constant (complex-valued) vectors, $\boldsymbol{k}$ is the wavevector, and where, in view of Maxwell's equations, the following relations must be satisfied:

$$\begin{cases} \omega\varepsilon\mathbf{E}_0 + \boldsymbol{k} \times \mathbf{H}_0 = 0, \\ -\omega\mu\mathbf{H}_0 + \boldsymbol{k} \times \mathbf{E}_0 = 0. \end{cases} \tag{5.41}$$

Remark 5.4.2 *The direction of the wavevector $\boldsymbol{k}$ can be freely chosen, and the polarization $\mathbf{E}_0$ can then be specified as any constant vector orthogonal to $\boldsymbol{k}$. Because of equation* (5.41)*, $\mathbf{H}_0$ can be expressed in terms of $\boldsymbol{k}$ and $\mathbf{E}_0$. If $\mathbf{E}_0$ is a real vector, or a multiple of a real vector times a complex number, then the plane wave is said to be "linearly polarized". Otherwise, circular or, more generally, elliptical polarization, takes place [63].*

5.4.3 Electromagnetic beams

While plane waves provide a good representation of fields from far away sources, in many applications—such as in photonics—other types of incident excitations, such as optical beams, need to be considered. In optical applications, incident beams obtained by means of the paraxial approximation and resulting Gaussian beams are often used. Yet, it may be desirable to utilize incident fields that fully satisfy Maxwell's equations, such as the vector electromagnetic beam of the form [25] (or suitable rotations thereof):

$$E_x(\boldsymbol{r}) = \int_{-\infty}^{\infty}\int_{-\infty}^{\infty} A_x(k_x, k_y) \exp\left[ik\left(k_x x_1 + k_y x_2 + k_z z\right)\right] \mathrm{d}k_x \mathrm{d}k_y, \tag{5.42a}$$

$$E_y(\boldsymbol{r}) = \int_{-\infty}^{\infty}\int_{-\infty}^{\infty} A_y(k_x, k_y) \exp\left[ik\left(k_x x_1 + k_y x_2 + k_z z\right)\right] \mathrm{d}k_x \mathrm{d}k_y, \tag{5.42b}$$

$$E_z(\boldsymbol{r}) = -\int_{-\infty}^{\infty}\int_{-\infty}^{\infty} \left[\frac{k_x}{k_z} A_x(k_x, k_y) + \frac{k_y}{k_z} A_y(k_x, k_y)\right] \times \exp\left[ik\left(k_x x_1 + k_y x_2 + k_z z\right)\right] \mathrm{d}k_x \mathrm{d}k_y, \tag{5.42c}$$

where A_x and A_y are the (arbitrarily prescribable) angular spectra for the $x-$ and $y-$components of the $\mathbf{E}-$field; the $z-$component of the wave vector is then given by

$$k_z = \begin{cases} \sqrt{1 - k_x^2 - k_y^2}, & \text{if } k_x^2 + k_y^2 \leq 1, \\ \text{sign}(z) i \sqrt{k_x^2 + k_y^2 - 1}, & \text{if } k_x^2 + k_y^2 > 1, \end{cases} \tag{5.43}$$

where the wavenumber value has been chosen to yield evanescent waves—instead of waves that grow exponentially at infinity.

Equation (5.42) yields great generality, as it represents an infinite superposition of plane waves. In a more concrete setting, given an initial profile for the transverse fields E_x and E_y, the amplitudes A_x and A_y can be found by means of an inverse Fourier transform. In the particular case of the fields at the $z = 0$ plane given by a Gaussian profile

$$E_x(x_1, x_2, 0) = \exp\left(-\frac{x_1^2 + x_2^2}{2\omega_0^2}\right), \tag{5.44}$$

$$E_y(x_1, x_2, 0) = 0, \tag{5.45}$$

which correspond to a linearly polarized Gaussian profile at the $z = 0$ plane, we get [25]:

$$A_x(k_x, k_y) = \frac{1}{2\pi f^2} \exp\left(-\frac{k_x^2 + k_y^2}{2f^2}\right), \tag{5.46}$$

$$A_y(k_x, k_y) = 0, \tag{5.47}$$

where $f = (k\omega_0)^{-1}$. Then, the $x-$component of the electric field is

$$E_x(\boldsymbol{r}) = \int_0^\infty \frac{1}{f^2} \exp\left(-\frac{b^2}{2f^2}\right) \exp\left(ikk_z x_3\right) J_0\left(kb\sqrt{x_1^2 + x_2^2}\right) \, b \, \mathrm{d}b \tag{5.48}$$

where $b = \sqrt{k_x^2 + k_y^2}$, and the $y-$ and $z-$components of the electric field can be found from equation (5.42)—in particular $E_y = 0$ everywhere.

5.5 Rectangular-polar electromagnetic solver

Now that we have obtained a system of boundary integral equations for the electromagnetic problems, we can proceed to extend the rectangular-polar method—introduced in Chapter 4—to the present electromagnetic context. The most direct approach to obtain such an implementation would be to apply the scalar rectangular-polar method presented in Chapter 4 to each component of the electromagnetic

vectorial integral equation (5.33). Using this procedure, however, one would incur a larger number of precomputations than is strictly necessary. In detail, the simple-minded approach would require precomputed applications of the following operators to the relevant set of products of Chebyshev polynomials:

- T_μ^Δ, $\mathrm{T}_\varepsilon^\Delta$ and R_μ^Δ, $\mathrm{R}_\varepsilon^\Delta$. (These operators require six precomputations in total per Chebyshev product, which arise from the scalar components of the kernels $\nabla_{\boldsymbol{r}} G_e(\boldsymbol{r}, \boldsymbol{r}')$ and $\nabla_{\boldsymbol{r}} G_i(\boldsymbol{r}, \boldsymbol{r}')$. Note that for R_α^Δ, we can use the vector calculus identity $\nabla_{\boldsymbol{r}} \times [G(\boldsymbol{r}, \boldsymbol{r}')\boldsymbol{d}(\boldsymbol{r}')] = [\nabla_{\boldsymbol{r}} G(\boldsymbol{r}, \boldsymbol{r}')] \times \boldsymbol{d}(\boldsymbol{r}')$.)
- S_μ^Δ and $\mathrm{S}_\varepsilon^\Delta$. (One component that comes from the kernel $k_e^2 G_e(\boldsymbol{r}, \boldsymbol{r}') - k_i^2 G_i(\boldsymbol{r}, \boldsymbol{r}')$.)

This approach thus requires a total of seven operator precomputations per Chebyshev product. As shown in what follows, however, the operators can be manipulated into a form that requires only four sets of precomputations.

To do this, we re-express the T operator by using the following identity for a scalar function $f(u, v)$ defined over Γ:

$$\begin{aligned} -\boldsymbol{n}(\boldsymbol{r}) \times \nabla f(\boldsymbol{r}) &= -\alpha(\boldsymbol{r}) \left[\boldsymbol{e}_1(\boldsymbol{r}) \times \boldsymbol{e}_2(\boldsymbol{r})\right] \times \nabla f(\boldsymbol{r}) \\ &= \alpha(\boldsymbol{r}) \times \nabla f(\boldsymbol{r}) \times \left[\boldsymbol{e}_1(\boldsymbol{r}) \times \boldsymbol{e}_2(\boldsymbol{r})\right] \\ &= \alpha(\boldsymbol{r}) \left[(\boldsymbol{e}_2(\boldsymbol{r}) \cdot \nabla f(\boldsymbol{r}))\boldsymbol{e}_1 - (\boldsymbol{e}_1(\boldsymbol{r}) \cdot \nabla f(\boldsymbol{r}))\boldsymbol{e}_2\right] \\ &= \alpha(\boldsymbol{r}) \left[\frac{\partial f(\boldsymbol{r})}{\partial v} \boldsymbol{e}_1(\boldsymbol{r}) - \frac{\partial f(\boldsymbol{r})}{\partial u} \boldsymbol{e}_2(\boldsymbol{r})\right], \end{aligned} \tag{5.49}$$

where α is as defined in equation (5.3). Then, if we let $f(u, v)$ denote the integral after the gradient in equation (5.13c), we obtain

$$\mathrm{T}[\boldsymbol{d}](\boldsymbol{r}) = \alpha(\boldsymbol{r}) \left(\boldsymbol{e}_1(\boldsymbol{r}) \frac{\partial}{\partial v} - \boldsymbol{e}_2(\boldsymbol{r}) \frac{\partial}{\partial u}\right) (\mathrm{S}^s[\mathrm{div}_\Gamma \boldsymbol{d}](\boldsymbol{r})), \quad \boldsymbol{r} \in \Gamma, \tag{5.50}$$

which only requires precomputations for the single-layer operator, since all other operations in this expression can efficiently be obtained whenever needed.

Next, we turn our attention to the R operator. For shorthand, we denote

$$f(\boldsymbol{r}(u, v)) \equiv \int_\Gamma G(\boldsymbol{r}(u, v), \boldsymbol{r}')\boldsymbol{d}(\boldsymbol{r}') \, \mathrm{d}\sigma(\boldsymbol{r}'). \tag{5.51}$$

Then, we can re-express the R operator in the form

$$\mathrm{R}[\boldsymbol{d}](\boldsymbol{r}) = (\boldsymbol{n}(\boldsymbol{r}) \cdot \nabla) f(\boldsymbol{r}) - \nabla^{\boldsymbol{n}} \left[\boldsymbol{n}(\boldsymbol{r}) \cdot f(\boldsymbol{r})\right], \tag{5.52}$$

where we used the Feynman notation $\nabla^{\boldsymbol{n}}$, which indicates that the differentiation takes $\boldsymbol{n}$ as constant. Now, by using the decomposition of the gradient into the tangent and normal planes:

$$\nabla g = \frac{\partial g}{\partial \xi_1}\boldsymbol{e}^1 + \frac{\partial g}{\partial \xi_2}\boldsymbol{e}^2 + \frac{\partial g}{\partial \boldsymbol{n}}\boldsymbol{n}, \tag{5.53}$$

we get

$$\begin{aligned}\mathrm{R}[\boldsymbol{d}](\boldsymbol{r}) =& \overrightarrow{K}[\boldsymbol{d}](\boldsymbol{r}) - \left[\boldsymbol{n}(\boldsymbol{r}) \cdot \overrightarrow{K}[\boldsymbol{d}](\boldsymbol{r})\right] \boldsymbol{n}(\boldsymbol{r}) - \left(\boldsymbol{e}^1(\boldsymbol{r}) \left[\boldsymbol{n}(\boldsymbol{r}) \cdot \frac{\partial}{\partial u}\right]\right. \\ &\left. + \boldsymbol{e}^2(\boldsymbol{r}) \left[\boldsymbol{n}(\boldsymbol{r}) \cdot \frac{\partial}{\partial v}\right]\right) \left(\overrightarrow{\mathrm{S}}[\boldsymbol{d}](\boldsymbol{r})\right), \quad \boldsymbol{r} \in \Gamma. \end{aligned} \tag{5.54}$$

In the context of the rectangular-polar integration method, the expression in equation (5.54) only requires two sets of precomputations—one for the single-layer and another for the normal derivative of the single-layer.

Finally, the S operator is given by

$$\mathrm{S}[\boldsymbol{d}](\boldsymbol{r}) = -\boldsymbol{n}(\boldsymbol{r}) \times \overrightarrow{\mathrm{S}}[\boldsymbol{d}](\boldsymbol{r}), \quad \boldsymbol{r} \in \Gamma, \tag{5.55}$$

which only requires precomputations for the single-layer potential.

Using these alternative expressions for the operators, we have the following count for the sets of precomputations in equation (5.33) within the rectangular-polar paradigm:

- $\overrightarrow{\mathrm{S}}_e$ and $\overrightarrow{\mathrm{S}}_i$: Two precomputations.
- $\overrightarrow{K}_e$ and $\overrightarrow{K}_i$: Two precomputations.

This leaves us with a total of four sets of precomputations—saving up a factor of $3/7$ in computing time and storage in comparison to the direct approach.

Putting it all together, the solution to the dielectric system in equation (5.33) using the rectangular-polar method is summarized in Algorithms 5.1 and 5.2. In particular, Algorithm 5.1 presents a high-level description of the solver, which is an almost straightforward application of the iterative solver GMRES. On the other hand, Algorithm 5.2 presents the steps needed to perform one forward map (the action) of the right-hand side in equation (5.33), which is needed for the GMRES solver. Once the electromagnetic densities are found, the total fields can be computed using the representation formulas in equations (5.20) and (5.22).

Algorithm 5.1 High-level description of the dielectric rectangular-polar solver.

procedure ELECTROMAGNETIC SOLVER(Geometry, Incident Fields)
    Discretize geometry
    ▷ Precomputations
    for $q = 1, \ldots, M$ **do** → For all patches
        Determine which points are close to patch q and precompute singular and near-singular weights for the single-layer and its derivative with both wavenumbers k_e and k_i.
    end for
    Use GMRES to solve equation (5.33), where the action of the operator is given by the procedure `Forward Map` in Algorithm 5.2
    return Solution densities
end procedure

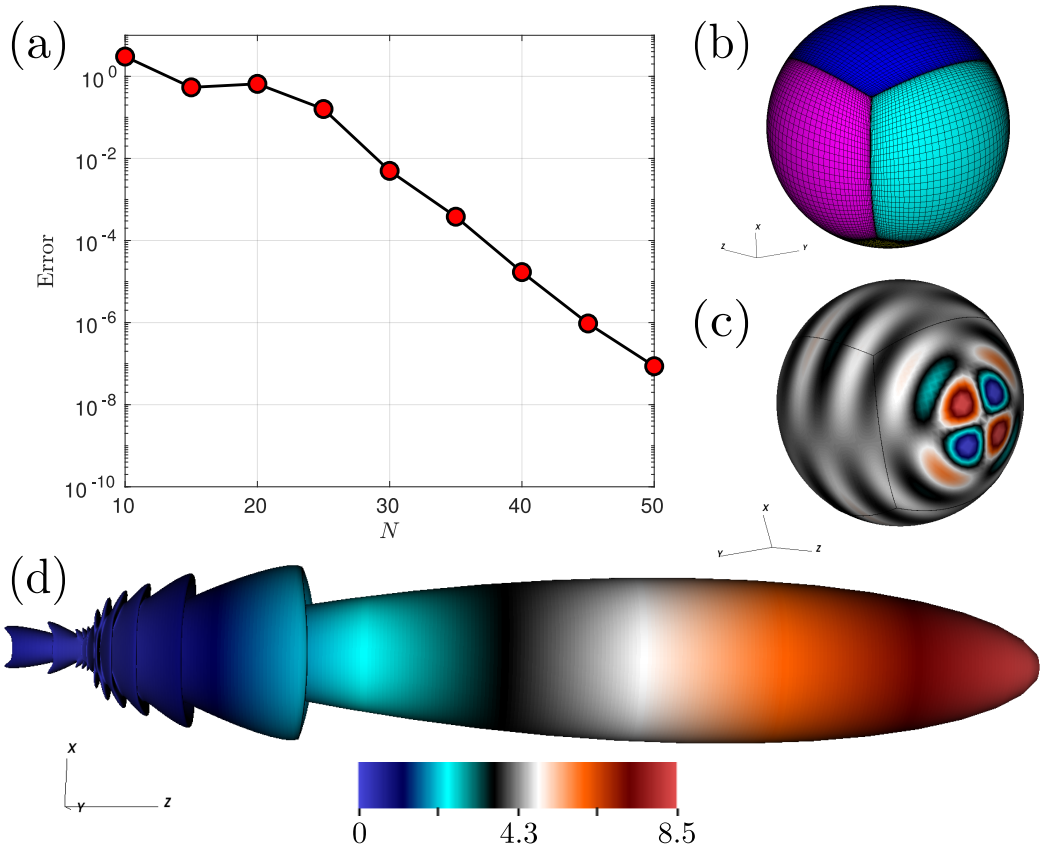

Figure 5.1: Scattering by a dielectric sphere of radius $2\lambda_0$. The convergence in the far field is shown in (a). On the other hand, (b) and (c) show the discretization and resulting density solution (one component) from the 50×50 discretization that gives an error of order 10^{-8}. The far field pattern for this problem is shown in (d).

Algorithm 5.2 Algorithmic steps to compute one forward map of the electromagnetic integral operators.

procedure FORWARD MAP($\widetilde{\boldsymbol{m}}, \widetilde{\boldsymbol{j}}$)
  $\widetilde{\boldsymbol{m}}, \widetilde{\boldsymbol{j}}$: Input densities
  Denote the set of operators:
    $Q = \{ \overrightarrow{\mathrm{S}}_{e,i}[\widetilde{\boldsymbol{m}}], \overrightarrow{\mathrm{S}}_{e,i}[\widetilde{\boldsymbol{j}}], \overrightarrow{K}_{e,i}[\widetilde{\boldsymbol{m}}], \overrightarrow{K}_{e,i}[\widetilde{\boldsymbol{j}}], \mathrm{S}^s_{e,i}[\mathrm{div}_\Gamma \widetilde{\boldsymbol{m}}], \mathrm{S}^s_{e,i}[\mathrm{div}_\Gamma \widetilde{\boldsymbol{j}}] \}$
  Initialize elements in $Q \to 0$
▷ Compute Chebyshev transforms and surface divergences
  for $q = 1, \ldots, M$ **do** → For all patches
    Compute Chebyshev transforms of the Cartesian components of $\widetilde{\boldsymbol{m}}^q, \widetilde{\boldsymbol{j}}^q$
    Compute $\mathrm{div}_\Gamma \widetilde{\boldsymbol{m}}^q$ and it's Chebyshev transform
    Compute $\mathrm{div}_\Gamma \widetilde{\boldsymbol{j}}^q$ and it's Chebyshev transform
  end for
▷ Evaluate operators in Q
  for $q^{\mathrm{trg}} = 1, \ldots, M$ **do** → For all target patches
    for $(i, j) = 1, \ldots, N^q$ **do** → For all target points in patch
      for $q^{\mathrm{src}} = 1, \ldots, M$ **do** → For all source patches
        if Target point close to source patch **then** → Singular integration
          Use precomputations and Chebyshev transforms to add the contributions on each operator in Q
        else → Non-singular integration
          Add contributions using Fejér's quadrature
        end if
      end for
    end for
  end for
▷ Compute EM operators using the Q operators
  for $q = 1, \ldots, M$ **do** → For all patches
    Compute $\mathrm{R}^\Delta_\alpha, \mathrm{S}^\Delta_\alpha, \mathrm{T}^\Delta_\alpha$ from the operators in Q using equations (5.50), (5.54) and (5.55)
  end for
  return Evaluated left-hand side in equation (5.33)
end procedure

5.6 Implementation validation: Scattering by a sphere

The method described in this chapter will be the foundation for subsequent chapters, and thus this section presents only one numerical example to provide a verification of the implementation. Figure 5.1 demonstrates the convergence of the far field pattern scattered by a sphere of diameter $4\lambda_0$, with exterior and interior refractive indices 1 and 1.47, respectively, under plane-wave illumination. For reference, the Mie solution was used; we can see that, as long as the precomputations

are accurate enough, the convergence is super-algebraically fast with respect to the discretization of the geometry.

Chapter 6

WINDOWED GREEN FUNCTION METHOD FOR 3D WAVEGUIDES

As mentioned in Chapter 2, the use of boundary integral equations for scattering problems with unbounded obstacles has previously been somewhat limited given the edge-errors that arise from direct truncation of an infinite surface. Some efforts towards tackling this difficulty have been studied in different contexts. Notably, in [37] it is shown that for the two-dimensional Helmholtz equation, boundary integral representations exist for unbounded obstacles. For the problem considered in this chapter – scattering by three-dimensional waveguides—a boundary element methodology based on conductive absorbers was developed in [81] which, however, does not address the important case of direct mode excitation—only point sources and Gaussian beams are considered in this paper—and which demonstrates the absorption properties of the method, but it does not present any estimates of the method's accuracy.

Recent progress in windowing techniques have established that boundary integral equations can be efficiently used to accurately solve a wide range of scattering problems that involve unbounded obstacles. For instance, in [13, 55, 61] windowing is used to model scattering by rough surfaces. Scattering by arrays using the quasi-periodic Green function together with the window function was presented in [21, 23], while in [14] the problem of scattering by arrays of cylinders is solved using the shifted Green function method in conjunction with windowing. Markedly, in [18, 20, 68] the windowed Green function (WGF) method was introduced for the problem of layer-media scattering in both two- and three-dimensional spaces, demonstrating improvements in several orders of magnitude for the computing times against competing methods. In [22] (see also Chapter 2), the WGF method was adapted for two-dimensional waveguides, including the notoriously problematic case of exact mode excitation. Interestingly, the WGF method can be used in conjunction with any kind of integral-equation solution methodology—e.g. Nyström, collocation and Galerkin, all work within the WGF paradigm—and, as shown in this chapter, the method effectively generalizes to the three-dimensional case.

This chapter presents a three-dimensional implementation of the WGF method

for dielectric waveguides by generalizing the two-dimensional methodologies introduced in Chapter 2. Even though the development of the three-dimensional WGF method presents significant implementation challenges, there is a three-dimensional correspondence for every key component of the two-dimensional algorithm. Importantly, as in the two-dimensional case, the kernels of the three-dimensional EM integral equations display the slowly-decaying oscillatory asymptotics from which the windowing approach derives its accuracy and super-algebraic convergence as the window size increases.

Throughout this chapter, we present two different types of waveguide excitations, namely:

1. **Beam illumination**: In this case an optical beam is used to illuminate the waveguide structure. The illuminating beam is taken to be a Gaussian in this chapter, but beams of other types can be used as well; see section 5.4.3.

2. **Mode illumination**: Under mode illumination, a propagating mode from a semi-infinite waveguide (SIW) impinges upon a nonuniformity in the waveguide structure—such as a bend, taper, split, termination, etc.

For the sake of simplicity, we require all the wavevectors of the plane wave expansion of illuminating beams to have a non-negative dot product with the optical waveguide axis—a natural assumption in the present waveguide context. The occurrence of negative dot products could give rise to vanishing oscillations which would affect the overall convergence if left untreated. (Such vanishing oscillations could nevertheless be treated by means of an approach similar to the one used in [18, 20, 68] for layered media.)

6.1 Radiation conditions for 3D EM waveguides

As mentioned in Chapter 5, the scattered fields for the bounded-obstacle dielectric transmission problem decay at infinity in accordance with the Silver-Müller radiation conditions. As in the two-dimensional *waveguide* case, a revised radiation condition applies to three-dimensional dielectric waveguides [67, equation 36]—which allows for energy to propagate inside the waveguide without decay, and which, more precisely, states that the fields behave as a sum of two components: (1) a field that decays as $1/R$, where R is the distance to the inhomogeneity, and (2) a superposition of outgoing bound modes.

When solving bounded-obstacle scattering problems via integral equations, the radiation condition is built into the kernels themselves, so that, provided correct kernels are used, the Silver-Müller radiation condition is automatically enforced. For the waveguide problem, in contrast, we must account for the fact that bound modes can appear in both the incident and scattered fields. These modes admit an integral representation over the infinite boundaries, and thus they require special treatment when formulating the waveguide integral equations.

6.2 Window function for 3D SIWs

As in the two-dimensional problem considered in Chapter 2, we make use of semi-infinite waveguides (SIWs) as a main building block for general nonuniform problems. The SIW are structures with a defined optical axis, and whose transverse shape—with respect to the optical axis—remains invariant. On the other hand, the nonuniformities can be either junctions or terminations of arbitrary shape between SIWs.

The window function used in the present context is analogous to the one used in the two-dimensional problem. As in that case, for a point $\boldsymbol{r} \in \Gamma$ we let $d(\boldsymbol{r})$ denote an auxiliary function whose definition depends on whether or not $\boldsymbol{r}$ is an element of one of the underlying SIWs. If $\boldsymbol{r}$ is not an element of any of the SIWs, then $d(\boldsymbol{r}) = 0$, and if $\boldsymbol{r}$ is an element of one of the SIWs, then $d(\boldsymbol{r})$ equals the distance from $\boldsymbol{r}$ to the edge of that SIW.

A suitable choice for the window function is given by:

$$w_A(\boldsymbol{r}) = \begin{cases} 1, & s < 0 \\ \exp\left(-2\dfrac{\exp\left(-1/|s|^2\right)}{|1-s|^2} \right), & 0 \le s \le 1\,, \\ 0, & s > 1 \end{cases} \tag{6.1}$$

where $s(\boldsymbol{r}) = \frac{|d(\boldsymbol{r})|-\alpha A}{A(1-\alpha)}$. Additionally, since the electromagnetic operators involve vectorial densities, we also utilize the matrix-valued window function given by

$$W_A(\boldsymbol{r}) = \begin{bmatrix} w_A(\boldsymbol{r}) & 0 & 0 \\ 0 & w_A(\boldsymbol{r}) & 0 \\ 0 & 0 & w_A(\boldsymbol{r}) \end{bmatrix}. \tag{6.2}$$

6.3 Beam illumination

We now turn our attention to the specific case of beam illumination. Given the non-negative dot product condition imposed on the beam in the introduction to the

present chapter, the dielectric formulation derived in Chapter 5 can be used for this problem. When combined with the windowing function described in Section 6.2 the following three-dimensional windowed integral equations result:

$$\boldsymbol{m}(\boldsymbol{r}) + \mathrm{R}_{\varepsilon}^{\Delta}[W_A\boldsymbol{m}](\boldsymbol{r}) + \mathrm{S}_{\alpha}^{\Delta}[W_A\boldsymbol{j}](\boldsymbol{r}) + \mathrm{T}_{\alpha}^{\Delta}[W_A\boldsymbol{j}](\boldsymbol{r}) = \frac{2\varepsilon_e}{\varepsilon_e+\varepsilon_i}\mathbf{E}^{\mathrm{inc}}\times\boldsymbol{n}, \tag{6.3a}$$

$$\boldsymbol{j}(\boldsymbol{r}) + \mathrm{R}_{\mu}^{\Delta}[W_A\boldsymbol{j}](\boldsymbol{r}) - \mathrm{S}_{\alpha}^{\Delta}[W_A\boldsymbol{m}](\boldsymbol{r}) - \mathrm{T}_{\alpha}^{\Delta}[W_A\boldsymbol{m}](\boldsymbol{r}) = \frac{2\mu_e}{\mu_e+\mu_i}\mathbf{H}^{\mathrm{inc}}\times\boldsymbol{n}, \tag{6.3b}$$

for $\boldsymbol{r}\in\Gamma$.

In order for the system (6.3) to provide a good approximation in the vicinity of the windowed region, it is necessary for the integrands in these operators to have non-vanishing oscillations as $d(\boldsymbol{r})\to\infty$. Remark 6.3.1 addresses this important point.

Remark 6.3.1 *In view of the definitions of the densities $\boldsymbol{j}$ and $\boldsymbol{m}$ in terms of the interior scattered fields, together with the radiation conditions, the densities behave asymptotically as the tangential components of a superposition of outgoing bound modes. The m-th mode contribution contains a factor of $e^{+ik_z^m|z|}$ (where k_z^m denotes the propagation constant of the m-th mode). Since the kernels oscillate with a factor of $e^{+ik|\boldsymbol{r}-\boldsymbol{r}'|}$, and since both k_z^m and k are positive, the product of the kernels and the densities result in non-vanishing oscillations as $d(\boldsymbol{r})\to\infty$.*

6.4 Mode illumination

In many instances, illuminating a waveguide with an incoming bound mode is desirable—this can model incoming fields from other structures that are connected through a waveguide. Historically, the sourcing of bound modes has been a non-straightforward matter, and alternative approximations are usually used—such as mode bootstrapping, illumination by Gaussian beams that approximate the mode, or by exciting the modes with point sources [76, 81]. These techniques usually require either additional simulations or large propagation distances for the incoming waves to shed away the undesired radiative or modal components, or the simulation is restricted to single-mode waveguides to avoid spurious modes being excited. However, it is highly advantageous to be able to directly source *any* mode at will, incurring into as little extra computation work and error as possible. With this goal in mind, this section proposes an integral equation methodology to accurately simulate the scattering of incident bound modes. In particular, we can use as incident field any given bound mode of the relevant waveguides—on the basis of an auxiliary

representation for the incident fields which, at minimal expense, incur errors that are exponentially smaller with regards to a certain approximation parameter.

To describe the proposed incident-mode approach, let us consider a three-dimensional nonuniform waveguide structure composed of one or more SIWs. For clarity, we consider the case in which there is only one exterior and one interior domain, denoted as usual by Ω_e and Ω_i, respectively. Let one of the SIW carry an incoming bound mode as an incident excitation. The region Ω^{inc} wherein the incoming mode is defined coincides with the SIW itself—including both the core and cladding region. Thus, using the associated indicator function

$$\chi^{\text{inc}}(\boldsymbol{r}) = \begin{cases} 1 & \text{for } \boldsymbol{r} \in \Omega^{\text{inc}}, \\ 0 & \text{for } \boldsymbol{r} \notin \Omega^{\text{inc}}, \end{cases} \tag{6.4}$$

the total fields are given by $\mathbf{E} = \mathbf{E}^{\text{inc}}\chi^{\text{inc}} + \mathbf{E}^{\text{scat}}$ and $\mathbf{H} = \mathbf{H}^{\text{inc}}\chi^{\text{inc}} + \mathbf{H}^{\text{scat}}$. Next, define the interior incident and scattered densities

$$\boldsymbol{m}^{\text{inc}} \equiv \boldsymbol{m}_i^{\text{inc}} = \chi^{\text{inc}}\mathbf{E}_i^{\text{inc}} \times \boldsymbol{n}, \tag{6.5a}$$

$$\boldsymbol{j}^{\text{inc}} \equiv \boldsymbol{j}_i^{\text{inc}} = \chi^{\text{inc}}\mathbf{H}_i^{\text{inc}} \times \boldsymbol{n}, \tag{6.5b}$$

$$\boldsymbol{m}^{\text{scat}} \equiv \boldsymbol{m}_i^{\text{scat}} = \mathbf{E}_i^{\text{scat}} \times \boldsymbol{n}, \tag{6.5c}$$

$$\boldsymbol{j}^{\text{scat}} \equiv \boldsymbol{j}_i^{\text{scat}} = \mathbf{H}_i^{\text{scat}} \times \boldsymbol{n}, \tag{6.5d}$$

and the exterior incident and scattered densities

$$\boldsymbol{m}_e^{\text{inc}} = -\chi^{\text{inc}}\mathbf{E}_e^{\text{inc}} \times \boldsymbol{n}, \tag{6.6a}$$

$$\boldsymbol{j}_e^{\text{inc}} = -\chi^{\text{inc}}\mathbf{H}_e^{\text{inc}} \times \boldsymbol{n}, \tag{6.6b}$$

$$\boldsymbol{m}_e^{\text{scat}} = -\mathbf{E}_e^{\text{scat}} \times \boldsymbol{n}, \tag{6.6c}$$

$$\boldsymbol{j}_e^{\text{scat}} = -\mathbf{H}_e^{\text{scat}} \times \boldsymbol{n}, \tag{6.6d}$$

respectively. Additionally, given the necessary continuity of the tangential components of the field induced by the boundary conditions, we obtain that the relations

$$\boldsymbol{m}_e^{\text{inc}} = -\boldsymbol{m}_i^{\text{inc}}, \tag{6.7a}$$

$$\boldsymbol{j}_e^{\text{inc}} = -\boldsymbol{j}_i^{\text{inc}}, \tag{6.7b}$$

$$\boldsymbol{m}_e^{\text{scat}} = -\boldsymbol{m}_i^{\text{scat}}, \tag{6.7c}$$

$$\boldsymbol{j}_e^{\text{scat}} = -\boldsymbol{j}_i^{\text{scat}}, \tag{6.7d}$$

hold.

Using these definitions and the representation formulas[1] presented in Chapter 5, we obtain the representation for the *total* fields:

$$i\omega\mu_i \mathscr{S}_i[\boldsymbol{j}_i^{\text{inc}} + \boldsymbol{j}_i^{\text{scat}}](\boldsymbol{r}) + \frac{i}{\omega\varepsilon_i}\mathscr{K}_i[\boldsymbol{j}_i^{\text{inc}} + \boldsymbol{j}_i^{\text{scat}}](\boldsymbol{r}) + \mathscr{D}_i[\boldsymbol{m}_i^{\text{inc}} + \boldsymbol{m}_i^{\text{scat}}](\boldsymbol{r}) = \begin{cases} \mathbf{E}_i(\boldsymbol{r}), & \boldsymbol{r} \in \Omega_i, \\ 0, & \boldsymbol{r} \notin \Omega_i, \end{cases} \tag{6.8a}$$

$$-i\omega\varepsilon_i \mathscr{S}_i[\boldsymbol{m}_i^{\text{inc}} + \boldsymbol{m}_i^{\text{scat}}](\boldsymbol{r}) - \frac{i}{\omega\mu_i}\mathscr{K}_i[\boldsymbol{m}_i^{\text{inc}} + \boldsymbol{m}_i^{\text{scat}}](\boldsymbol{r}) + \mathscr{D}_i[\boldsymbol{j}_i^{\text{inc}} + \boldsymbol{j}_i^{\text{scat}}](\boldsymbol{r}) = \begin{cases} \mathbf{H}_i(\boldsymbol{r}), & \boldsymbol{r} \in \Omega_i, \\ 0, & \boldsymbol{r} \notin \Omega_i. \end{cases} \tag{6.8b}$$

$$i\omega\mu_e \mathscr{S}_e[\boldsymbol{j}_e^{\text{inc}} + \boldsymbol{j}_e^{\text{scat}}](\boldsymbol{r}) + \frac{i}{\omega\varepsilon_e}\mathscr{K}_e[\boldsymbol{j}_e^{\text{inc}} + \boldsymbol{j}_e^{\text{scat}}](\boldsymbol{r}) + \mathscr{D}_e[\boldsymbol{m}_e^{\text{inc}} + \boldsymbol{m}_e^{\text{scat}}](\boldsymbol{r}) = \begin{cases} \mathbf{E}_e(\boldsymbol{r}), & \boldsymbol{r} \in \Omega_e, \\ 0, & \boldsymbol{r} \notin \Omega_e, \end{cases} \tag{6.9a}$$

$$-i\omega\varepsilon_e \mathscr{S}_e[\boldsymbol{m}_e^{\text{inc}} + \boldsymbol{m}_e^{\text{scat}}](\boldsymbol{r}) - \frac{i}{\omega\mu_e}\mathscr{K}_e[\boldsymbol{m}_e^{\text{inc}} + \boldsymbol{m}_e^{\text{scat}}](\boldsymbol{r}) + \mathscr{D}_e[\boldsymbol{j}_e^{\text{inc}} + \boldsymbol{j}_e^{\text{scat}}](\boldsymbol{r}) = \begin{cases} \mathbf{H}_e(\boldsymbol{r}), & \boldsymbol{r} \in \Omega_e, \\ 0, & \boldsymbol{r} \notin \Omega_e. \end{cases} \tag{6.9b}$$

Following the same steps as in the bounded-obstacle case discussed in section 5.3, we obtain the following system of integral equations

$$\begin{aligned} &\boldsymbol{m}(\boldsymbol{r}) + \mathrm{R}_\varepsilon^\Delta[\boldsymbol{m}](\boldsymbol{r}) + \mathrm{S}_\varepsilon^\Delta[\boldsymbol{j}](\boldsymbol{r}) + \mathrm{T}_\varepsilon^\Delta[\boldsymbol{j}](\boldsymbol{r}) = \\ &\qquad - \left(\boldsymbol{m}^{\text{inc}}(\boldsymbol{r}) + \mathrm{R}_\varepsilon^\Delta[\boldsymbol{m}^{\text{inc}}](\boldsymbol{r}) + \mathrm{S}_\varepsilon^\Delta[\boldsymbol{j}^{\text{inc}}](\boldsymbol{r}) + \mathrm{T}_\varepsilon^\Delta[\boldsymbol{j}^{\text{inc}}](\boldsymbol{r})\right), \end{aligned} \tag{6.10a}$$

$$\begin{aligned} &\boldsymbol{j}(\boldsymbol{r}) + \mathrm{R}_\mu^\Delta[\boldsymbol{j}](\boldsymbol{r}) - \mathrm{S}_\mu^\Delta[\boldsymbol{m}](\boldsymbol{r}) - \mathrm{T}_\mu^\Delta[\boldsymbol{m}](\boldsymbol{r}) = \\ &\qquad - \left(\boldsymbol{j}^{\text{inc}}(\boldsymbol{r}) + \mathrm{R}_\mu^\Delta[\boldsymbol{j}^{\text{inc}}](\boldsymbol{r}) - \mathrm{S}_\mu^\Delta[\boldsymbol{m}^{\text{inc}}](\boldsymbol{r}) - \mathrm{T}_\mu^\Delta[\boldsymbol{m}^{\text{inc}}](\boldsymbol{r})\right), \end{aligned} \tag{6.10b}$$

[1] Although the representation theorems presented are for bounded obstacles, a limiting form akin to that in [67] can be used to justify that an integral representation exists for waveguide structures with infinite boundaries.

where all the operators involved are given by integrals along the complete *infinite* boundary Γ of the waveguide. The operators on the left-hand side act only on the scattered densities; in virtue of section 6.1, the product of the densities times the relevant kernels have non-vanishing oscillations along the surface of the waveguide, hence the windowing technique provides an effective way to numerically truncate and evaluate these operators. On the contrary, the operators on the right-hand side act on the incident densities, for which the waves travel in the direction opposite to those inherent in the kernels, so that the net oscillations of the integrands may vanish. A strategy designed to evaluate these right-hand operators in spite of the potential loss of integrand oscillatory character is presented in the following section.

6.4.1 Evaluation of incident contributions

In order to overcome the difficulty associated with the evaluation of the right-hand side expressions in equation (6.10), we make use of an auxiliary representation for the incident mode. To do this, we denote by Γ^w the portion of the waveguide for which the window function is greater than zero,

$$\Gamma^w = \Gamma \cap \{\boldsymbol{r} : w_A(\boldsymbol{r}) > 0\}, \tag{6.11}$$

and we let Γ^∞ denote the portion of the SIW that carries the incident mode that is not contained in Γ^w:

$$\Gamma^\infty = \Omega^{\text{inc}} \cap (\Gamma \setminus \Gamma^w)\,. \tag{6.12}$$

Further, we define the auxiliary (infinite) boundary $\Gamma^\perp$ to be the plane perpendicular to the SIW with the incident mode, and that crosses the waveguide exactly at the junction between Γ^w and Γ^∞. Additionally, we consider Ω^∞ to be the portion of Ω^{inc} that goes from $\Gamma^\perp$ to infinity in the direction opposite to the incoming mode—this notation is analogous to that used for the one presented in Chapter 2 and depicted in Figure 2.1 for the two-dimensional case. Using these definitions together with the representation formulas from section 5.2, we obtain

$$i\omega\mu_i(\mathscr{S}_i^\infty + \mathscr{S}_i^\perp)[\boldsymbol{j}_i^{\text{inc}}](\boldsymbol{r}) + \frac{i}{\omega\varepsilon_i}(\mathscr{K}_i^\infty + \mathscr{K}_i^\perp)[\boldsymbol{j}_i^{\text{inc}}](\boldsymbol{r}) + (\mathscr{D}_i^\infty + \mathscr{D}_i^\perp)[\boldsymbol{m}_i^{\text{inc}}+](\boldsymbol{r}) = \begin{cases} \mathbf{E}_i(\boldsymbol{r}), & \boldsymbol{r} \in (\Omega_i \cap \Omega^\infty), \\ 0, & \boldsymbol{r} \notin (\Omega_i \cap \Omega^\infty), \end{cases} \tag{6.13a}$$

$$i\omega\mu_e(\mathscr{S}_e^{\infty}+\mathscr{S}_e^{\perp})[\boldsymbol{j}_e^{\mathrm{inc}}](\boldsymbol{r})+\frac{i}{\omega\varepsilon_e}(\mathscr{K}_e^{\infty}+\mathscr{K}_e^{\perp})[\boldsymbol{j}_e^{\mathrm{inc}}](\boldsymbol{r})+(\mathscr{D}_e^{\infty}+\mathscr{D}_e^{\perp})[\boldsymbol{m}_e^{\mathrm{inc}}+](\boldsymbol{r})=\begin{cases}\mathbf{E}_e(\boldsymbol{r}), & \boldsymbol{r}\in(\Omega_e\cap\Omega^{\infty}),\\ 0, & \boldsymbol{r}\notin(\Omega_e\cap\Omega^{\infty}),\end{cases}\tag{6.13b}$$

where the superscripts ∞ and $\perp$ in the potential operators denote integration over Γ^{∞} and $\Gamma^{\perp}$ (normal pointing away from Ω^{∞}), respectively. Similar expressions for $\mathbf{H}_i$ and $\mathbf{H}_e$ hold by exchanging $\mathbf{E}\to\mathbf{H}$, $\boldsymbol{j}\to\boldsymbol{m}$, $\boldsymbol{m}\to\boldsymbol{j}$ and $\mu\to-\varepsilon$.

The idea of this auxiliary formulation for the field was introduced for the two-dimensional case in Chapter 2 (see also [22]), and in its three-dimensional variant—equation (6.13))—can be used to evaluate the challenging right-hand side in equation (6.10). In detail, consider a point $\boldsymbol{r}\in\Gamma^{w}$, then, in view of $\boldsymbol{r}\notin((\Omega_e\cap\Omega^{\infty})\cup(\Omega_i\cap\Omega^{\infty}))$, together with equation (6.13), we have

$$\begin{aligned}\mathrm{R}_{\varepsilon}^{\Delta}[\boldsymbol{m}^{\mathrm{inc}}](\boldsymbol{r})+\mathrm{S}_{\varepsilon}^{\Delta}[\boldsymbol{j}^{\mathrm{inc}}](\boldsymbol{r})+\mathrm{T}_{\varepsilon}^{\Delta}[\boldsymbol{j}^{\mathrm{inc}}](\boldsymbol{r})&=(\mathrm{R}_{\varepsilon}^{\Delta,w}-\mathrm{R}_{\varepsilon}^{\Delta,\perp})[\boldsymbol{m}^{\mathrm{inc}}](\boldsymbol{r})+\\&\quad(\mathrm{S}_{\varepsilon}^{\Delta,w}-\mathrm{S}_{\varepsilon}^{\Delta,\perp})[\boldsymbol{j}^{\mathrm{inc}}](\boldsymbol{r})+(\mathrm{T}_{\varepsilon}^{\Delta,w}-\mathrm{T}_{\varepsilon}^{\Delta,\perp})[\boldsymbol{j}^{\mathrm{inc}}](\boldsymbol{r}),\end{aligned}\tag{6.14a}$$

$$\begin{aligned}\mathrm{R}_{\mu}^{\Delta}[\boldsymbol{j}^{\mathrm{inc}}](\boldsymbol{r})-\mathrm{S}_{\mu}^{\Delta}[\boldsymbol{m}^{\mathrm{inc}}](\boldsymbol{r})-\mathrm{T}_{\mu}^{\Delta}[\boldsymbol{m}^{\mathrm{inc}}](\boldsymbol{r})&=(\mathrm{R}_{\mu}^{\Delta,w}-\mathrm{R}_{\mu}^{\Delta,\perp})[\boldsymbol{j}^{\mathrm{inc}}](\boldsymbol{r})-\\&\quad(\mathrm{S}_{\mu}^{\Delta,w}-\mathrm{S}_{\mu}^{\Delta,\perp})[\boldsymbol{m}^{\mathrm{inc}}](\boldsymbol{r})-(\mathrm{T}_{\mu}^{\Delta,w}-\mathrm{T}_{\mu}^{\Delta,\perp})[\boldsymbol{m}^{\mathrm{inc}}](\boldsymbol{r}),\end{aligned}\tag{6.14b}$$

where, again, the superscripts ∞ and $\perp$ in the integral operators denote integration over Γ^{∞} and $\Gamma^{\perp}$, respectively. The identity in equation (6.14) is an important result from this thesis in view of Remark 6.4.1.

Remark 6.4.1 *The operators in the right-hand side of equation* (6.14) *involve integrals that can be accurately computed. The integrals over the bounded surface* Γ^{w} *can be treated as in the bounded obstacle case. On the other hand, the integrals over* $\Gamma^{\perp}$*, in spite of involving an infinite surface, the integrands are* ***exponentially*** *decaying towards infinity—along* $\Gamma^{\perp}$*—due to the nature of the incident bound modes. This exponential decay allows us to truncate* $\Gamma^{\perp}$ *to perform the integrals, incurring in an exponentially small truncation error.*

Putting it all together, we obtain the following WGF system of integral equations for a waveguide structure illuminated by a bound mode:

$$\boldsymbol{m}(\boldsymbol{r}) + \mathrm{R}_{\varepsilon}^{\Delta}[W_A\boldsymbol{m}](\boldsymbol{r}) + \mathrm{S}_{\varepsilon}^{\Delta}[W_A\boldsymbol{j}](\boldsymbol{r}) + \mathrm{T}_{\varepsilon}^{\Delta}[W_A\boldsymbol{j}](\boldsymbol{r}) = \mathbf{b}_m^{\perp}(\boldsymbol{r}), \quad \boldsymbol{r} \in \Gamma^w, \tag{6.15a}$$

$$\boldsymbol{j}(\boldsymbol{r}) + \mathrm{R}_{\mu}^{\Delta}[W_A\boldsymbol{j}](\boldsymbol{r}) - \mathrm{S}_{\mu}^{\Delta}[W_A\boldsymbol{m}](\boldsymbol{r}) - \mathrm{T}_{\mu}^{\Delta}[W_A\boldsymbol{m}](\boldsymbol{r}) = \mathbf{b}_j^{\perp}(\boldsymbol{r}), \quad \boldsymbol{r} \in \Gamma^w, \tag{6.15b}$$

where

$$\mathbf{b}_m^{\perp}(\boldsymbol{r}) = -\Big(\boldsymbol{m}^{\mathrm{inc}} + (\mathrm{R}_{\varepsilon}^{\Delta,w} - \mathrm{R}_{\varepsilon}^{\Delta,\perp})[\boldsymbol{m}^{\mathrm{inc}}](\boldsymbol{r}) + (\mathrm{S}_{\varepsilon}^{\Delta,w} - \mathrm{S}_{\varepsilon}^{\Delta,\perp})[\boldsymbol{j}^{\mathrm{inc}}](\boldsymbol{r}) + (\mathrm{T}_{\varepsilon}^{\Delta,w} - \mathrm{T}_{\varepsilon}^{\Delta,\perp})[\boldsymbol{j}^{\mathrm{inc}}](\boldsymbol{r})\Big), \tag{6.16a}$$

$$\mathbf{b}_j^{\perp}(\boldsymbol{r}) = \Big(\boldsymbol{j}^{\mathrm{inc}} + (\mathrm{R}_{\mu}^{\Delta,w} - \mathrm{R}_{\mu}^{\Delta,\perp})[\boldsymbol{j}^{\mathrm{inc}}](\boldsymbol{r}) - (\mathrm{S}_{\mu}^{\Delta,w} - \mathrm{S}_{\mu}^{\Delta,\perp})[\boldsymbol{m}^{\mathrm{inc}}](\boldsymbol{r}) - (\mathrm{T}_{\mu}^{\Delta,w} - \mathrm{T}_{\mu}^{\Delta,\perp})[\boldsymbol{m}^{\mathrm{inc}}](\boldsymbol{r})\Big). \tag{6.16b}$$

6.5 Numerical examples

To illustrate the accuracy and applicability of the WGF method, this section presents several numerical examples. Each example was selected so as to highlight a particular signature difficulty arising in waveguide simulations. For all simulations in this problem, we take $n_e = 1.0$ and $n_i = 1.47$ (SiO_2). Throughout this section, to illustrate where the electromagnetic energy is concentrated, we use the complex Poynting vector $\mathbf{S} = \frac{1}{2}(\mathbf{E} \times \mathbf{H}^*)$; see [46, section 6.9].

Our first example concerns a uniform circular waveguide. As indicated in section 3.2, the fields, mode profiles and propagation constants for this problem are given in terms of Bessel functions. Figure 6.1 compares the WGF mode solution (d-e) to the corresponding result obtained without use of a window function (f-g). Figure 6.1 (a) presents the error of the solution along the center of the waveguide core; for this particular case, where a discretization of 18×18 (~ 9 points per mode's wavelength) is used, accuracies of order 10^{-4} are achieved by the WGF method. The un-windowed solution does match some qualitative features of the field, but it is otherwise clearly wrong: not just the field values in the center of the waveguide are off (as indicated by Figure 6.1 (a)), but Figure 6.1 (f-g) displays incorrectly curved wave fronts which arise as the physical (straight) wavefronts are superimposed to the unphysical reflections arising from the truncation edge.

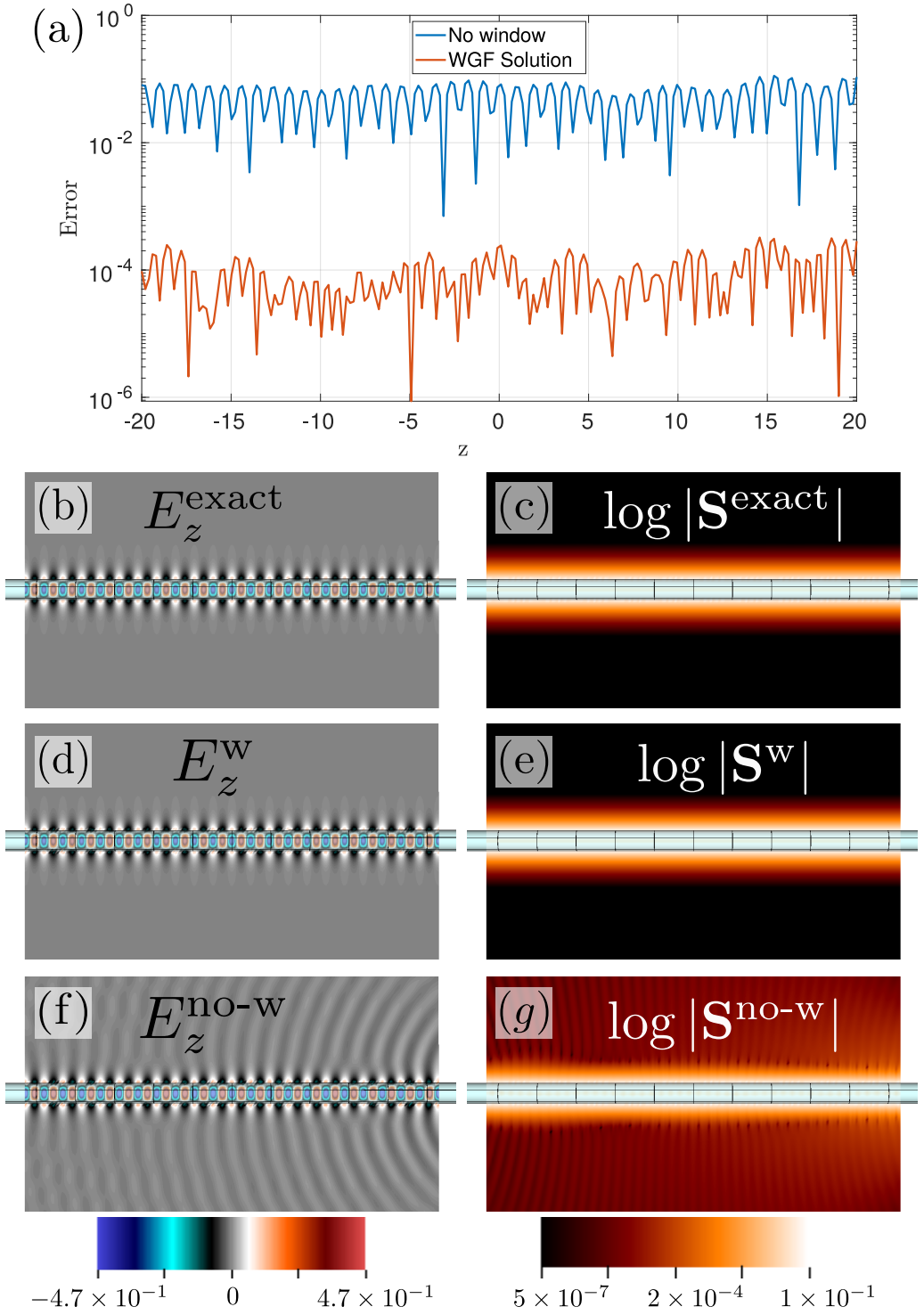

Figure 6.1: Mode propagation along a uniform circular waveguide. The error in E_z along the center of the waveguide is presented in (a). In (b), (d) and (f), the values of E_z are displayed for the exact, windowed and un-windowed solutions, respectively. On the other hand, (c), (e) and (g) concern the logarithm of the magnitude of the Poynting vector, also for the exact, windowed and un-windowed solutions, respectively.

For our second example, in Figure 6.2 we present the simulated fields for a waveguide with elliptical cross-section illuminated by an electromagnetic beam of the form of equation (5.42), showing in particular, in Figures 6.2 (c) and (d), that a certain amount of energy is coupled to the waveguide. At the same time, the logarithmic scale reveals that the beam also reflects and passes through the structure. In fact, this example is representative of the "mode launching" problem, for which one illuminates a waveguide with the purpose of producing such a coupling with propagating modes in the waveguide.

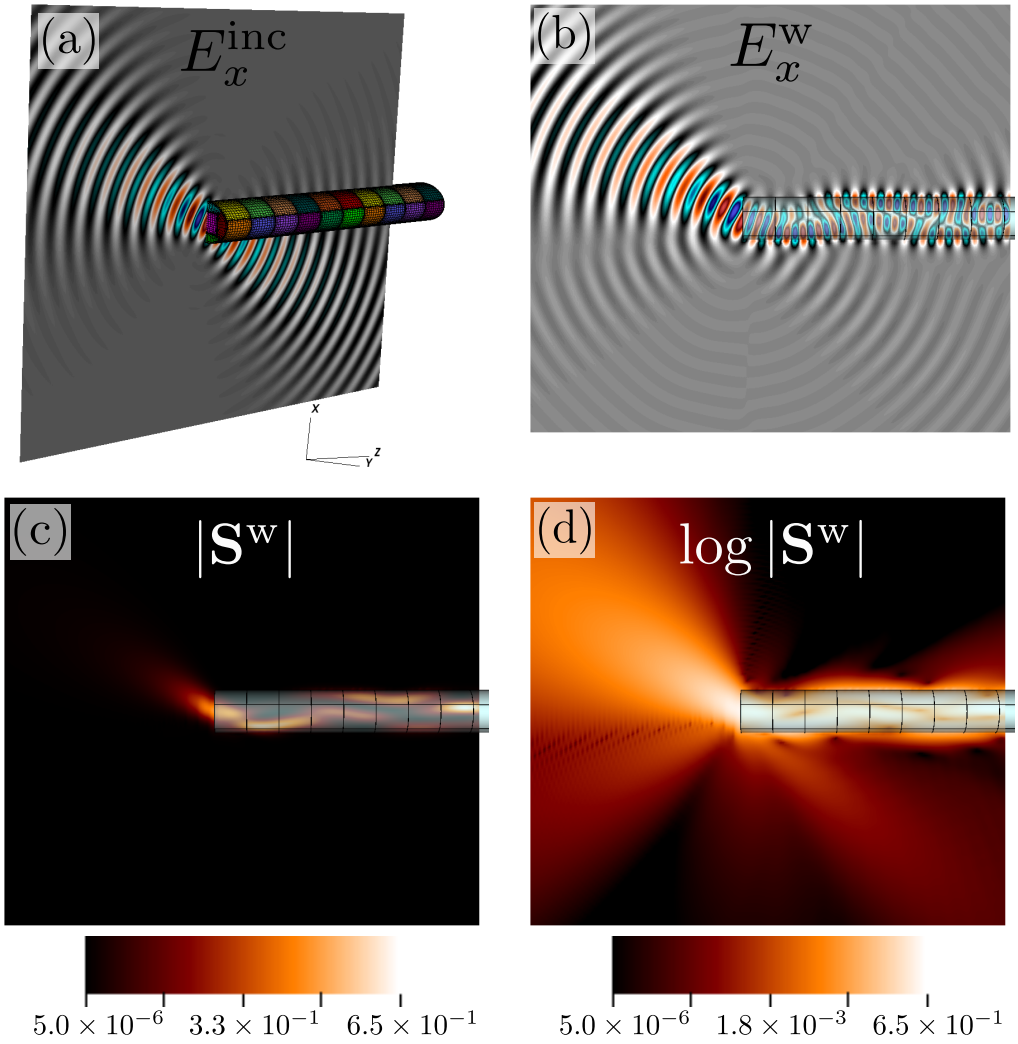

Figure 6.2: Illumination of an elliptical waveguide by an electromagnetic beam. In this mode launching problem, several modes get excited, and the simulation shows the "bouncing" of the trapped fields inside the waveguide.

Figure 6.3 presents the simulation of a circular waveguide with a 90° bend illuminated by a bound mode. Figure 6.3 (a) shows the patch structure, as well

as the discretization of $\Gamma^{\perp}$ used in this example, which corresponds to a disk. In Figure 6.3 (b), one of the components of the scattered density is displayed, showing a discontinuity at the point at which the horizontal straight portion of the waveguide meets the curved structure. The incident field is prescribed in this horizontal section, and the scattered field in this region only results from the (weak) reflections that arise from scattering from the curved portion. Figure 6.3 (c) shows that the mode is mostly preserved across the curved region: the discrepancy in character of the field shown in the vertical and horizontal sections is only a matter of appearance, reflecting the fact that the x-component of the field is the tangential component in the vertical section, but it is the normal component in the horizontal section. A different type of transition is demonstrated in Figure 6.4. In this case, the structure is illuminated by a bound mode and a waveguide taper is used to provide a transition between waveguides of two different radii.

Our last example concerns a dielectric antenna fed by a bound mode. Figure 6.5 displays the fields resulting in this case. In particular, Figures 6.5 (c) and (d) show that the energy is mostly bound within the waveguide core. The logarithmic plot in Figure 6.5 (d) clearly demonstrates the energy distribution in the near field.

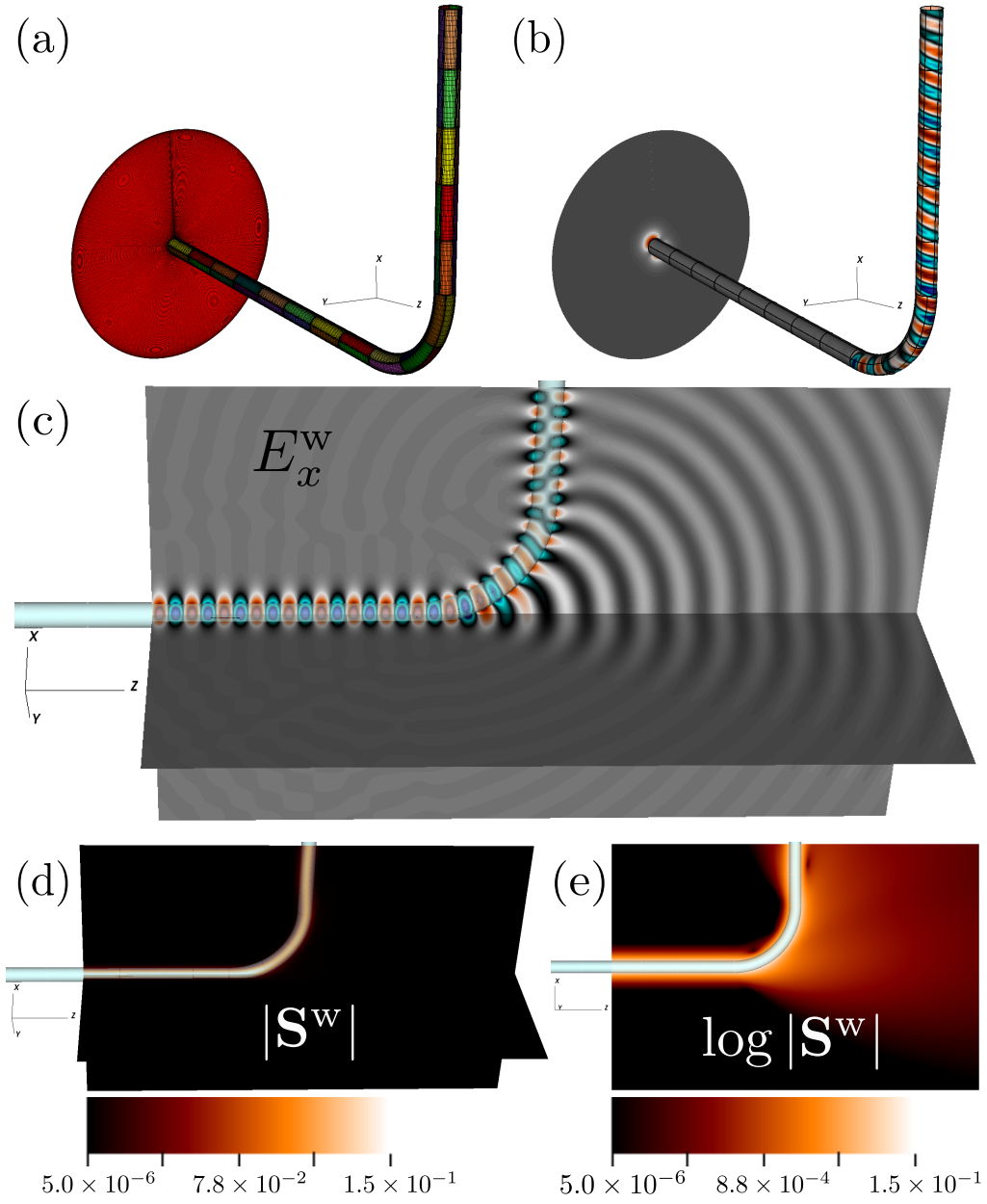

Figure 6.3: Mode propagation along a 90° bend.

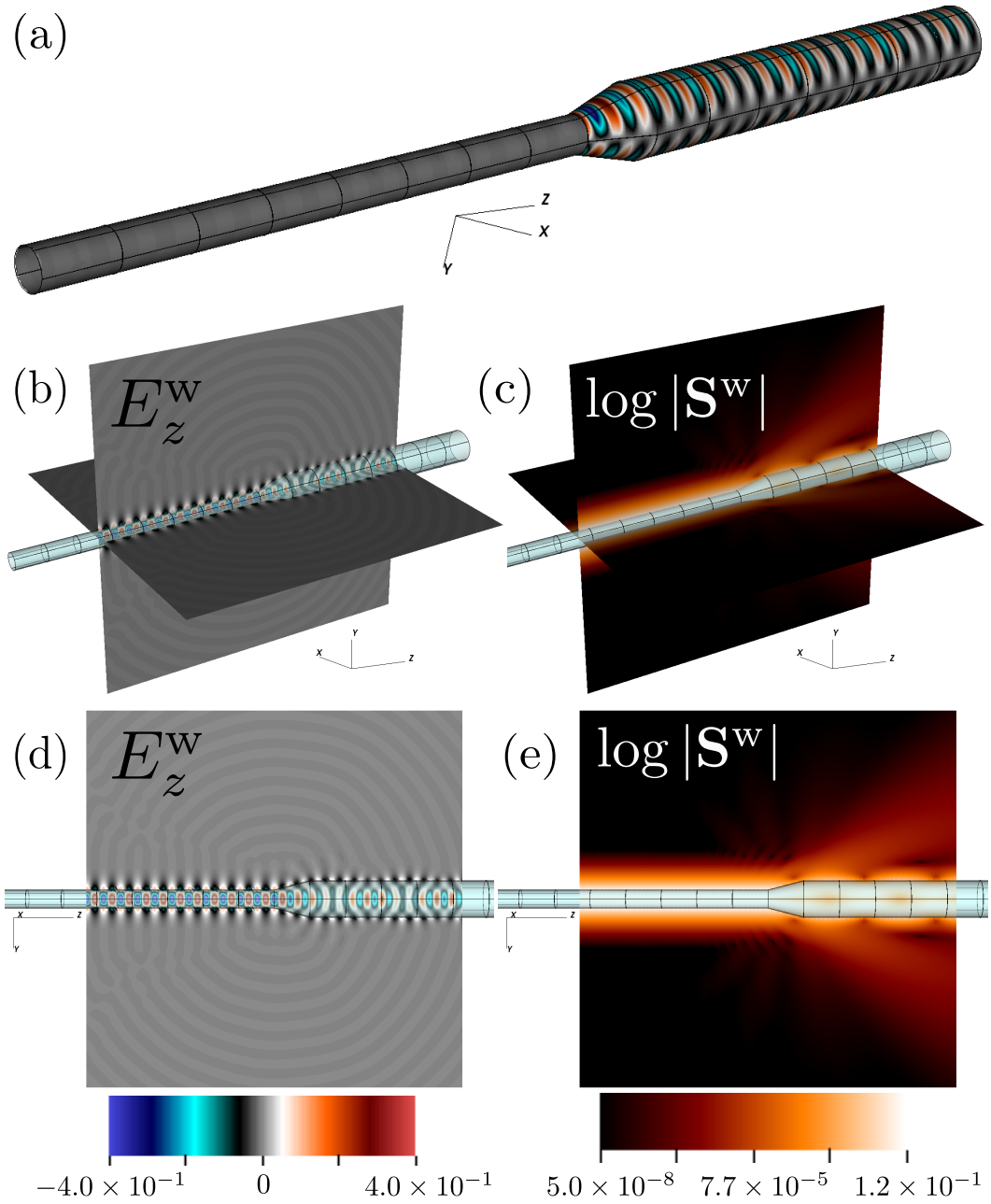

Figure 6.4: Simulation of a taper structure on which a circular waveguide transitions to another with a bigger diameter.

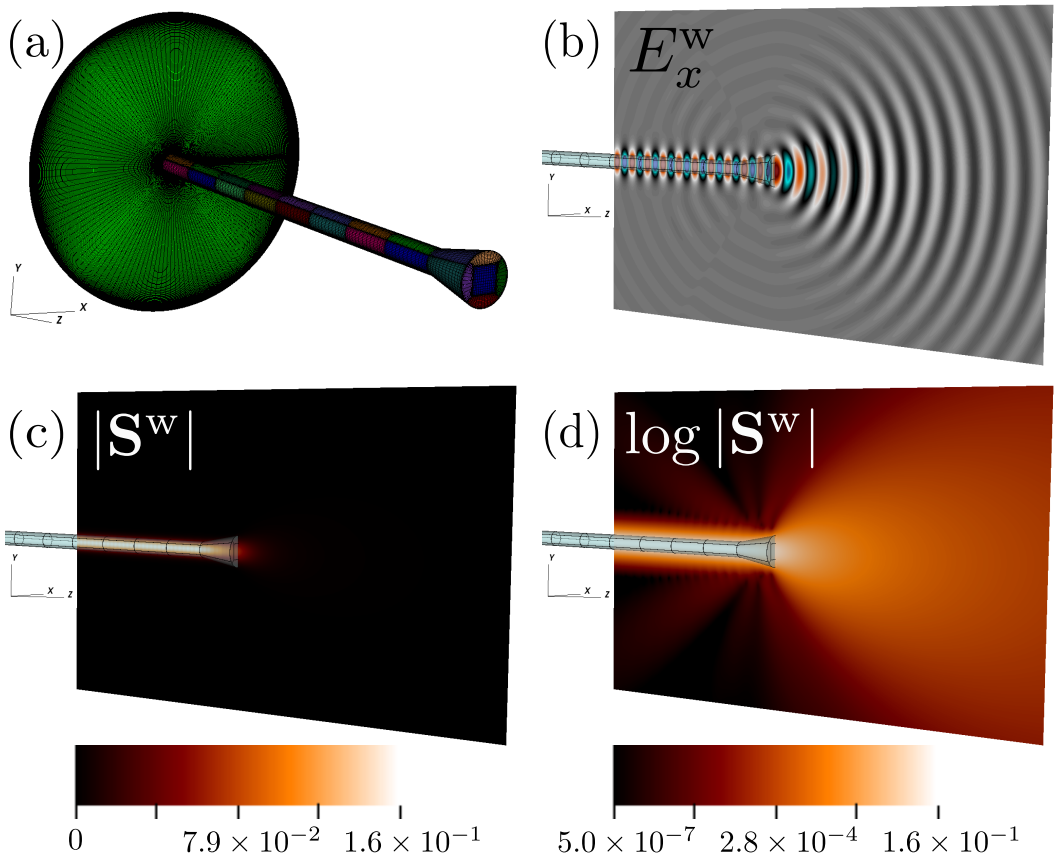

Figure 6.5: Modeling of a dielectric antenna by a terminated waveguide.

Shape optimization of electromagnetic devices

Chapter 7

BIE GRADIENT-BASED OPTIMIZATION OF ELECTROMAGNETIC DEVICES

In the previous chapters, we developed fast, accurate algorithms for a variety of electromagnetic simulation problems. While simulation can be a challenging task, it has significant merits for real-life applications, including as an effective means to guide the design of electromagnetic devices for a wide range of applications.

In the field of photonics, design on the basis of gradient-based optimization has seen a significant increase in use in recent years, in great part due to the proven advantages of the adjoint techniques for gradient evaluation [36, 41, 44, 53, 64–66, 71, 82]. In brief, most design problems for photonic devices can be modeled by maximizing or minimizing a functional of the electromagnetic fields, which in turn, depend on the incident excitations and a set of design parameters that characterize the refractive-index function $n(\boldsymbol{r})$ throughout the simulation domain. Within volumetric solver paradigms used by other authors, this typically means that the design parameters are the values of the refractive index function at all the discretization points. Although these techniques have been quite useful, they tend to incur significant thresholding errors that occur as an optimized refractive-index function $n^{\text{opt}}(\boldsymbol{r})$ that varies continuously, and which spans an infinity of refractive-index values, is approximated by a discontinuous refractive-index function that only takes two (or small finite number) values.

Many such photonic devices are mostly comprised of piecewise constant dielectric materials, which can be efficiently simulated using boundary integral equation methods. Yet, we are not aware of any previous contributions (except for this author's collaborative work in [74]) that rely on use of boundary integral methods as a simulation engine for optimization of photonic devices. In this chapter, we introduce such an integral methodology for the simulation and the efficient computation of the gradient of functionals that arise in electromagnetic device design. Relying on boundary parametrization that smoothly depend on a set of design parameters, we derive a continuous adjoint problem from which the gradient can be efficiently computed. We pay close attention to the implementation details, given that significant computational time can be saved by exploiting the non-trivial underlying sparsity of

some matrices associated to this problem.

7.1 Device optimization in a boundary integral setting

Consider the problem of three-dimensional scattering by a collection of N_{obj} dielectric obstacles Ω_j for $j = 1 \dots N_{\text{obj}}$ within an "exterior" dielectric matrix Ω_e – which carries the incident fields $\mathbf{E}^{\text{inc}}$ and $\mathbf{H}^{\text{inc}}$. Denote by $\boldsymbol{\alpha} = [\alpha_1, \alpha_2, \cdots, \alpha_M]^T \in \mathbb{R}^M$ the vector of design parameters, and let the boundary of the $j-$th obstacle be $\Gamma_j(\boldsymbol{\alpha})$, and $\Gamma = \cup_j \Gamma_j$. Let us also introduce the following notation for the dielectric integral equations from Chapter 5, which will be needed for the optimization problem.

Let us define the extended vector

$$\boldsymbol{\Psi} = \begin{bmatrix} \boldsymbol{\Psi}^{\boldsymbol{m}}(\boldsymbol{r}) \\ \boldsymbol{\Psi}^{\boldsymbol{j}}(\boldsymbol{r}) \end{bmatrix}, \quad \boldsymbol{r} \in \Gamma(\boldsymbol{\alpha}), \tag{7.1}$$

where $\boldsymbol{\Psi}^{\boldsymbol{m}}$ and $\boldsymbol{\Psi}^{\boldsymbol{j}}$ are the integral densities associated with the magnetic and electric currents, so that the operator associated with the dielectric integral equations is given by

$$\mathrm{A}(\boldsymbol{\Psi}, \boldsymbol{\alpha}) = \begin{bmatrix} \boldsymbol{\Psi}^{\boldsymbol{m}}(\boldsymbol{r}) + \mathrm{R}_{\varepsilon}^{\Delta}[\boldsymbol{\Psi}^{\boldsymbol{m}}](\boldsymbol{r}) + \mathrm{S}_{\varepsilon}^{\Delta}[\boldsymbol{\Psi}^{\boldsymbol{j}}](\boldsymbol{r}) + \mathrm{T}_{\varepsilon}^{\Delta}[\boldsymbol{\Psi}^{\boldsymbol{j}}](\boldsymbol{r}) \\ \boldsymbol{\Psi}^{\boldsymbol{j}}(\boldsymbol{r}) + \mathrm{R}_{\mu}^{\Delta}[\boldsymbol{\Psi}^{\boldsymbol{j}}](\boldsymbol{r}) - \mathrm{S}_{\mu}^{\Delta}[\boldsymbol{\Psi}^{\boldsymbol{m}}](\boldsymbol{r}) - \mathrm{T}_{\mu}^{\Delta}[\boldsymbol{\Psi}^{\boldsymbol{m}}](\boldsymbol{r}) \end{bmatrix}, \quad \boldsymbol{r} \in \Gamma(\boldsymbol{\alpha}), \tag{7.2}$$

while the associated right-hand side is given by

$$\mathrm{b}(\boldsymbol{\alpha}) = \begin{bmatrix} \dfrac{2\varepsilon_e}{\varepsilon_e + \varepsilon_i} \mathbf{E}^{\text{inc}}(\boldsymbol{r}) \times \boldsymbol{n}(\boldsymbol{r}) \\ \dfrac{2\mu_e}{\mu_e + \mu_i} \mathbf{H}^{\text{inc}}(\boldsymbol{r}) \times \boldsymbol{n}(\boldsymbol{r}) \end{bmatrix}, \quad \boldsymbol{r} \in \Gamma(\boldsymbol{\alpha}). \tag{7.3}$$

Defining the operator

$$T(\boldsymbol{\Psi}, \boldsymbol{\alpha}) \equiv \mathrm{A}(\boldsymbol{\Psi}, \boldsymbol{\alpha}) - \mathrm{b}(\boldsymbol{\alpha}), \tag{7.4}$$

then, letting S denote the solution map (that produces the solution $\boldsymbol{\Psi}$ for any given parameter vector $\boldsymbol{\alpha}$), we clearly have

$$T(S(\boldsymbol{\alpha}), \boldsymbol{\alpha}) = 0, \tag{7.5}$$

or equivalently, in the reduced form

$$\widetilde{T}(\boldsymbol{\alpha}) \equiv T(S(\boldsymbol{\alpha}), \boldsymbol{\alpha}) = 0. \tag{7.6}$$

Consider the inner product defined by

$$\left\langle \boldsymbol{\Phi}, \boldsymbol{\Psi} \right\rangle_{\Gamma} = \int_{\Gamma} \overline{\boldsymbol{\Phi}^{\boldsymbol{m}}(\boldsymbol{r}')} \cdot \boldsymbol{\Psi}^{\boldsymbol{m}}(\boldsymbol{r}') \, \mathrm{d}\sigma(\boldsymbol{r}') + \int_{\Gamma} \overline{\boldsymbol{\Phi}^{\boldsymbol{j}}(\boldsymbol{r}')} \cdot \boldsymbol{\Psi}^{\boldsymbol{j}}(\boldsymbol{r}') \, \mathrm{d}\sigma(\boldsymbol{r}'). \tag{7.7}$$

Furthermore, we seek to maximize objective functions of the form

$$J(\boldsymbol{\Psi}, \boldsymbol{\alpha}) = |I(\boldsymbol{\Psi}, \boldsymbol{\alpha})|^2, \tag{7.8}$$

with

$$I(\boldsymbol{\Psi}, \boldsymbol{\alpha}) = a^{\mathrm{inc}}(\boldsymbol{\alpha}) + \left\langle \mathbf{K}(\boldsymbol{\alpha}), \boldsymbol{\Psi} \right\rangle_{\Gamma}, \tag{7.9}$$

and where the specific forms of $a^{\mathrm{inc}}(\boldsymbol{\alpha})$ and $\mathbf{K}(\boldsymbol{\alpha})$ depends on the desired objective function. In its reduced form [34, 77], we have that the objective functional $f(\boldsymbol{\alpha})$ is given by

$$f(\boldsymbol{\alpha}) \equiv J(S(\boldsymbol{\alpha}), \boldsymbol{\alpha}). \tag{7.10}$$

Then, the optimization problem considered here can be defined as

$$\begin{cases} \max \; J(\boldsymbol{\Psi}, \boldsymbol{\alpha}), \\ \text{subject to:} \\ \quad T(\boldsymbol{\Psi}, \boldsymbol{\alpha}) = 0, \quad \boldsymbol{\alpha} \in \mathbb{R}^M. \end{cases} \tag{7.11}$$

Although this optimization problem is generally quite challenging, in view of an optimization landscape which generally contains large numbers of local maxima, in practice "sufficiently optimal" local maxima may provide significant improvements over designs based on human expertise alone. With this in mind, we seek to use a gradient-based optimization approach.

The most direct way to numerically approximate the gradient is to apply a finite difference approximation [51] to equation (7.10), which yields

$$[\nabla f(\boldsymbol{\alpha})]_i = \frac{f(\boldsymbol{\alpha} + \delta \mathbf{e}_i) - f(\boldsymbol{\alpha})}{\delta}, \tag{7.12}$$

where $\mathbf{e}_i$ is i-th vector of the standard basis ($[\mathbf{e}_i]_j = \delta_{ij}$). The approximation in equation (7.12) has a very simple expression and is a good black-box method; the method only requires an adequate solver for the forward problem and a procedure for the evaluation of the objective function. However, we can see that this approach can be quite expensive if we consider problems with parameters numbering from

$M \approx 10$ to $M \approx 1000$, or even $M \approx 10^6$ and beyond. Indeed, equation (7.12) requires $M + 1$ forward simulations, where, in general, each forward simulation can be quite expensive, specially in the three-dimensional case considered here. Instead, in the following section we present a variant of the classical adjoint-based method that is applicable in the context of electromagnetic boundary integral equations, which provides valuable continuous adjoint formulation to which acceleration methods [16] can be naturally applied. Under this framework, the full gradient can be evaluated on the basis of merely two simulations—one for the forward system, and one for a related adjoint problem—as opposed to $M + 1$ forward simulations required under the direct approach in equation (7.12). (In addition to two simulations, the adjoint approach additionally requires $M+1$ sparse, and, therefore, inexpensively computed forward maps, see section 7.2.1.)

Remark 7.1.1 *An appealing feature of the integral-equation approach to photonic device optimization arises precisely from its focus on discretization of* interfaces. *In such a setup, the optimization parameters are used to control the parametrizations in terms of* (u, v) *parameters and geometry controlling parameters* $\boldsymbol{\alpha}$*, and the actual electromagnetic discretization takes place on a fixed computational grid. For volumetric approaches, in contrast, the variation of a portion of an interface implies a change in the material properties of portions of the structure being simulated—which presents significant challenges.*

7.2 Adjoint computation of the gradient

In order to provide a consistent framework for the computation of the gradient via the adjoint method, let us call U the domain of the operator A in equation (7.2), which, in each one of the available existence and regularity theories for integral-equation contexts, is a Banach space, as well as a vector subspace of $L^2(\Gamma)$. Additionally, denote $V = \mathbb{R}^M$ with the usual inner product. Then, the objective functional in equation (7.8) is a mapping of the form $J : U \times V \to \mathbb{R}$. We assume J to be Gâteaux differentiable (an assumption that is often trivially verified in practice), and we denote the directional derivative of J at $(\boldsymbol{\Psi}, \boldsymbol{\alpha})$, in the direction $(\boldsymbol{\Phi}, \boldsymbol{\beta})$ by [34, 77]

$$dJ(\boldsymbol{\Psi}, \boldsymbol{\alpha}; \boldsymbol{\Phi}, \boldsymbol{\beta}) = \lim_{t \to 0^+} \frac{1}{t} \Big(J(\boldsymbol{\Psi} + t\boldsymbol{\Phi}, \boldsymbol{\alpha} + t\boldsymbol{\beta}) - J(\boldsymbol{\Psi}, \boldsymbol{\alpha}) \Big). \tag{7.13}$$

With this notation, we can write the directional derivative of the reduced cost functional at $\boldsymbol{\alpha}$ in the direction $\boldsymbol{\beta}$

$$df(\boldsymbol{\alpha}; \boldsymbol{\beta}) = dJ(S(\boldsymbol{\alpha}), \boldsymbol{\alpha}; dS(\boldsymbol{\alpha}; \boldsymbol{\beta}), 0) + dJ(S(\boldsymbol{\alpha}), \boldsymbol{\alpha}; 0, \boldsymbol{\beta}), \tag{7.14}$$

where

$$dS(\boldsymbol{\alpha};\boldsymbol{\beta}) = \lim_{t\to 0^+} \frac{1}{t}\Big(S(\boldsymbol{\alpha}+t\boldsymbol{\beta}) - S(\boldsymbol{\alpha})\Big). \tag{7.15}$$

Then, the gradient can be written in the form

$$[\nabla f(\boldsymbol{\alpha})]_i = df(\boldsymbol{\alpha}, \mathbf{e}_i). \tag{7.16}$$

Similarly, we can take the directional derivative of the governing integral equation (7.6), which in turn must be zero independent of the direction:

$$dT(S(\boldsymbol{\alpha}), \boldsymbol{\alpha}; dS(\boldsymbol{\alpha};\boldsymbol{\beta}), 0) + dT(S(\boldsymbol{\alpha}), \boldsymbol{\alpha}; 0, \boldsymbol{\beta}) = 0, \tag{7.17}$$

and to use this expression in conjunction with equation (7.14), we take the inner product of equation (7.17) with an arbitrary function $\boldsymbol{\psi} \in U$

$$\big\langle \boldsymbol{\psi}, dT(S(\boldsymbol{\alpha}), \boldsymbol{\alpha}; dS(\boldsymbol{\alpha};\boldsymbol{\beta}), 0)\big\rangle_\Gamma + \big\langle \boldsymbol{\psi}, dT(S(\boldsymbol{\alpha}), \boldsymbol{\alpha}; 0, \boldsymbol{\beta})\big\rangle_\Gamma = 0. \tag{7.18}$$

We can also simplify some of the expressions from above. In view of equation (7.4) and the linearity of $\mathrm{A}(\boldsymbol{\Psi}, \boldsymbol{\alpha})$ on the first argument, we have

$$dT(S(\boldsymbol{\alpha}), \boldsymbol{\alpha}; dS(\boldsymbol{\alpha};\boldsymbol{\beta}), 0) = \mathrm{A}(dS(\boldsymbol{\alpha};\boldsymbol{\beta}), \boldsymbol{\alpha}). \tag{7.19}$$

At the same time, using equation (7.8), we have explicitly

$$\begin{aligned} dJ(S(\boldsymbol{\alpha}), \boldsymbol{\alpha}; dS(\boldsymbol{\alpha};\boldsymbol{\beta}), 0) =& \mathrm{Re}\big(2\,\overline{I(S(\boldsymbol{\alpha}), \boldsymbol{\alpha})}\big\langle \mathbf{K}(\boldsymbol{\alpha}), dS(\boldsymbol{\alpha};\boldsymbol{\beta})\big\rangle_\Gamma\big) \\ =& \mathrm{Re}\big(\big\langle 2\, I(S(\boldsymbol{\alpha}), \boldsymbol{\alpha})\mathbf{K}(\boldsymbol{\alpha}), dS(\boldsymbol{\alpha};\boldsymbol{\beta})\big\rangle_\Gamma\big) \end{aligned} \tag{7.20}$$

Because the variation in equation (7.14) has to be real, we can then combine equations (7.14), (7.18) and (7.19) to get

$$\begin{aligned} df(\boldsymbol{\alpha};\boldsymbol{\beta}) = \mathrm{Re}\Bigg[\Big(\big\langle \boldsymbol{\psi}, \mathrm{A}(dS(\boldsymbol{\alpha};\boldsymbol{\beta}), \boldsymbol{\alpha})\big\rangle_\Gamma + \big\langle 2I(S(\boldsymbol{\alpha}), \boldsymbol{\alpha})\mathbf{K}(\boldsymbol{\alpha}), dS(\boldsymbol{\alpha};\boldsymbol{\beta})\big\rangle_\Gamma\Big) + \\ \Big(\big\langle \boldsymbol{\psi}, dT(S(\boldsymbol{\alpha}), \boldsymbol{\alpha}; 0, \boldsymbol{\beta})\big\rangle_\Gamma + dJ(S(\boldsymbol{\alpha}), \boldsymbol{\alpha}; 0, \boldsymbol{\beta})\Big)\Bigg], \end{aligned} \tag{7.21}$$

which, using the properties of the inner product and the adjoint operator $\mathrm{A}^\dagger(\cdot, \boldsymbol{\alpha})$ of $\mathrm{A}(\cdot, \boldsymbol{\alpha})$, yields

$$\begin{aligned} df(\boldsymbol{\alpha};\boldsymbol{\beta}) = \mathrm{Re}\Bigg[\Big(\big\langle\, \mathrm{A}^\dagger(\boldsymbol{\psi}, \boldsymbol{\alpha}) + 2I(S(\boldsymbol{\alpha}), \boldsymbol{\alpha})\mathbf{K}(\boldsymbol{\alpha}), dS(\boldsymbol{\alpha};\boldsymbol{\beta})\big\rangle_\Gamma\Big) + \\ \Big(\big\langle \boldsymbol{\psi}, dT(S(\boldsymbol{\alpha}), \boldsymbol{\alpha}; 0, \boldsymbol{\beta})\big\rangle_\Gamma + dJ(S(\boldsymbol{\alpha}), \boldsymbol{\alpha}; 0, \boldsymbol{\beta})\Big)\Bigg]. \end{aligned} \tag{7.22}$$

Remark 7.2.1 *In equation* (7.22)*, two contributing terms are present: one that relates to the variations of the solution density dS, and another that concerns variations of the parameters* $\boldsymbol{\alpha}$ *while keeping the solution density constant. The first term is indeed the one that carries most of the computational cost—it requires a new solution of the system of integral equations for each direction needed. On the other hand, the second term can be approximated via certain evaluations of the forward map—i.e. the action—of the boundary integral operators, which are considerably cheaper to evaluate than a full solve.*

Using the solution $\boldsymbol{\psi}$ to the adjoint problem

$$\mathrm{A}^{\dagger}(\boldsymbol{\psi}, \boldsymbol{\alpha}) = -2I(S(\boldsymbol{\alpha}), \boldsymbol{\alpha})\mathbf{K}(\boldsymbol{\alpha}), \tag{7.23}$$

(which will be discussed in detail in section 7.3) then, equation (7.22) simplifies to

$$df(\boldsymbol{\alpha}; \boldsymbol{\beta}) = \mathrm{Re}\left[\left\langle \boldsymbol{\psi}, dT(S(\boldsymbol{\alpha}), \boldsymbol{\alpha}; 0, \boldsymbol{\beta})\right\rangle_{\Gamma} + dJ(S(\boldsymbol{\alpha}), \boldsymbol{\alpha}; 0, \boldsymbol{\beta})\right]. \tag{7.24}$$

In the context of our integral equation problem, the directional derivatives in equation (7.24) depend nonlinearly on the explicit parametrization of the dielectric obstacles, which is defined by the parameter vector $\boldsymbol{\alpha}$. Hence, approximations of these derivatives is inexpensively and accurately obtained by means of finite difference approximations by relying on use of certain sparse surface parametrization methods, as discussed in the following section.

7.2.1 Numerical approximation of directional derivatives

The directional derivatives in the $\boldsymbol{\beta}$ direction on the right-hand side of equation (7.24), along which the solution $S(\boldsymbol{\alpha})$ remains unchanged and does not need to be recalculated, can be obtained as indicated in what follows. The definition of these directional derivatives, together with equations (7.4) and (7.8), leads directly to the finite difference approximations

$$dT(S(\boldsymbol{\alpha}), \boldsymbol{\alpha}; 0, \boldsymbol{\beta}) \approx \frac{\mathrm{A}(S(\boldsymbol{\alpha}), \boldsymbol{\alpha} + \delta\boldsymbol{\beta}) - \mathrm{A}(S(\boldsymbol{\alpha}), \boldsymbol{\alpha})}{\delta} - \frac{\mathrm{b}(\boldsymbol{\alpha} + \delta\boldsymbol{\beta}) - \mathrm{b}(\boldsymbol{\alpha})}{\delta}, \tag{7.25}$$

and

$$dJ(S(\boldsymbol{\alpha}), \boldsymbol{\alpha}; 0, \boldsymbol{\beta}) \approx \frac{J(S(\boldsymbol{\alpha}), \boldsymbol{\alpha} + \delta\boldsymbol{\beta}) - J(S(\boldsymbol{\alpha}), \boldsymbol{\alpha})}{\delta}, \tag{7.26}$$

for an adequately chosen value of the parameter δ. Of course, higher-order approximations can be used at the cost of the additional necessary forward map computations.

Remark 7.2.2 *The quantities associated to* b *in equation* (7.25) *can be quickly computed since they only involve the sourcing term of the integral equations. On the other hand,* $\mathrm{A}(S(\boldsymbol{\alpha}), \boldsymbol{\alpha})$ *and* $J(S(\boldsymbol{\alpha}), \boldsymbol{\alpha})$ *are readily known and independent of the direction* $\boldsymbol{\beta}$ *taken. Furthermore, to compute each component of the gradient, we must consider* $\boldsymbol{\beta} = \mathbf{e}_i$ *for* $i = 1, \ldots, M$*, and thus for the evaluation of the gradient, one needs to compute* M *additional froward maps for* $\mathrm{A}(S(\boldsymbol{\alpha}), \boldsymbol{\alpha} + \delta\mathbf{e}_i)$*, and* M *additional objective functions* $J(S(\boldsymbol{\alpha}), \boldsymbol{\alpha} + \delta\boldsymbol{\beta})$*, the latter being considerably cheaper to compute.*

Although in equation (7.25), we have that $\mathrm{A}(S(\boldsymbol{\alpha}), \boldsymbol{\alpha}) - \mathrm{b}(\boldsymbol{\alpha}) = 0$, we note that the explicit form on which the equation is written can be used to exploit the sparsity of the mapping given by

$$\mathrm{A}_\delta(\boldsymbol{\alpha}, \boldsymbol{\beta}) = \mathrm{A}(S(\boldsymbol{\alpha}), \boldsymbol{\alpha} + \delta\boldsymbol{\beta}) - \mathrm{A}(S(\boldsymbol{\alpha}), \boldsymbol{\alpha}). \tag{7.27}$$

To show the sparsity pattern, we first decompose all the boundary integral operators into the contributions from each and every one of the P patches from the geometry parametrization

$$\mathrm{L}(\boldsymbol{m}, \boldsymbol{\alpha}) = \begin{bmatrix} \mathrm{L}_{11} & \ldots & \mathrm{L}_{1P} \\ \vdots & \ddots & \vdots \\ \mathrm{L}_{P1} & \ldots & \mathrm{L}_{PP} \end{bmatrix} \begin{bmatrix} \boldsymbol{m}_1 \\ \vdots \\ \boldsymbol{m}_P \end{bmatrix} \tag{7.28}$$

where L represents any of the relevant integral operators ($L = \mathrm{R}^\Delta_\varepsilon, \mathrm{S}^\Delta_\varepsilon, \mathrm{T}^\Delta_\varepsilon \ldots$) acting on a density $\boldsymbol{m}$, and $\mathrm{L}_{ij}(\boldsymbol{m}_j, \boldsymbol{\alpha})$ denotes the contribution by the density at the j-th patch evaluated at the target i-th patch.

Consider also an auxiliary mapping that takes as argument an index $i = 1, \cdots, M$, and returns a vector of integers $\overrightarrow{q}(i) = [q_1(i), \ldots, q_p(i)]$ that contains the indices of all the parametrization patches that are affected when the i-th parameter $\boldsymbol{\alpha}_i$ is modified. Then, taking the direction $\boldsymbol{\beta} = \mathbf{e}_\ell$, as needed for the gradient computation, we have that the discretization of each one of the operators $\mathrm{A}(S(\boldsymbol{\alpha}), \boldsymbol{\alpha} + \delta\boldsymbol{\beta})$ and $\mathrm{A}(S(\boldsymbol{\alpha}), \boldsymbol{\alpha})$ cannot be sparse. However, because the only components of the linear operators that change are those that correspond to perturbed portions of Γ, then the

following sparsity structure is induced in the underlying integral operators in A:

$$[\mathrm{L}(\boldsymbol{m},\boldsymbol{\alpha}+\delta\mathbf{e}_\ell)-\mathrm{L}(\boldsymbol{m},\boldsymbol{\alpha})]_{ij}=\begin{cases}\mathrm{L}_{ij}(\boldsymbol{m},\boldsymbol{\alpha}+\delta\mathbf{e}_\ell)-\mathrm{L}_{ij}(\boldsymbol{m},\boldsymbol{\alpha}+\delta\mathbf{e}_\ell), & \text{if either } i\in\overrightarrow{q}(\ell) \text{ or } j\in\overrightarrow{q}(\ell)\,,\\ 0, & \text{otherwise.}\end{cases} \tag{7.29}$$

Appropriate use of this sparse structure can enable gradient evaluations that would otherwise prove overwhelmingly expensive.

7.3 Adjoint operators

We now turn our attention to the solution of the adjoint problem in equation (7.23). In principle, one could compute the adjoint operator $\mathrm{A}^\dagger$ by taking the discretized version of A and then construct $\mathrm{A}^\dagger$ by doing the conjugate transpose. This process, however, would require explicitly knowing the entries of these matrices, which can be unfeasible for medium to large sized problems. Instead, to solve the adjoint problem, we follow the same approach as in the case of the direct forward problem. In order to do so, we then have to find a way to compute the action of the adjoint operator.

To derive the action of $\mathrm{A}^\dagger$, we note that A is composed of integral operators that are all in terms of the operators R, T and S defined in equation (5.13). Hence, $\mathrm{A}^\dagger$ can be constructed from the simpler adjoint operators of R, T and S. Indeed, if we take the expressions from equation (5.14) and define their adjoint counter parts

$$\mathrm{S}^{s\dagger}[\varphi](\boldsymbol{r})=\int_\Gamma \overline{G(\boldsymbol{r},\boldsymbol{r}')}\varphi(\boldsymbol{r}')\,\mathrm{d}\sigma(\boldsymbol{r}') \tag{7.30a}$$

$$\overrightarrow{\mathrm{S}}^\dagger[\boldsymbol{d}](\boldsymbol{r})=\int_\Gamma \overline{G(\boldsymbol{r},\boldsymbol{r}')}\boldsymbol{d}(\boldsymbol{r}')\,\mathrm{d}\sigma(\boldsymbol{r}'), \tag{7.30b}$$

$$\overrightarrow{K}^\dagger[\boldsymbol{d}](\boldsymbol{r})=\int_\Gamma \overline{\frac{\partial G}{\partial \boldsymbol{n}(\boldsymbol{r})}}(\boldsymbol{r},\boldsymbol{r}')\boldsymbol{d}(\boldsymbol{r}')\,\mathrm{d}\sigma(\boldsymbol{r}'), \tag{7.30c}$$

for $\boldsymbol{r}\in\Gamma$, then, it can be shown that the adjoints of the electromagnetic operators are given by

$$\mathrm{S}^\dagger[\boldsymbol{d}](\boldsymbol{r})=\overrightarrow{\mathrm{S}}^\dagger\Big[\boldsymbol{n}(\boldsymbol{r}')\times\boldsymbol{d}(\boldsymbol{r}')\Big](\boldsymbol{r}), \tag{7.31a}$$

$$\mathrm{T}^\dagger[\boldsymbol{d}](\boldsymbol{r})=\left(\mathbf{e}^1(\boldsymbol{r})\frac{\partial}{\partial u}+\mathbf{e}^2(\boldsymbol{r})\frac{\partial}{\partial v}\right)\left(\mathrm{S}^{s\dagger}\Big[\mathrm{div}_\Gamma[\boldsymbol{n}(\boldsymbol{r}')\times\boldsymbol{d}(\boldsymbol{r}')]\Big](\boldsymbol{r})\right), \tag{7.31b}$$

$$\mathrm{R}^{\dagger}[\boldsymbol{d}](\boldsymbol{r}) = \left(\mathbf{e}^1(\boldsymbol{r})\frac{\partial}{\partial u} + \mathbf{e}^2(\boldsymbol{r})\frac{\partial}{\partial v}\right) \times \left(\overrightarrow{\mathrm{S}}^{\dagger}\left[\boldsymbol{n}(\boldsymbol{r}') \times \boldsymbol{d}(\boldsymbol{r}')\right](\boldsymbol{r})\right) + \boldsymbol{n}(\boldsymbol{r}) \times \overrightarrow{K}^{\dagger}\left[\boldsymbol{n}(\boldsymbol{r}') \times \boldsymbol{d}(\boldsymbol{r}')\right](\boldsymbol{r}). \tag{7.31c}$$

The action of the adjoint operator of the overall system is then given by

$$\mathrm{A}^{\dagger}(\boldsymbol{\Psi}, \boldsymbol{\alpha}) = \begin{bmatrix} \boldsymbol{\Psi}^{\boldsymbol{m}}(\boldsymbol{r}) + \mathrm{R}_{\varepsilon}^{\dagger\Delta}[\boldsymbol{\Psi}^{\boldsymbol{m}}](\boldsymbol{r}) + \mathrm{S}_{\varepsilon}^{\dagger\Delta}[\boldsymbol{\Psi}^{\boldsymbol{j}}](\boldsymbol{r}) + \mathrm{T}_{\varepsilon}^{\dagger\Delta}[\boldsymbol{\Psi}^{\boldsymbol{j}}](\boldsymbol{r}) \\ \boldsymbol{\Psi}^{\boldsymbol{j}}(\boldsymbol{r}) + \mathrm{R}_{\mu}^{\dagger\Delta}[\boldsymbol{\Psi}^{\boldsymbol{j}}](\boldsymbol{r}) - \mathrm{S}_{\mu}^{\dagger\Delta}[\boldsymbol{\Psi}^{\boldsymbol{m}}](\boldsymbol{r}) - \mathrm{T}_{\mu}^{\dagger\Delta}[\boldsymbol{\Psi}^{\boldsymbol{m}}](\boldsymbol{r}) \end{bmatrix}, \quad \boldsymbol{r} \in \Gamma(\boldsymbol{\alpha}), \tag{7.32}$$

where, analogous to equation (5.32), we have

$$\mathrm{R}_{\alpha}^{\dagger\Delta} \equiv \frac{2}{\alpha_e + \alpha_i}\left(\alpha_e \mathrm{R}_e^{\dagger} - \alpha_i \mathrm{R}_i^{\dagger}\right), \tag{7.33a}$$

$$\mathrm{S}_{\alpha}^{\dagger\Delta} \equiv \frac{2i}{\omega(\alpha_e + \alpha_i)}\left(k_e^2 \mathrm{S}_e^{\dagger} - k_i^2 \mathrm{S}_i^{\dagger}\right), \tag{7.33b}$$

$$\mathrm{T}_{\alpha}^{\dagger\Delta} \equiv \frac{2i}{\omega(\alpha_e + \alpha_i)}\left(\mathrm{T}_e^{\dagger} - \mathrm{T}_i^{\dagger}\right), \tag{7.33c}$$

where the subindex α represents either the dielectric constant symbol, $\alpha = \varepsilon$, or the magnetic permeability $\alpha = \mu$.

Remark 7.3.1 *The solution of the adjoint problem in equation* (7.23) *can be obtained using the rectangular-polar method just as the forward problem (see Chapters 4 and 5). Furthermore, in view of the form of the adjoint operators* (7.31)*, the precomputations needed are exactly the same as those needed for the direct problem in equation* (7.5).

7.4 Numerical examples: Metasurface design

In this section, we apply a standard gradient-descent method in conjunction with the adjoint method described in the previous sections to simulate and optimize optical devices based on multilayer metasurfaces. In brief, a metasurface is a structure that contains dielectric inclusions—of sizes comparable to the wavelength—in arrangements designed to manipulate light in prescribed ways. Metasurface-based

devices have been shown to provide an exceptional control on light at micro scales [4–7, 49, 71].

The particular setting for the problem considered here is that of multilayered metasurfaces used to construct optical metalenses. Each "meta atom" consists of a rounded cylinder of given height, and the radii are the design parameters $\boldsymbol{\alpha}$. In our examples, we illuminate the structure with a plane wave ($x-$polarized), and we take as objective function the square of the $x-$component of the total electric field at a focal point $\boldsymbol{r}_0$, but other types of illumination and objective functions can analogously be considered. All the forward and adjoint solves were performed using an accelerated version of the rectangular polar integration method, relying on the parallel accelerated implementation previously produced, on the basis of serial accelerator method [16], by former group member Dr. Agustin Fernandez-Lado, who also contributed to the overall code implementation used in this section. The particular implementation of the overall solution and optimization method was produced in Fortran with MPI; all runs were done on Caltech's EMSCAT cluster.

Figure 7.1 presents the results of an optimized lens design consisting of ten layers, each layer consisting of a metasurface of ten by ten nanoposts. In this case the electromagnetic parameters are given by $\lambda_0 = 400$ nm, $n_e = 1.0$, $n_i = 1.46$. The height of all the nanoposts is 400 nm, with separation between layers of 700 nm. The posts in each layer are arranged on a Cartesian array, with a separation of 350 nm in both the x- and y-direction; the corresponding optimization problem involves a total of one thousand optimization parameters. For this particular problem, the optimization was capped to 20 gradient-descent iterations. Using 501 cores, each system solve required approximately 260 seconds for each the direct and adjoint problems, and 60 seconds for the evaluation of all necessary sparse forward maps needed to compute the inner products in equation (7.24)—for a total of $\approx$ 10 minutes for one full gradient computation. Use of the simple (non-sparse) version of this algorithm would have required $\approx$ 2.2 hours instead of $\approx$ 10 minutes. Further, use of the direct finite-difference gradient approximation equation (7.12), without any recourse to the adjoint strategy, would have increased the gradient computation time from $\approx$ 10 minutes to $\approx$ 3 days (or two months for the twenty optimization iterations).

The ideas presented in this chapter are easily extensible to multiobjective problems, such as the one presented in Figure 7.2, for which five focal points were used to spell the letter "C." In this case, the metasurface consists of three layers of 14×14

nanoposts with the same parameters as those of Figure 7.1.

Finally, in Figure 7.3, we present the optimized design of an array consisting of ten layers, each of metasurfaces of 5×12 nanoposts. The design consists of nanoposts made of TiO_2 ($n_i = 2.50$) immersed on SiO_2 ($n_e = 1.47$) and the objective function is designed to induce light-focusing at two different points, depending on the illumination wavelength of either 700 nm or 500 nm.

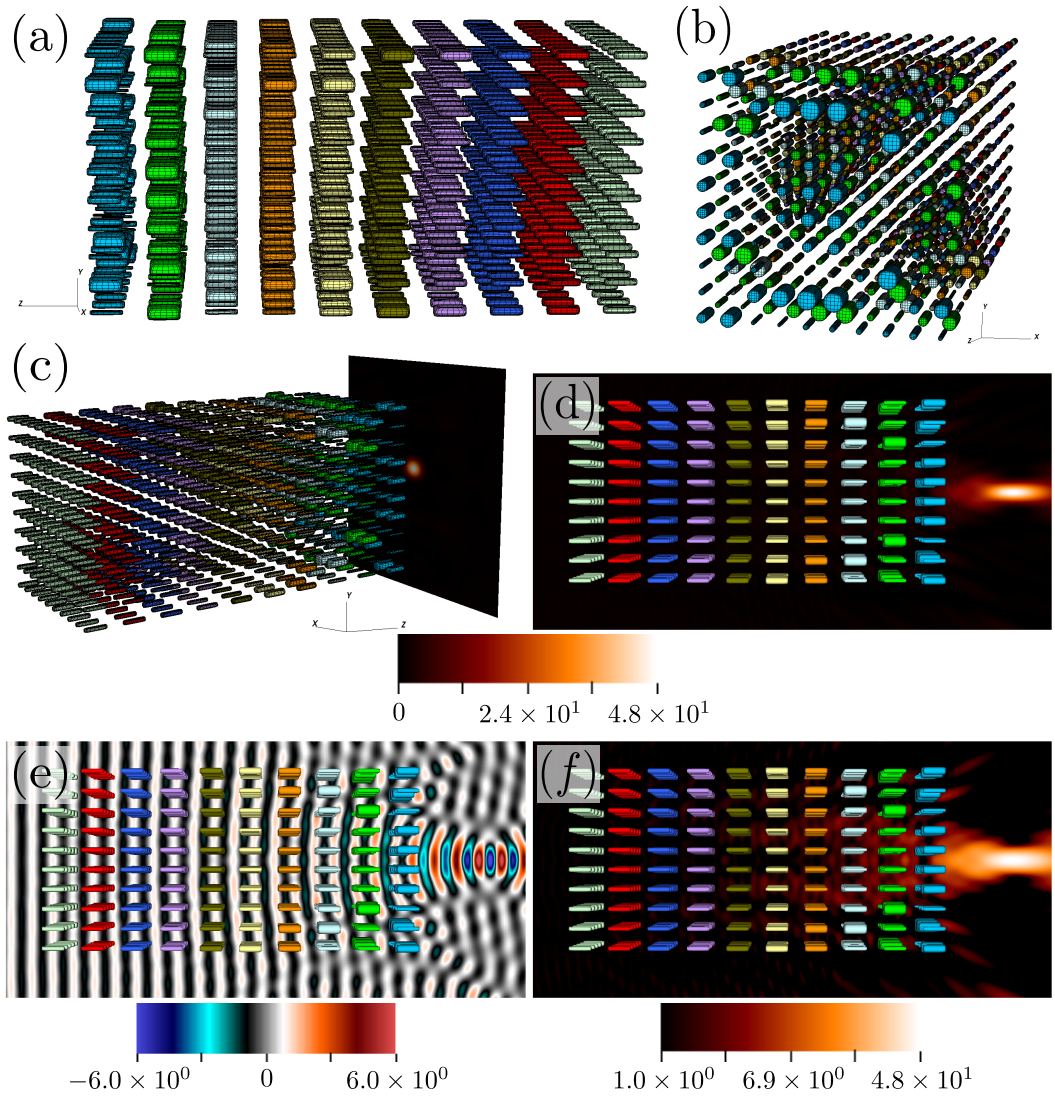

Figure 7.1: Metasurface consisting of an array of $10 \times 10 \times 10$ nanoposts. The design is optimized to focus light at a point in a given focal plane.

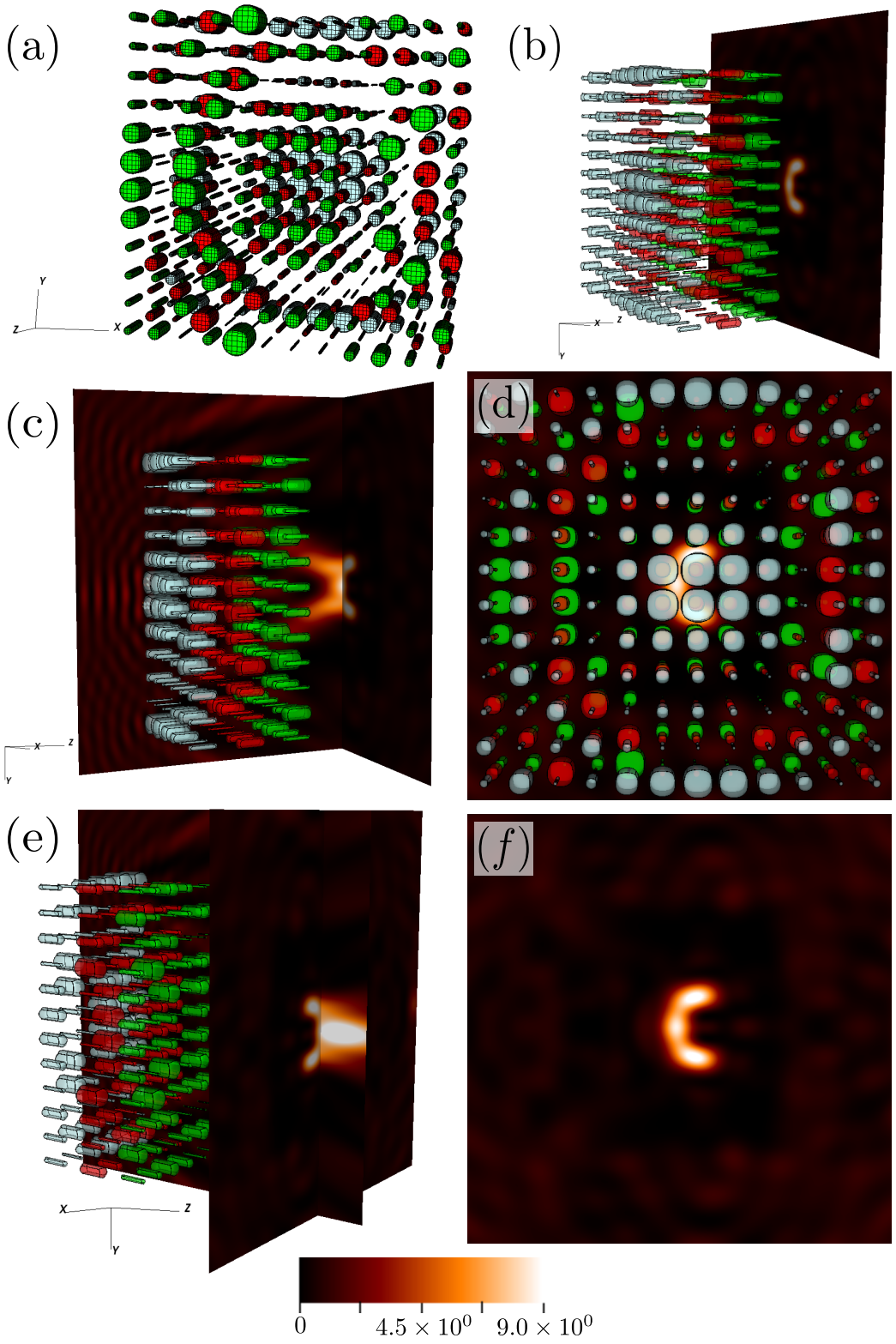

Figure 7.2: Optimized metasurface to focus light on the shape of the letter "C." The size of the array is of $10 \times 10 \times 4$ nanoposts.

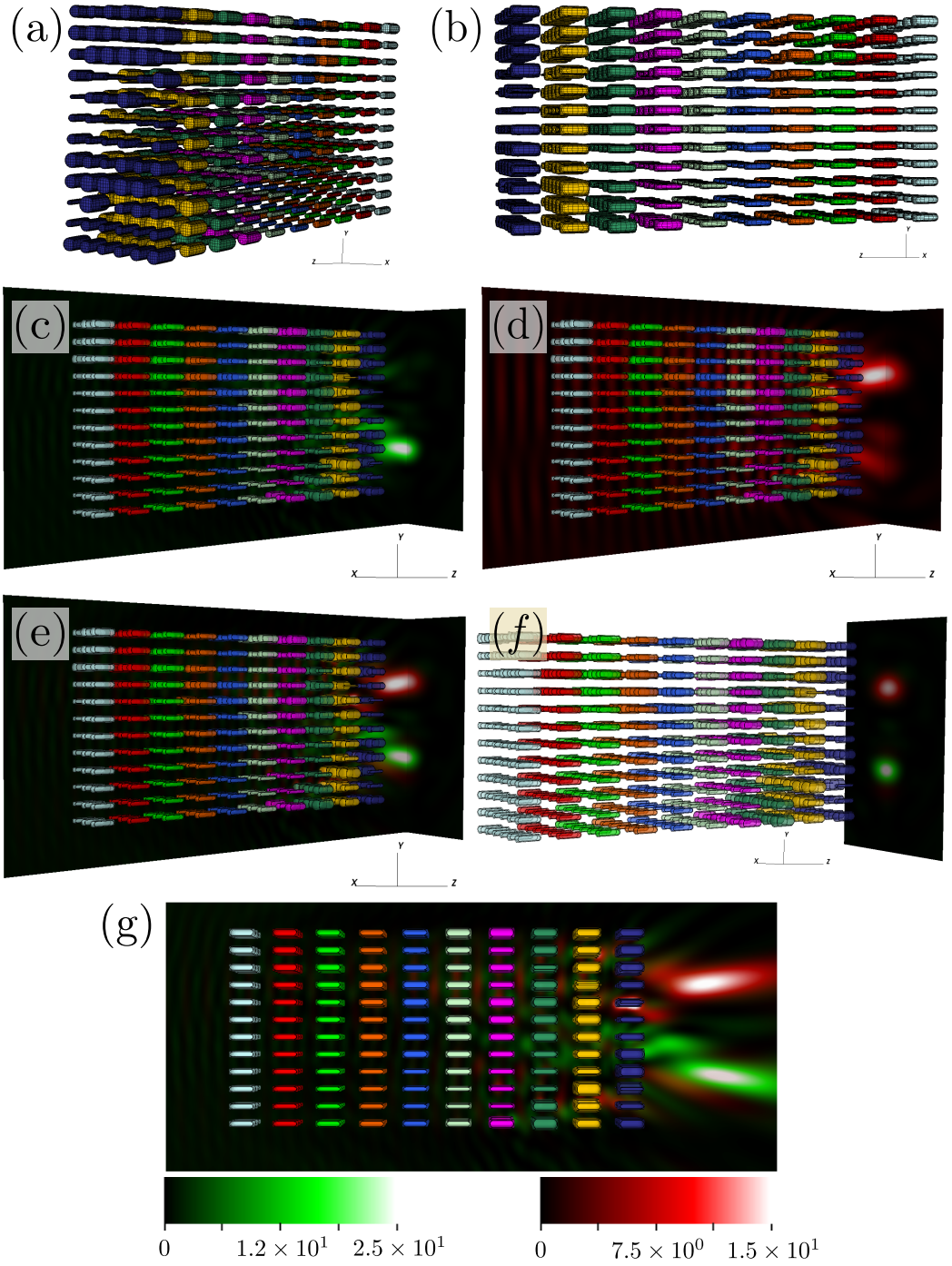

Figure 7.3: Two-wavelength splitter. The size of the array is of $6 \times 12 \times 10$ nanoposts.

Concluding remarks

Chapter 8

CONCLUSIONS AND FUTURE WORK

This thesis presents a variety of integral-equation methods that effectively tackle a range of problems in computational electromagnetism, with application to problems in electrical engineering and applied physics. In particular, the developed techniques were used to solve problems concerning waveguides in two and three dimensions and metamaterial-design problems, demonstrating the value of the integral-equation approach in this context. We conclude this thesis with a brief summary of the proposed methodologies and a discussion of potentially valuable follow-on work.

The WGF method for waveguide problems introduced in Chapters 2 and 6, enables efficient treatment of complex waveguide structures. This approach has already facilitated the design of two-dimensional structures such as waveguide tapers, splitters and grating couplers such as those shown in Figures 8.1 and 8.2 (see [74] for details). This computational method provides super-algebraically accurate approximations as the window sizes are increased and, as a result, the method can be orders of magnitude faster than solvers considered presently in engineering practice [74]. The proposed approach retains the attractive qualities of boundary integral equation methods, such as reduced dimensionality, efficient parallelization, and high-order accuracy for arbitrary geometries. And, while the present implementation is based on use of Nyström integral-equation solvers (which we heartily recommend), any available boundary integral method for transmission problems, such as, e.g., those based on the Method of Moments, can be easily modified to incorporate the WGF methodology.

Many problems in areas of electrical engineering require knowledge of the bound modes of three-dimensional dielectric waveguides, considered in Chapter 3, as these are used as feeds for photonic structures. In practice, a wide variety of waveguide cross sections have been used, and the evaluation of the types of open waveguide modes treated in this chapter have generally been considered challenging. As demonstrated by the numerical examples in Chapter 3, the proposed method provides an accurate and reliable tool for treatment of a problem for which other approaches have experienced difficulties.

The boundary integral equation framework for the optimization of electromag-

netic devices developed in Chapter 7 provides significant advantages. On the basis of its fast and highly-accurate electromagnetic solvers, as well as the new powerful adjoint techniques for gradient evaluation, the methods enable solution of challenging three-dimensional simulation and optimization problems that would otherwise require prohibitively high computing costs.

The rectangular-polar method for singular integrals introduced in Chapter 4 underlies much of the work presented in this thesis. In view of its ability to effectively integrate the types of singular kernels that arise in the context of boundary integral equations in scattering theory, the methodology was used in conjunction with suitable FFT-based acceleration methods and the GMRES linear algebra solver to produce solutions for highly-challenging three-dimensional waveguide problems and three-dimensional metamaterial structures. The rectangular-polar method is itself demonstrated in the context of bounded obstacles, including examples for which the scattering obstacles contain open, closed, smooth and non-smooth, scattering surfaces. In all of these cases the solver produced results with high accuracy in short computing times. In particular, the rectangular-polar method is well-suited for application to general engineering configurations—where the scattering objects are provided in standard (but generally highly complex) CAD representations.

The numerical examples presented throughout this thesis demonstrate the enabling character of the proposed approaches. We believe that the present and subsequent works, as described in the following section, will lead to significant improvements in the computational simulation and optimization capabilities in photonics.

8.1 Future work

A natural continuation of the work presented throughout this thesis concerns use of the three-dimensional WGF method in Chapter 6 in conjunction with the BIE optimization framework developed in Chapter 7 to design and optimize fully three-dimensional waveguide structures. Significant advances have recently been made precisely in this direction in the two-dimensional case [74].

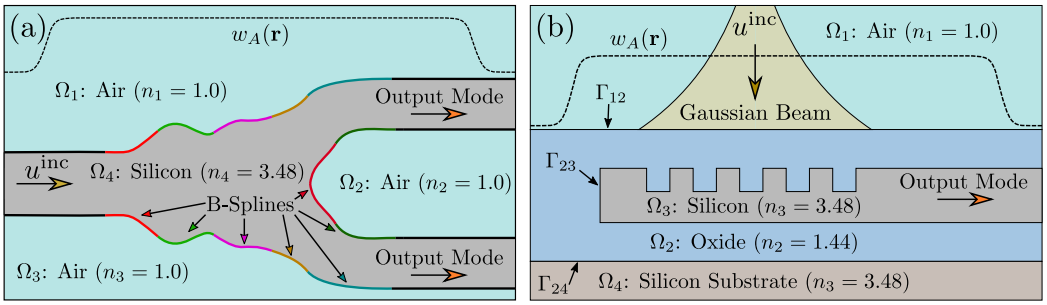

Figure 8.1: Illustrations of the two-dimensional mode splitter (a) and grating coupler (b) problems [74].

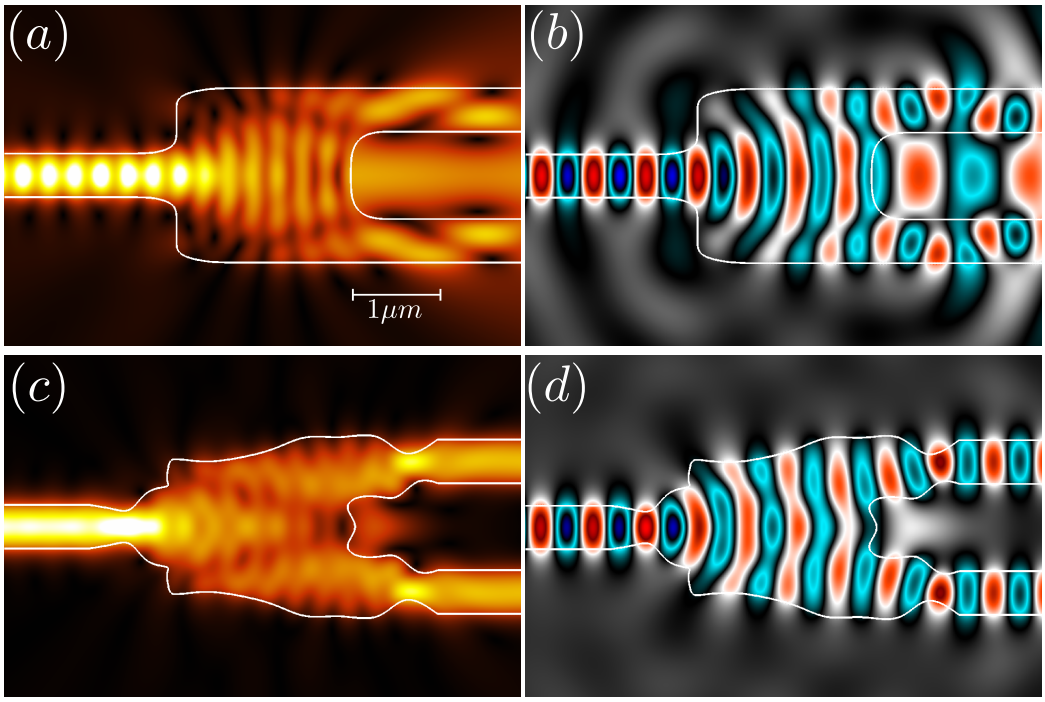

Figure 8.2: In (a) and (b), we show the intensity and real part of the fields, respectively, for the initial, non-optimized splitter. On the other hand, (c) and (d) present the optimized counterparts [74].

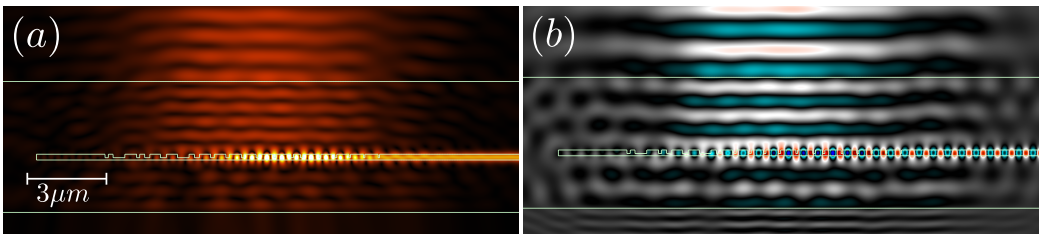

Figure 8.3: Intensity (a) and real part (b) of the fields produced by the WGF adjoint optimization algorithm for the problem of the grating coupler [74].

For reference in this context we present Figures 8.1 to 8.3 from [74], which demonstrate the character of the applied problems that can be treated by these methods. In particular, Figure 8.1 (a) depicts the problem of mode splitting, on which the boundaries of a waveguide junction are optimized to split the energy onto two separate waveguides. In Figure 8.1 (b), the problem of the grating coupler is depicted. In this case, a serrated structure is illuminated by a beam, and the sizes of the grating "teeth" are designed to couple as much energy as possible to the output mode. Figures 8.2 and 8.3 present the results of the optimization runs obtained for the mode splitter and the grating coupler, respectively. Forthcoming work along the lines of this effort seeks to extend and apply these methodologies to some of the most challenging and exciting three-dimensional design problems in electromagnetics in general, and photonics in particular.

Back matter

BIBLIOGRAPHY

[1] Milton Abramowitz and Irene A. Stegun. *Handbook of Mathematical Functions with Formulas, Graphs, and Mathematical Tables*. National Bureau of Standards. Washington, D.C., 10th edition, 1972.

[2] Eldar Akhmetgaliyev. *Fast numerical methods for mixed, singular Helmholtz boundary value problems and Laplace eigenvalue problems—with applications to antenna design, sloshing, electromagnetic scattering and spectral geometry*. PhD thesis, California Institute of Technology, 2016. doi: 10.7907/Z97P8W93.

[3] Eldar Akhmetgaliyev, Oscar P. Bruno, and Nilima Nigam. A boundary integral algorithm for the Laplace Dirichlet-Neumann mixed eigenvalue problem. *Journal of Computational Physics*, 298:1–28, October 2015. ISSN 00219991. doi: 10.1016/j.jcp.2015.05.016. arXiv ID: 1411.0071.

[4] Amir Arbabi and Andrei Faraon. Fundamental limits of ultrathin metasurfaces. *Scientific Reports*, 7:43722, March 2017. ISSN 2045-2322. doi: 10.1038/srep43722. arXiv ID: 1411.2537.

[5] Amir Arbabi, Yu Horie, Mahmood Bagheri, and Andrei Faraon. Dielectric metasurfaces for complete control of phase and polarization with subwavelength spatial resolution and high transmission. *Nature Nanotechnology*, 10 (11):937–943, August 2015. ISSN 1748-3387. doi: 10.1038/nnano.2015.186.

[6] Amir Arbabi, Yu Horie, Alexander J. Ball, Mahmood Bagheri, and Andrei Faraon. Subwavelength-thick lenses with high numerical apertures and large efficiency based on high-contrast transmitarrays. *Nature Communications*, 6: 7069, May 2015. ISSN 20411723. doi: 10.1038/ncomms8069. arXiv ID: 1410.8261.

[7] Ehsan Arbabi, Amir Arbabi, Seyedeh Mahsa Kamali, Yu Horie, and Andrei Faraon. Multiwavelength polarization-insensitive lenses based on dielectric metasurfaces with meta-molecules. *Optica*, 3(6):628, June 2016. ISSN 2334-2536. doi: 10.1364/OPTICA.3.000628.

[8] George B. Arfken, Hans J. Weber, and Frank E. Harris. *Mathematical Methods for Physicists: A Comprehensive Guide*. Elsevier. Waltham, MA, 7th edition, 2013. ISBN 9780123846549. doi: 10.1016/C2009-0-30629-7.

[9] Jean-Pierre Berenger. A perfectly matched layer for the absorption of electromagnetic waves. *Journal of Computational Physics*, 114(2):185–200, October 1994. ISSN 00219991. doi: 10.1006/jcph.1994.1159.

[10] Timo Betcke and Lloyd N. Trefethen. Reviving the method of particular solutions. *SIAM review*, 47(3):469–491, January 2005. ISSN 0036-1445. doi: 10.1137/S0036144503437336.

[11] John P. Boyd. *Chebyshev and Fourier Spectral Methods*. Dover Publications, Inc. Mineola, New York, 2nd edition, 2001. ISBN 978-0486411835.

[12] James Bremer and Zydrunas Gimbutas. A Nyström method for weakly singular integral operators on surfaces. *Journal of Computational Physics*, 231(14): 4885–4903, May 2012. ISSN 00219991. doi: 10.1016/j.jcp.2012.04.003.

[13] Oscar P. Bruno and Bérangère Delourme. Rapidly convergent two-dimensional quasi-periodic Green function throughout the spectrum-including Wood anomalies. *Journal of Computational Physics*, 262:262–290, April 2014. ISSN 00219991. doi: 10.1016/j.jcp.2013.12.047.

[14] Oscar P. Bruno and Agustin G. Fernandez-Lado. Rapidly convergent quasi-periodic Green functions for scattering by arrays of cylinders—including Wood anomalies. *Proceedings of the Royal Society A: Mathematical, Physical and Engineering Science*, 473(2199):20160802, March 2017. ISSN 1364-5021. doi: 10.1098/rspa.2016.0802.

[15] Oscar P. Bruno and Leonid A. Kunyansky. A Fast, High-Order Algorithm for the Solution of Surface Scattering Problems: Basic Implementation, Tests, and Applications. *Journal of Computational Physics*, 169(1):80–110, May 2001. ISSN 00219991. doi: 10.1006/jcph.2001.6714.

[16] Oscar P. Bruno and Leonid A. Kunyansky. Surface scattering in three dimensions: an accelerated high-order solver. *Proceedings of the Royal Society A: Mathematical, Physical and Engineering Sciences*, 457(2016):2921–2934, December 2001. ISSN 1364-5021. doi: 10.1098/rspa.2001.0882.

[17] Oscar P. Bruno and Stéphane K. Lintner. A high-order integral solver for scalar problems of diffraction by screens and apertures in three-dimensional space. *Journal of Computational Physics*, 252:250–274, November 2013. ISSN 00219991. doi: 10.1016/j.jcp.2013.06.022. arXiv ID: 1208.5173.

[18] Oscar P. Bruno and Carlos Pérez-Arancibia. Windowed Green function method for the Helmholtz equation in the presence of multiply layered media. *Proceedings of the Royal Society A: Mathematical, Physical and Engineering Sciences*, 473(2202):20170161, June 2017. doi: 10.1098/rspa.2017.0161.

[19] Oscar P. Bruno, Jeffrey S. Ovall, and Catalin Turc. A high-order integral algorithm for highly singular PDE solutions in Lipschitz domains. *Computing*, 84(3-4):149–181, April 2009. ISSN 0010-485X. doi: 10.1007/s00607-009-0031-1.

[20] Oscar P. Bruno, Mark Lyon, Carlos Pérez-Arancibia, and Catalin Turc. Windowed Green Function Method for Layered-Media Scattering. *SIAM Journal on Applied Mathematics*, 76(5):1871–1898, January 2016. ISSN 0036-1399. doi: 10.1137/15M1033782.

[21] Oscar P. Bruno, Stephen P. Shipman, Catalin Turc, and Stephanos Venakides. Superalgebraically convergent smoothly windowed lattice sums for doubly periodic Green functions in three-dimensional space. *Proceedings of the Royal Society A: Mathematical, Physical and Engineering Sciences*, 472(2191): 20160255, July 2016. ISSN 1364-5021. doi: 10.1098/rspa.2016.0255. arXiv ID: 1307.1176.

[22] Oscar P. Bruno, Emmanuel Garza, and Carlos Pérez-Arancibia. Windowed Green function method for nonuniform open-waveguide problems. *IEEE Transactions on Antennas and Propagation*, 65(9):4684–4692, September 2017. ISSN 0018926X. doi: 10.1109/TAP.2017.2728118. arXiv ID: 1610.04939.

[23] Oscar P. Bruno, Stephen P. Shipman, Catalin Turc, and Venakides Stephanos. Three-dimensional quasi-periodic shifted Green function throughout the spectrum, including Wood anomalies. *Proceedings of the Royal Society A: Mathematical, Physical and Engineering Sciences*, 473(2207):20170242, November 2017. ISSN 1364-5021. doi: 10.1098/rspa.2017.0242. arXiv ID: 1704.01017.

[24] Julian Chaubell, Oscar P. Bruno, and Chi O. Ao. Evaluation of EM-wave propagation in fully three-dimensional atmospheric refractive index distributions. *Radio Science*, 44(1):RS1012, February 2009. ISSN 00486604. doi: 10.1029/2008RS003882.

[25] Carl G. Chen, Paul T. Konkola, Juan Ferrera, Ralf K. Heilmann, and Mark L. Schattenburg. Analyses of vector Gaussian beam propagation and the validity of paraxial and spherical approximations. *Journal of the Optical Society of America A*, 19(2):404, February 2002. ISSN 1084-7529. doi: 10.1364/JOSAA.19.000404.

[26] Hank Childs, Eric Brugger, Brad Whitlock, Jeremy Meredith, Sean Ahern, David Pugmire, Kathleen Biagas, Mark Miller, Cyrus Harrison, Gunther H. Weber, Hari Krishnan, Thomas Fogal, Allen Sanderson, Christoph Garth, E Wes Bethel, David Camp, Oliver Rübel, Marc Durant, Jean M. Favre, and Paul Navrátil. VisIt: An End-User Tool For Visualizing and Analyzing Very Large Data. In *High Performance Visualization–Enabling Extreme-Scale Scientific Insight*, chapter 16, pages 357–372. CRC Press, October 2012.

[27] Giulio Ciraolo. *Non-Rectilinear Waveguides: Analytical and Numerical Results Based on the Green's Function*. PhD thesis, Universita Degli Studi Di Firenze, 2005.

[28] Giulio Ciraolo and Rolando Magnanini. Analytical results for 2-D non-rectilinear waveguides based on a Green's function. *Mathematical Methods in the Applied Sciences*, 31(13):1587–1606, September 2008. ISSN 01704214. doi: 10.1002/mma.988. arXiv ID: arXiv:0704.3847v1.

[29] James Clerk Maxwell. On Faraday's lines of force: Part I. *Proceedings of the Cambridge Philosophical Society. Mathematical and physical sciences*, 1 part xi:160–162, December 1855. ISSN 0008-1981.

[30] James Clerk Maxwell. On Faraday's lines of force: Part II. *Proceedings of the Cambridge Philosophical Society. Mathematical and physical sciences*, 1 part xi:163–166, February 1856. ISSN 0008-1981.

[31] David Colton and Rainer Kress. *Integral Equation Methods in Scattering Theory*. John Wiley & Sons, Inc. New York, 1st edition, 1983. ISBN 978-1-611973-15-0.

[32] David Colton and Rainer Kress. *Inverse Acoustic and Electromagnetic Scattering Theory*. Springer. New York, 3rd edition, 2013. ISBN 978-1-4614-4942-3. doi: 10.1007/978-1-4614-4942-3.

[33] Martin Costabel and Monique Dauge. General edge asymptotics of solutions of second-order elliptic boundary value problems I. *Proceedings of the Royal Society of Edinburgh: Section A Mathematics*, 123(1):109–155, November 1993. ISSN 0308-2105. doi: 10.1017/S0308210500021272.

[34] Juan Carlos De los Reyes. *Numerical PDE-Constrained Optimization*. Springer. New York, 1st edition, 2015. ISBN 978-3-319-13394-2. doi: 10.1007/978-3-319-13395-9.

[35] Laurent Demanet and Lexing Ying. Scattering in Flatland: Efficient Representations via Wave Atoms. *Foundations of Computational Mathematics*, 10(5): 569–613, October 2010. ISSN 1615-3375. doi: 10.1007/s10208-010-9070-4. arXiv ID: 0805.4022.

[36] Yongbo Deng and Jan G. Korvink. Topology optimization for three-dimensional electromagnetic waves using an edge element-based finite-element method. *Proceedings of the Royal Society A: Mathematical, Physical and Engineering Science*, 472(2189):20150835, May 2016. ISSN 1364-5021. doi: 10.1098/rspa.2015.0835.

[37] John A. DeSanto and Paul A. Martin. On the derivation of boundary integral equations for scattering by an infinite one-dimensional rough surface. *The Journal of the Acoustical Society of America*, 102(1):67, July 1997. ISSN 00014966. doi: 10.1121/1.419714.

[38] Ardavan Farjadpour, David Roundy, Alejandro Rodriguez, Mihai Ibanescu, Peter Bermel, John D. Joannopoulos, Steven G. Johnson, and Geoffrey W.

Burr. Improving accuracy by subpixel smoothing in the finite-difference time domain. *Optics Letters*, 31(20):2972, October 2006. ISSN 0146-9592. doi: 10.1364/OL.31.002972.

[39] Thomas Frevillier. Suborbital spaceflights, 2015. URL `https://grabcad.com/library/suborbital-spaceflights-1`.

[40] Mahadevan Ganesh and Ivan G. Graham. A high-order algorithm for obstacle scattering in three dimensions. *Journal of Computational Physics*, 198(1): 211–242, July 2004. ISSN 00219991. doi: 10.1016/j.jcp.2004.01.007.

[41] Michael B. Giles and Niles A. Pierce. An Introduction to the Adjoint Approach to Design. *Flow, Turbulence and Combustion*, 65(3-4):393–415, December 2000. ISSN 1573-1987. doi: 10.1023/A:1011430410075.

[42] David J. Griffiths. *Introduction to Electrodynamics*. Prentice Hall. Upper Saddle River, New Jersey, 3rd edition, 1999. ISBN 0-13-805326-X.

[43] Nail A. Gumerov and Ramani Duraiswami. *Fast Multipole Methods for the Helmholtz Equation in Three Dimensions*. Elsevier Ltd. Kidlington, Oxford, 1st edition, 2004. ISBN 0-08-044371-0.

[44] Paul Hansen and Lambertus Hesselink. Accurate adjoint design sensitivities for nano metal optics. *Optics Express*, 23(18):23899, September 2015. ISSN 1094-4087. doi: 10.1364/OE.23.023899. arXiv ID: arXiv:1308.0212.

[45] Demetrios Hondros and Peter Debye. Elektromagnetische Wellen an dielektrischen Drähten. *Annalen der Physik*, 337(8):465–476, 1910. ISSN 00033804. doi: 10.1002/andp.19103370802.

[46] John David Jackson. *Classical Electrodynamics*. John Wiley & Sons, Inc. Hoboken, New Jersey, 3rd edition, 1998. ISBN 0-471-30932-X.

[47] Barbara M. Johnston, Peter R. Johnston, and David Elliott. A sinh transformation for evaluating two-dimensional nearly singular boundary element integrals. *International Journal for Numerical Methods in Engineering*, 69(7): 1460–1479, February 2007. ISSN 00295981. doi: 10.1002/nme.1816.

[48] Peter R. Johnston and David Elliott. A sinh transformation for evaluating nearly singular boundary element integrals. *International Journal for Numerical Methods in Engineering*, 62(4):564–578, January 2005. ISSN 0029-5981. doi: 10.1002/nme.1208.

[49] Seyedeh Mahsa Kamali, Ehsan Arbabi, Amir Arbabi, and Andrei Faraon. A review of dielectric optical metasurfaces for wavefront control. *Nanophotonics*, 7(6):1041–1068, May 2018. ISSN 21928614. doi: 10.1515/nanoph-2017-0129. arXiv ID: 1804.09802.

[50] Andreas Klöckner, Alexander H. Barnett, Leslie Greengard, and Michael O'Neil. Quadrature by Expansion: A New Method for the Evaluation of Layer Potentials. *Journal of Computational Physics*, 252(3):332–349, November 2013. ISSN 00219991. doi: 10.1016/j.jcp.2013.06.027. arXiv ID: arXiv:1207.4461v2.

[51] Dana A. Knoll and David E. Keyes. Jacobian-free Newton–Krylov methods: a survey of approaches and applications. *Journal of Computational Physics*, 193 (2):357–397, January 2004. ISSN 00219991. doi: 10.1016/j.jcp.2003.08.010.

[52] Rainer Kussmaul. Ein numerisches Verfahren zur Lösung des Neumannschen Außenraumproblems für die Helmholtzsche Schwingungsgleichung. *Computing*, 4(3):246–273, September 1969. ISSN 0010-485X. doi: 10.1007/BF02234773.

[53] Christopher M. Lalau-Keraly, Samarth Bhargava, Owen D. Miller, and Eli Yablonovitch. Adjoint shape optimization applied to electromagnetic design. *Optics Express*, 21(18):21693, September 2013. ISSN 1094-4087. doi: 10.1364/OE.21.021693.

[54] Nikolai Nikolaevich Lebedev and Richard A. Silverman. *Special functions and their applications*. Dover Publications, Inc. New York, 1st edition, 1972.

[55] Martin Maas. *High order fast numerical methods for scattering problems by preiodic surfaces and groups of particles - including Wood anomalies*. PhD thesis, Universidad de Buenos Aires, 2018.

[56] Rolando Magnanini and Fadil Santosa. Wave Propagation in a 2-D Optical Waveguide. *SIAM Journal on Applied Mathematics*, 61(4):1237–1252, 2001. doi: 10.1137/S0036139999360489.

[57] Johannes Markkanen, Pasi Ylä-Oijala, and Ari Sihvola. Surface integral equation method for scattering by DB objects with sharp wedges. *Applied Computational Electromagnetics Society Journal*, 26(5):367–374, May 2011.

[58] Erich Martensen. Über eine Methode zum räumlichen Neumannschen Problem mit einer Anwendung für torusartige Berandungen. *Acta Mathematica*, 109 (1):75–135, 1963. ISSN 0001-5962. doi: 10.1007/BF02391810.

[59] James Clerk Maxwell. A dynamical theory of the electromagnetic field. *Philosophical Transactions of the Royal Society of London*, 155(2986):459–512, January 1865. ISSN 0261-0523. doi: 10.1098/rstl.1865.0008.

[60] James Clerk Maxwell. *A Treatise on Electricity and Magnetism*. Cambridge University Press. Cambridge, 1st edition, 1873. ISBN 9780511709333. doi: 10.1017/CBO9780511709333.

[61] John A. Monro. *A Super-Algebraically Convergent, Windowing-Based Approach to the Evaluation of Scattering from Periodic Rough Surfaces*. PhD thesis, California Institute of Technology, 2007.

[62] Claus Muller. *Foundations of the Mathematical Theory of Electromagnetic Waves*. Springer-Verlag. New York, 1st edition, 1969.

[63] Jean Claude Nédélec. *Acoustic and Electromagnetic Equations: Integral Representations for Harmonic Problems*. Springer. 1st edition, 2001. ISBN 978-1-4419-2889-4. doi: 10.1007/978-1-4757-4393-7.

[64] Armand C. R. Niederberger, David A. Fattal, Nicolas R. Gauger, Shanhui Fan, and Raymond G. Beausoleil. Sensitivity analysis and optimization of sub-wavelength optical gratings using adjoints. *Optics Express*, 22(11):12971, June 2014. ISSN 1094-4087. doi: 10.1364/OE.22.012971.

[65] Natalia K. Nikolova, John W. Bandler, and Mohamed H. Bakr. Adjoint Techniques for Sensitivity Analysis in High-Frequency Structure CAD. *IEEE Transactions on Microwave Theory and Techniques*, 52(1):403–419, January 2004. ISSN 0018-9480. doi: 10.1109/TMTT.2003.820905.

[66] Natalia K. Nikolova, Reza Safian, Ezzeldin A. Soliman, Mohamed H. Bakr, and John W. Bandler. Accelerated Gradient Based Optimization Using Adjoint Sensitivities. *IEEE Transactions on Antennas and Propagation*, 52(8):2147–2157, August 2004. ISSN 0018-926X. doi: 10.1109/TAP.2004.832313.

[67] Alexander I. Nosich. Radiation conditions, limiting absorption principle, and general relations in open waveguide scattering. *Journal of electromagnetic waves and applications*, 8(3):329–353, January 1994.

[68] Carlos Pérez-Arancibia. *Windowed integral equation methods for problems of scattering by defects and obstacles in layered media*. PhD thesis, California Institute of Technology, 2016. doi: 10.7907/Z9GQ6VQT.

[69] Carlos Pérez-Arancibia, Luiz M. Faria, and Catalin Turc. Harmonic density interpolation methods for high-order evaluation of Laplace layer potentials in 2D and 3D. *Journal of Computational Physics*, 376:411–434, January 2019. ISSN 10902716. doi: 10.1016/j.jcp.2018.10.002.

[70] Carlos Pérez-Arancibia, Catalin Turc, and Luiz Faria. Planewave Density Interpolation Methods for 3D Helmholtz Boundary Integral Equations. *SIAM Journal on Scientific Computing*, 41(4):A2088–A2116, January 2019. ISSN 1064-8275. doi: 10.1137/19M1239866.

[71] Raphaël Pestourie, Carlos Pérez-Arancibia, Zin Lin, Wonseok Shin, Federico Capasso, and Steven G. Johnson. Inverse design of large-area metasurfaces. *Optics Express*, 26(26):33732, December 2018. ISSN 1094-4087. doi: 10.1364/OE.26.033732. arXiv ID: 1808.04215.

[72] William H. Press, Saul A. Teukolsky, William T. Vetterling, and Brian P. Flannery. *Numerical recipes: The art of scientific computing*. Cambridge University Press. New York, 3rd edition, 2007. ISBN 978-0-511-33555-6.

[73] Sadasiva M. Rao, Donald R. Wilton, and Allen W. Glisson. Electromagnetic scattering by surfaces of arbitrary shape. *IEEE Transactions on Antennas and Propagation*, 30(3):409–418, May 1982. ISSN 0096-1973. doi: 10.1109/TAP.1982.1142818.

[74] Constantine Sideris, Emmanuel Garza, and Oscar P. Bruno. Ultra-Fast Simulation and Optimization of Nanophotonic Devices with Integral Equation Methods. *ACS Photonics*, November 2019. ISSN 2330-4022. doi: 10.1021/acsphotonics.9b01137.

[75] Allan W. Snyder and John D. Love. *Optical Waveguide Theory*. Chapman and Hall. New York, 1st edition, 1983.

[76] Allen Taflove and Susan C. Hagness. *Computational Electrodynamics - The Finite-Difference Time-Domain Method*. Artech House, Inc. Norwood, 3rd edition, 2005. ISBN 1-58053-832-0.

[77] Fredi Tröltzsch. *Optimal Control of Partial Differential Equations: Theory, Methods and Applications*. American Mathematical Society. Providence, Rhode Island, 1st edition, 2010. ISBN 978-0-8218-4904-0.

[78] Catalin Turc, Akash Anand, Oscar P. Bruno, and Julian Chaubell. Efficient Solution of Three-Dimensional Problems of Acoustic and Electromagnetic Scattering by Open Surfaces. In *10th International Conference on Mathematical and Numerical Aspects of Waves*, July 2011. URL `http://hdl.handle.net/2014/43461`.

[79] Jörg Waldvogel. Fast Construction of the Fejér and Clenshaw–Curtis Quadrature Rules. *BIT Numerical Mathematics*, 46(1):195–202, March 2006. ISSN 0006-3835. doi: 10.1007/s10543-006-0045-4.

[80] Pasi Ylä-Oijala and Matti Taskinen. Well-conditioned Muller formulation for electromagnetic scattering by dielectric objects. *IEEE Transactions on Antennas and Propagation*, 53(10):3316–3323, October 2005. ISSN 0018-926X. doi: 10.1109/TAP.2005.856313.

[81] Lei Zhang, Jung Hoon Lee, Ardavan Oskooi, Amit Hochman, Jacob K. White, and Steven G. Johnson. A Novel Boundary Element Method Using Surface Conductive Absorbers for Full-Wave Analysis of 3-D Nanophotonics. *Journal of Lightwave Technology*, 29(7):949–959, April 2011. ISSN 0733-8724. doi: 10.1109/JLT.2011.2107727. arXiv ID: 1004.5076.

[82] Maksym V. Zhelyeznyakov, Alan Zhan, and Arka Majumdar. Design and Optimization of Ellipsoid Scatterer-based Metasurfaces via the Inverse T-Matrix Method. *arXiv*, pages 1–19, August 2019. arXiv ID: 1908.10466.